Title

Studies in electronic structure theory: Non-orthogonal configuration interaction, oxidation state analysis, and proton reduction catalysis.

Author

Sundstrom, Eric Jon

Publication Date

2014

Peer reviewed|Thesis/dissertation

Studies in electronic structure theory: Non-orthogonal configuration interaction, oxidation state analysis, and proton reduction catalysis.

by

Eric Jon Sundstrom

A dissertation submitted in partial satisfaction of the
requirements for the degree of
Doctor of Philosophy

in

Chemistry

in the

Graduate Division

of the

University of California, Berkeley

Committee in charge:

Professor Martin Head-Gordon, Chair
Professor William H. Miller
Professor Jeffrey A. Reimer

Spring 2014

Studies in electronic structure theory: Non-orthogonal configuration interaction, oxidation state analysis, and proton reduction catalysis.

Abstract

Studies in electronic structure theory: Non-orthogonal configuration interaction, oxidation state analysis, and proton reduction catalysis.

by

Eric Jon Sundstrom

Doctor of Philosophy in Chemistry

University of California, Berkeley

Professor Martin Head-Gordon, Chair

In this dissertation, we will investigate two different areas of electronic structure theory. In the first portion, we shall focus on the study of molecular transition metal systems. Specifically, we will be modeling oxidation and reduction catalysts, which are potentially useful in creating new clean energy sources. Secondly, we will develop a wave-function based method for computing electronic excited states, with a focus on multielectron excitations. These excitations play an important role in many areas of physics and chemistry, including photosynthesis, vision, and organic solar cells.

Quantum mechanics tells one how to compute all the properties of a system which correspond to operators, but what if a property of a given system has no corresponding operator and what if this property provides synthetic chemists a collectively obtained historical intuition about reactivity? This set of questions exactly applies to the case of oxidation state, a property which represents the hypothetical charge on a given atom. This makes calculating oxidation states from electronic structure a matter of creating a recipe which respects both the physics of the system and matches "known" values. We develop one such recipe which we call the localized orbital bonding analysis (LOBA). This method is based on two standard electronic structure methods: localization of molecular orbitals and population analysis. We show that LOBA matches "known" oxidation states of a large set of transition metal systems, we compare it with other recipes for calculating oxidation states, and use it to show a ligand reduction in a proposed transition-metal water-oxidation catalyst.

Now that we have a method which allows us to present computational results in a chemically intuitive framework, we applied LOBA and Kohn-Sham Density Functional Theory (KS-DFT) to study the electro-catalytic generation of hydrogen from protons in an aqueous solution by a molecular molybdenum-oxo complex. We mapped out the thermodynamics of the catalytic cycle including both the reduction steps, which by comparison with experimental evidence were found to be coupled with a proton transfer. We also evaluated the kinetics of the release of hydrogen gas, using transition state theory. It was found experimentally that the reduction overpotential would be the limiting factor in using this catalyst for real

world applications By analyzing the LOBA results across this cycle, we found that one of the reductions partially occurred on the ligand, because of this we supposed that substitutions on the ligand could provide changes in the reduction potentials. With this evidence we calculated the same path for the complex with electron withdrawing (fluorides) and electron donating (methyl-) groups located on the ligand and found that the fluorides reduced the potential making the catalyst theoretically more efficient. Additionally, we present an alternative mechanism for H_2 release which has a lower energy barrier by the inclusion of a bridging water, propose a mechanism for the stoichiometric reaction which produces the catalyst, and discuss alternative catalytic cycles.

Our second major advance was the development of an excited state method, Non-orthogonal Configuration Interaction (NOCI). This method has many advantages including the ability to treat double excitations at the same level as single excitations and low computational scaling when compared with other methods. NOCI is a configuration interaction method where the basis in which one diagonalizes the Hamiltonian can be any Slater determinant, each of which may be non-orthogonal with the rest of the basis. To provide proof of concept, we choose systems for which the character of the wavefunctions of excited states are known; the linear polyenes and β-carotene. This also showed that NOCI is able to treat double excitations which are important for these systems. We demonstrate that NOCI, when applied to systems with extended conjugation, provides a feasible way to obtain a qualitatively correct wavefunction. We also present a new extension to this method allowing for purification of higher-order spin states by utilizing Generalized Hartree–Fock (GHF) Slater determinants and the details for computing $\langle S^2 \rangle$ for the ground and excited states. In order to apply NOCI more straightforwardly to other systems, we develop a procedure for automatically generating the Slater determinants used in the expansion of the wavefunction. This method utilizes information from the Hartree–Fock Hessian to generate the basis for diagonalizing the Hamiltonian. We validate this method by considering a subset of the systems studied in the previous section, showing that the method performs almost the same as when prior knowledge of the system is used to choose the basis. We also corroborate this success by applying the method to a wide range of well-characterized chromophores, resulting in errors very similar to CIS for single excitations and much improved for double excitations.

To Rita and Leon,

For all the things.

Contents

List of Figures

List of Tables

Acknowledgments

My Ph.D. would not have been possible without the help and support by many people both prior to and during my time at Berkeley. First and most directly, I would like to thank my advisor, Martin Head-Gordon, for always providing me with valuable insights and discussions. You gave me the time and space to explore my own ideas and truly grow as a scientist. For that and the ride home from Orinda, I will always be grateful. Secondly, I would like to thank Alex Thom for recognizing both what I was prepared to do when I arrived at Berkeley and also what I would be capable of later. You put my feet on the path I walked; it was a bit rough but turned out quite nice. I have to thank Leslie Silvers for her friendship, advice, and for always making sure I was paid. Before I even turned up to Berkeley my scientific style and career was already influenced by Professors Anna Krylov and Dor Ben-Amotz, without whom I do not think I would have even applied to Berkeley.

I also would not be here without the assistance of these lovely people:

My officemates: KVL, WK, DES, YM

My labmates: PRH, RJA, DSL, NM, SFM, NJM, FAMB, EE, EWN, DWS, KB, EL, ASK, TAB, AWH, KDC, JT, AFW, JKW

My classmates: PAS, ZRM, JMS, GO'D, DPH, SJE, DTL, ABG, JRH, CSM, DJL, ANJS

My family: ABS, IWS, DJE, KLE-D, JCS, JLS, JMS

My friends: REM, KLG, GLG, RML, SML, BAW, NAW, DMA, EHHA, MAR, LDR

I would also like to thank the above for not having any indistinguishable initialisms.

Chapter 1

Introduction

1.1 Quantum Mechanics and Electronic Structure

In the early twentieth century, physicists were faced with a number of observed phenomena [1, 2] which were in conflict with the understanding of the time. This conflict resulted in one of the greatest and most profound scientific paradigm shifts ever, quantum mechanics.[3–11] One of the principles of quantum mechanics is that both matter and light behave simultaneously as both particles and waves.[12] The time-independent wave equation for particles, the time-independent Schrödinger equation, may be written down as:

$$\hat{H}\,|\Psi\rangle = E\,|\Psi\rangle \tag{1.1}$$

where $\hat{H}$ is the Hamiltonian, the sum of the kinetic and potential energy operators, $|\Psi\rangle$ is the eigenfunction of the operator, known as the wavefunction, which describes all the properties of the system, and E is the energy of the system. Equation 1.1 and its time-dependent counterpart may be used to describe any physical system, even classical systems, due to the quantum-classical correspondence principle. This being said, the Schrödinger equation has limited applicability for large systems because quantum effects quite often thermally average out and more critically these equations are too difficult to solve for such systems. These properties limit the study of quantum mechanics to roughly nanoscale materials.

One of the most successful applications of quantum mechanics is the study of the electrons in molecules and materials, a field known as electronic structure.[13] In electronic structure, the most fundamental simplification is the Born-Oppenheimer approximation[14], in which one solves the time-independent Schrödinger equation for the electrons in the field of fixed nuclei. Mathematically, this results in a separation of the variables into electronic and nuclear degrees of freedom. The Born-Oppenheimer approximation may be justified by invoking the different time-scales of the response of the two type of particles. Electrons have approximately 2000 times less mass than the nuclei they orbit resulting in much faster motion per unit force. Nuclear motion occurs on the pico-to-femto-second time scale because of their large mass, whereas electronic motions occur on the femto-to-atto-second time scale.

Thus, the nuclear motions may be viewed as responses to changes in the "instantaneous" movement of the electrons. Another way of saying this is that motions of the electrons only depend parametrically on the positions of the nuclei. After applying the Born-Oppenheimer approximation to any system of electrons and nuclei, one may solve the electronic time-independent Schrödinger equation independent of the nuclei:

$$\hat{H}_{\text{elec}} \left|\Psi_{\text{elec}}\right\rangle = E_{\text{elec}} \left|\Psi_{\text{elec}}\right\rangle \tag{1.2}$$

$$\hat{H}_{\text{elec}} = -\sum_i \frac{1}{2}\nabla_i^2 - \sum_i \sum_A \frac{Z_A}{r_{iA}} + \sum_i \sum_{i<j} \frac{1}{r_{ij}} \tag{1.3}$$

where the electronic Hamiltonian is a sum of the kinetic energy of the electrons, i, their potential energy with respect to the nuclei, A, and the energy associated with the interactions between electrons. Most, if not all, of electronic structure may be boiled down to the solving of this equation, which is typically the starting point for many other areas of theoretical chemistry including descriptions of nuclear dynamics and solutions to the time-dependent Schrödinger equation.

We have now defined the Hamiltonian, one component necessary for solving Equation 1.2, but have not yet discussed the other perhaps more important component, the wavefunction ($\left|\Psi_{\text{elec}}\right\rangle$). There are many possible choices to represent the electronic wavefunction, but the most common is to represent it as an antisymmetrized product of N single-particle wavefunctions. These single-particle wavefunctions are typically written as a product of a spatial component, which represents the position of the electron, and a spin component, which represents the spin angular momentum of the electron:

$$\chi_i^{\alpha}(\tau_1) = \chi_i^{\alpha}(\mathbf{r}_1, \xi_1) = \psi_i(\mathbf{r}_1)\alpha(\xi_1) \tag{1.4}$$

$$\chi_i^{\beta}(\tau_1) = \chi_i^{\beta}(\mathbf{r}_1, \xi_1) = \psi_i(\mathbf{r}_1)\beta(\xi_1) \tag{1.5}$$

where $\mathbf{r}$ is the position and ξ is the spin angular momentum parameter. α corresponds to spin up and β corresponds to spin down (the eigenfunctions of $\hat{S}_z$) and these two functions are orthonormal:

$$\langle \alpha \,|\, \alpha \rangle = 1 \tag{1.6}$$

$$\langle \beta \,|\, \beta \rangle = 1 \tag{1.7}$$

$$\langle \alpha \,|\, \beta \rangle = 0 \tag{1.8}$$

Electrons are identical fermions and in order to make our wavefunction obey proper fermionic statistics we need the wavefunction to be anti-symmetric[15] with respect to the interchange of any two electrons positions.

$$\left|\chi_1(\tau_1)\chi_2(\tau_2)\right\rangle = -\left|\chi_1(\tau_2)\chi_2(\tau_1)\right\rangle \tag{1.9}$$

A direct product of single-particle wavefunctions does not obey anti-symmetry and thus is inappropriate to describe more than one electron. Therefore to describe multi-electronic systems we use a wavefunction which is a determinant of single-particle wavefunctions, known as a Slater determinant[16, 17]:

$$|\Phi(\tau_1,\tau_2,...,\tau_N)\rangle = (N!)^{-\frac{1}{2}} \begin{vmatrix} \chi_i(\tau_1) & \chi_j(\tau_1) & \cdots & \chi_k(\tau_1) \\ \chi_i(\tau_2) & \chi_j(\tau_2) & \cdots & \chi_k(\tau_2) \\ \vdots & \vdots & \ddots & \vdots \\ \chi_i(\tau_N) & \chi_j(\tau_N) & \cdots & \chi_k(\tau_N) \end{vmatrix} \tag{1.10}$$

which is commonly written as $|\chi_1\chi_2...\chi_N\rangle$.

1.2 Hartree–Fock and the Correlation Problem

Combining the time-independent Schrödinger equation and a single Slater determinant as the wavefunction results in the Hartree–Fock method (HF).[18–22] HF is the mean-field solution to Equation 1.2 and can be physically understood as an approximation where every electron interacts with the field created by the charge density of the other electrons. The expectation value of the Hamiltonian with respect to a single Slater determinant is the HF energy:

$$E_{\text{HF}} = \left\langle \Phi_{\text{HF}} \left| \hat{H} \right| \Phi_{\text{HF}} \right\rangle \tag{1.11}$$

$$= \sum_i \left\langle \chi_i \left| \hat{h} \right| \chi_i \right\rangle + \frac{1}{2} \sum_i \sum_j \left[\left\langle \chi_i\chi_j \left| \frac{1}{r_{ij}} \right| \chi_i\chi_j \right\rangle - \left\langle \chi_i\chi_j \left| \frac{1}{r_{ij}} \right| \chi_j\chi_i \right\rangle \right] \tag{1.12}$$

with

$$\left\langle \chi_i \left| \hat{h} \right| \chi_i \right\rangle = \int d\tau_1 \chi_i^*(\tau_1) \left[-\frac{1}{2}\nabla_i^2 - \sum_A \frac{Z_A}{r_{1A}} \right] \chi_i(\tau_1) \tag{1.13}$$

$$\left\langle \chi_i\chi_j \left| \frac{1}{r_{ij}} \right| \chi_i\chi_j \right\rangle = \int d\tau_1 d\tau_2 \chi_i^*(\tau_1)\chi_j^*(\tau_2) \frac{1}{r_{12}} \chi_i(\tau_1)\chi_j(\tau_2) \tag{1.14}$$

This is a variational method and therefore the best spin orbitals are the ones that minimize the energy, keeping the constraints imposed on the wavefunction that the spin-orbitals remain orthonormal, $\langle \chi_i \,|\, \chi_j \rangle = \delta_{ij}$. These best spin orbitals define an integro-differential equation:

$$\hat{h}(1)\chi_i(1) + \sum_{j\neq i} \left[\int d\tau_2 \chi_j^*(2) \frac{1}{r_{12}} \chi_j(2) \right] \chi_i(1) - \sum_{j\neq i} \left[\int d\tau_2 \chi_j^*(2) \frac{1}{r_{12}} \chi_i^*(2) \right] \chi_j(1) = \varepsilon_i \chi_i(1) \tag{1.15}$$

This equation is typically rewritten using the Coulomb operator:

$$\hat{J}_j(1) = \int d\tau_2 \chi_j^*(2) \frac{1}{r_{12}} \chi_j(2), \tag{1.16}$$

the Exchange operator:

$$\hat{K}_j(1)\chi_i(1) = \int d\tau_2 \chi_j^*(2) \frac{1}{r_{12}} \chi_i^*(2)\chi_j(1), \tag{1.17}$$

and the Fock operator:

$$\hat{f}(1) = \hat{h}(1) + \sum_{j \neq i} \hat{J}_j(1) - \sum_{j \neq i} \hat{K}_j(1), \tag{1.18}$$

resulting in what is more clearly an eigenvalue equation:

$$\hat{f}(1)\chi_i(1) = \varepsilon_i \chi_i(1) \tag{1.19}$$

In order to solve this equation numerically, we expand the spatial component of the single-particle wavefunctions in a basis of M atomic orbitals (AO), $|\omega_\mu(\mathbf{r})\rangle$, which are known and have been optimized to obtain specific atomic properties:

$$|\phi_i\rangle = |\omega_\mu\rangle \, C_{\cdot i}^{\mu \cdot} \tag{1.20}$$

In this equation we have employed the Einstein summation convention and the tensor notation with both covariant (subscript) and contravariant (superscript) indices of Head-Gordon et al.[23], and the convention that single-particle wavefunctions, henceforth molecular orbitals (MOs) will be indexed by Roman letters, i, and AO will be indexed by lower case Greek letters, μ. By substituting the expansion (Equation 1.20) into Equation 1.19, integrating out the spin components, and multiplying by $\langle\omega_\nu|$, the integro-differential equation becomes a matrix equation:

$$\langle \omega_\mu \, | f(1) | \, \omega_\nu \rangle \, C_{\cdot i}^{\nu \cdot} = \varepsilon_i \, \langle \omega_\mu \, | \, \omega_\nu \rangle \, C_{\cdot i}^{\nu \cdot} \tag{1.21}$$

$$\int d\mathbf{r}_1 \omega_\mu(1) f(1) \omega_\nu(1) C_{\cdot i}^{\nu \cdot} = \varepsilon_i \int d\mathbf{r} \omega_\mu(1) \omega_\nu(1) C_{\cdot i}^{\nu \cdot} \tag{1.22}$$

$$F_{\mu\nu} C_{\cdot i}^{\nu \cdot} = \varepsilon_i S_{\mu\nu} C_{\cdot i}^{\nu \cdot} \tag{1.23}$$

$$\mathbf{FC} = \mathbf{SC}\varepsilon \tag{1.24}$$

This matrix eigenvalue problem, called the Roothaan-Hall equation, is easily solvable on a computer, but because the Fock matrix ($\mathbf{F}$) depends on the functions of all the electrons, Equation 1.18, and solving Equation 1.24 gives us those functions, this becomes an iterative non-linear process. The spin integration done to arrive at Equation 1.24 assumes that each pair of spin functions has the same spatial component, restricted Hartree–Fock (RHF); these equations may be rederived without this assumption and one arrives at a similar set

of equations known as the Pople-Nesbet equations yielding the unrestricted Hartree–Fock (UHF) formalism.[24]

The AO basis is typically larger than the number of electrons in the system and thus solving Equation 1.24 provides us with functions which are unoccupied (virtual) functions; these functions will be important later and will be labeled for the rest of the work with Roman letters starting from a $(a, b, c, ...)$.

Despite HF typically recovering 99% of the total energy of a system and often being qualitatively correct, the remaining 1% of energy is crucial for understanding interesting questions in chemical systems including relative energies, bond-breaking processes, and van der Waals interactions. This missing energy is attributable to the fact that electrons do not just interact via their charge densities but have interactions that are "instantaneous" repulsions. The difference between the HF energy and the exact non-relativistic energy is termed the correlation energy, because it deals with how electronic motions are correlated. There are many different treatments to obtain approximate correlation energies and most of electronic structure theory is devoted to calculating this quantity.

1.3 Density Functional Theory

The most commonly used class of methods for solving the correlation problem is known as density functional theory (DFT); in fact, 80-90% of electronic structure calculations today use these methods. The Hohenberg-Kohn theorems[25] constitute the theoretical framework of DFT; they state that the ground state electron density, $n(\mathbf{r})$, uniquely defines the potential of a system and the ground state energy may be written as the minimum of a functional of the real space density:

$$E\left[n(\mathbf{r})\right] = \int d\mathbf{r} v_{\text{ext}}(\mathbf{r}) n(\mathbf{r}) + \frac{1}{2}\int\int d\mathbf{r} d\mathbf{r}' \frac{n(\mathbf{r})n(\mathbf{r}')}{|\mathbf{r}-\mathbf{r}'|} + G\left[n(\mathbf{r})\right] \tag{1.25}$$

$$\tag{1.26}$$

Here, $v_{\text{ext}}(\mathbf{r})$ is the external potential from electron-nuclei interactions, the second term is the classical Coulombic interaction and G is a universal functional defined as:

$$G\left[n(\mathbf{r})\right] = T\left[n(\mathbf{r})\right] + V_{\text{ee}}\left[n(\mathbf{r})\right] - \frac{1}{2}\int\int d\mathbf{r} d\mathbf{r}' \frac{n(\mathbf{r})n(\mathbf{r}')}{|\mathbf{r}-\mathbf{r}'|} \tag{1.27}$$

where T is a kinetic energy functional, V_{ee} is a functional which represents all electron-electron interactions (from which we have subtracted the known classical Coulombic interaction so as not to double count). The Hohenberg-Kohn mapping is powerful because the exact wavefunction consists of an exponentially growing number of variables whereas the density is a function of Euclidean three-space.

Despite the power of these theorems, finding a form of this functional (G) proved difficult and it was not until the Kohn-Sham equations were introduced that DFT became a viable

solution to the correlation problem. The Kohn-Sham equations[26] involve expressing the problem as a system of non-interacting electrons in an effective potential which reproduces the true density of the system.

$$E\left[n(\mathbf{r})\right] = T_s\left[n(\mathbf{r})\right] + \int d\mathbf{r} v_{\text{ext}}(\mathbf{r}) n(\mathbf{r}) + \frac{1}{2}\iint d\mathbf{r} d\mathbf{r}' \frac{n(\mathbf{r}) n(\mathbf{r}')}{|\mathbf{r} - \mathbf{r}'|} + E_{\text{xc}}\left[n(\mathbf{r})\right] \tag{1.28}$$

$$v_{\text{eff}} = v_{\text{ext}}(\mathbf{r}) + \frac{1}{2}\int d\mathbf{r}' \frac{n(\mathbf{r}')}{|\mathbf{r} - \mathbf{r}'|} + \frac{\delta E_{\text{xc}}\left[n(\mathbf{r})\right]}{\delta n(\mathbf{r})} \tag{1.29}$$

$$v_{\text{xc}} = \frac{\delta E_{\text{xc}}\left[n(\mathbf{r})\right]}{\delta n(\mathbf{r})} \tag{1.30}$$

where E_{xc} is the exchange-correlation functional. This repartitioning allows one to compute the kinetic energy of the non-interacting electrons exactly:

$$T_s\left[n(\mathbf{r})\right] = \sum_{i=1}^{N} \int d\mathbf{r} \phi_i^*(\mathbf{r}) \left(-\frac{1}{2}\nabla^2\right) \phi_i(\mathbf{r}) \tag{1.31}$$

using the Kohn-Sham orbitals $\phi_i(\mathbf{r})$ which define the Kohn-Sham eigenvalue problem:

$$\left(-\frac{1}{2}\nabla^2 + v_{\text{eff}}(\mathbf{r})\right) \phi_i(\mathbf{r}) = \varepsilon_i \phi_i(\mathbf{r}) \tag{1.32}$$

and parameterize the electron density as:

$$n(\mathbf{r}) = \sum_i |\phi_i(\mathbf{r})|^2 \tag{1.33}$$

Equating the Hohenberg-Kohn equations with those of Kohn-Sham:

$$E_{\text{HK}} = T + V_{\text{ext}} + J + (V_{\text{ee}} - J) \tag{1.34}$$

$$E_{\text{KS}} = T_s + V_{\text{ext}} + J + E_{\text{xc}} \tag{1.35}$$

$$E_{\text{xc}} = (T - T_s) + (V_{\text{ee}} - J) \tag{1.36}$$

it can be seen that E_{xc} contains the kinetic energy not described by the non-interacting electrons and all non-classical electron-electron interactions. The inability of the G of Hohenberg-Kohn to be formulated to obtain accurate kinetic energies is the reason Kohn-Sham was such an important advance; this is because T is the first large unknown term in G where as the difference $T - T_s$ is very small.

Although both Hohenberg-Kohn and Kohn-Sham present theories that are formally exact, in order to preserve this property they require the exact exchange-correlation functional, which is unknown and potentially unknowable; thus all currently applied forms of DFT utilize approximate functionals (in Kohn-Sham this involves formulations for E_{xc}). The creation and development of new and better functionals has been and continues to be the main

methodological driving force of DFT.[27, 28] Popular functional forms include (in order of increasing computational complexity): the local density approximation (LDA)[17, 29, 30], which depends only on the value of the density at a point, generalized gradient approximations (GGAs)[31–36], which depend on the value and gradient of the density in space, meta-GGAs[37–39], which depend on the kinetic energy density, hybrid functionals[40, 41] (which can be paired with any of the other forms), which contain a fraction of exact exchange, and range-separated functionals, which divide interactions into both a short and long range component[42, 43]. Also recently the addition dispersion correction[44] have become common for all forms of Kohn-Sham DFT.

The most popular forms of DFT, especially for describing chemistry, are the hybrid density functionals, with B3LYP[40] being the most popular variety of this formulation. As stated above, hybrid DFT involves adding a fraction of exact exchange as calculated by Hartree–Fock theory (Equation 1.17), but using the Kohn-Sham orbitals. Different hybrid DFT functionals include different fractions of exact exchange, where this fraction can be thought of as a way of tuning the physical content of the functional. This fraction may be justified by the adiabatic connection formula where one connects the fully interacting Hamiltonian and the Hamiltonian of the non-interacting electrons by a coupling parameter.[45] In the limit of a linear interpolation between the two Hamiltonians, one finds that there persists a fraction of exchange with the same form as HF exchange. This provides a framework for including a fraction of exact exchange but does not give a rigorous number for what fraction to use. Therefore this fraction is typically taken as a parameter to be optimized in forming E_{xc}. From a numerical viewpoint, this fraction may be justified by the fact that it is well known that HF underestimates atomization energies, where as GGA functionals overestimate these energies and thus a mixture of the two should result in better energies.[28]

DFT's ubiquitousness in electronic structure is attributable to its ability to strike a good balance between accuracy and computational cost. The most common forms of Kohn-Sham DFT scale at approximately the same cost as Hartree–Fock calculations but because they are able to include correlation effects, they are much more accurate when applied to real chemical problems. Despite these favorable features, DFT does have problems. First and foremost the exact functional is not known and thus one must choose an approximate functional for which there are inherent errors. In typical applications one tries several functionals and chooses the functional which most accurately represents the known physics of the system. Secondly, Kohn-Sham DFT, if not corrected for this deficiency, is poor at describing dispersions interactions. Third, Kohn-Sham DFT has an issue accounting for what is known as self-interaction error, a single electron is able to interact with its own density, which is entirely unphysical. Fourth, the KS framework involves only a single configuration of the electrons, which may be inappropriate to treat so-called strongly correlated problems, where multiple configurations make essential contributions.

1.4 Configuration Interaction

Another approach to tackle the correlation problem is configuration interaction (CI). In CI theory, the wavefunction is expanded as a linear combination of excited determinants, determinants where the orbitals from the HF reference are reoccupied (occupied orbitals become holes and virtual orbitals are filled):

$$|\Psi_{\mathrm{CI}}\rangle = |\Psi_{ref}\rangle + \sum_{ia} c_i^a \left|\Psi_i^a\right\rangle + \sum_{\substack{i<j \\ a<b}} c_{i_j}^{ab} \left|\Psi_{i_j}^{ab}\right\rangle + \sum_{\substack{i<j<k \\ a<b<c}} c_{ijk}^{abc} \left|\Psi_{ijk}^{abc}\right\rangle + \dots \tag{1.37}$$

If the wavefunction and energy are calculated by diagonalizing in the basis of the complete set of these excited determinants (i.e. all possible configurations of the electrons in all orbitals) then this method is known as full configuration interaction (FCI). The FCI energy is the exact solution to the electronic problem and thus it accounts for all correlation energy (in a given finite basis); in fact correlation energy itself is defined as:

$$E_{\mathrm{corr}} = E_{\mathrm{FCI}} - E_{\mathrm{HF}} \tag{1.38}$$

The reason FCI calculations are not commonly performed is that the number of components of this wavefunction grows as $\binom{M}{N}$ where M is the number of basis functions and N is the number of electrons in the system. This means that computing any property of this wavefunction including the energy requires an exponentially growing number of computations and is therefore not feasible even for relatively small systems with small basis sets.[46, 47] For this reason CI is more typically approximated using a truncated expansion[13, 48], usually based upon a rank of excitation operator:

$$|\Psi_{\mathrm{CI}}\rangle = \left(\mathbb{1} + \hat{C}_1 + \hat{C}_2 + \hat{C}_3 + \dots\right) |\Psi_{\mathrm{ref}}\rangle \tag{1.39}$$

For example CI singles (CIS) involves building the Hamiltonian in the basis of all determinants created by $\hat{C}_1$ and diagonalizing this matrix, and likewise CI singles and doubles (CISD) includes $\hat{C}_1 + \hat{C}_2$.

An important note about these truncated CIs, beyond CIS and not including FCI, are that their energies are not size-consistent.[48, 49] Size-consistency is the property that the energy evaluated on a molecular system made of two non-interacting fragments, A and B, is the same as evaluating the energy on the two fragments separately:

$$E_{\mathrm{A+B}} = E_{\mathrm{A}} + E_{\mathrm{B}} \tag{1.40}$$

If the fragments are truly non-interacting then the Hamiltonian becomes separable:

$$\hat{H} = \hat{H}_{\mathrm{A}} + \hat{H}_{\mathrm{B}} \tag{1.41}$$

In Hartree–Fock, the wavefunction may be written as the product of wavefunctions localized on each fragment.

$$\left|\Psi_{\mathrm{HF}}^{\mathrm{A+B}}\right\rangle = \left|\Psi_{\mathrm{HF}}^{\mathrm{A}}\right\rangle \left|\Psi_{\mathrm{HF}}^{\mathrm{B}}\right\rangle \tag{1.42}$$

A wavefunction with this property is known as multiplicatively separable and is always size consistent:

$$E^{\mathrm{A+B}} = \frac{\left\langle \Psi^{\mathrm{A+B}} \left| \hat{H}_{\mathrm{A}} + \hat{H}_{\mathrm{B}} \right| \Psi^{\mathrm{A+B}} \right\rangle}{\left\langle \Psi^{\mathrm{A+B}} \mid \Psi^{\mathrm{A+B}} \right\rangle} \tag{1.43}$$

$$= \frac{\left\langle \Psi^{\mathrm{A}} \right| \left\langle \Psi^{\mathrm{B}} \right| \hat{H}_{\mathrm{A}} + \hat{H}_{\mathrm{B}} \left| \Psi^{\mathrm{A}} \right\rangle \left| \Psi^{\mathrm{B}} \right\rangle}{\left\langle \Psi^{\mathrm{A}} \right| \left\langle \Psi^{\mathrm{B}} \right| \Psi^{\mathrm{B}} \rangle \left| \Psi^{\mathrm{A}} \right\rangle} \tag{1.44}$$

$$= \left\langle \Psi^{\mathrm{A}} \left| \hat{H}_{\mathrm{A}} \right| \Psi^{\mathrm{A}} \right\rangle + \left\langle \Psi^{\mathrm{B}} \left| \hat{H}_{\mathrm{B}} \right| \Psi^{\mathrm{B}} \right\rangle \tag{1.45}$$

The CI wavefunctions for each calculation are:

$$\left| \Psi^{\mathrm{A}}_{\mathrm{CI}} \right\rangle = (\mathbb{1} + \hat{C}) \left| \Psi^{\mathrm{A}}_{\mathrm{ref}} \right\rangle \tag{1.46}$$

$$\left| \Psi^{\mathrm{B}}_{\mathrm{CI}} \right\rangle = (\mathbb{1} + \hat{C}) \left| \Psi^{\mathrm{B}}_{\mathrm{ref}} \right\rangle \tag{1.47}$$

$$\left| \Psi^{\mathrm{A+B}}_{\mathrm{CI}} \right\rangle = (\mathbb{1} + \hat{C}) \left| \Psi^{\mathrm{A+B}}_{\mathrm{ref}} \right\rangle \tag{1.48}$$

The energies for the two fragments are:

$$E^{\mathrm{A}} = \frac{\left\langle \Psi^{\mathrm{A}}_{\mathrm{CI}} \left| \hat{H}_{\mathrm{A}} \right| \Psi^{\mathrm{A}}_{\mathrm{CI}} \right\rangle}{\left\langle \Psi^{\mathrm{A}}_{\mathrm{CI}} \mid \Psi^{\mathrm{A}}_{\mathrm{CI}} \right\rangle} \tag{1.49}$$

$$E^{\mathrm{B}} = \frac{\left\langle \Psi^{\mathrm{B}}_{\mathrm{CI}} \left| \hat{H}_{\mathrm{B}} \right| \Psi^{\mathrm{B}}_{\mathrm{CI}} \right\rangle}{\left\langle \Psi^{\mathrm{B}}_{\mathrm{CI}} \mid \Psi^{\mathrm{B}}_{\mathrm{CI}} \right\rangle} \tag{1.50}$$

The energy of the combined system is:

$$E^{\mathrm{A+B}} = \frac{\left\langle \Psi^{\mathrm{A+B}}_{\mathrm{CI}} \left| \hat{H}_{\mathrm{A}} + \hat{H}_{\mathrm{B}} \right| \Psi^{\mathrm{A+B}}_{\mathrm{CI}} \right\rangle}{\left\langle \Psi^{\mathrm{A+B}}_{\mathrm{CI}} \mid \Psi^{\mathrm{A+B}}_{\mathrm{CI}} \right\rangle} \tag{1.51}$$

The numerator of Equation 1.51 is:

$$\left\langle \Psi^{\mathrm{A+B}}_{\mathrm{CI}} \left| \hat{H}_{\mathrm{A}} + \hat{H}_{\mathrm{B}} \right| \Psi^{\mathrm{A+B}}_{\mathrm{CI}} \right\rangle = \left\langle \Psi^{\mathrm{A+B}}_{\mathrm{HF}} \left| \hat{H}_{\mathrm{A}} + \hat{H}_{\mathrm{B}} \right| \Psi^{\mathrm{A+B}}_{\mathrm{HF}} \right\rangle \tag{1.52}$$

$$+ \left\langle \Psi^{\mathrm{A+B}}_{\mathrm{HF}} \left| \left(\hat{C}_{\mathrm{A}} + \hat{C}_{\mathrm{B}} \right) \left(\hat{H}_{\mathrm{A}} - E^{\mathrm{A}}_{\mathrm{HF}} \right) \left(\hat{C}_{\mathrm{A}} + \hat{C}_{\mathrm{B}} \right) \right| \Psi^{\mathrm{A+B}}_{\mathrm{HF}} \right\rangle \tag{1.53}$$

$$+ \left\langle \Psi^{\mathrm{A+B}}_{\mathrm{HF}} \left| \left(\hat{C}_{\mathrm{A}} + \hat{C}_{\mathrm{B}} \right) \left(\hat{H}_{\mathrm{B}} - E^{\mathrm{B}}_{\mathrm{HF}} \right) \left(\hat{C}_{\mathrm{A}} + \hat{C}_{\mathrm{B}} \right) \right| \Psi^{\mathrm{A+B}}_{\mathrm{HF}} \right\rangle \tag{1.54}$$

$$= E^{\mathrm{A}}_{\mathrm{HF}} + \left\langle \Psi^{\mathrm{A}}_{\mathrm{HF}} \left| \hat{C}_{\mathrm{A}} \left(\hat{H}_{\mathrm{A}} - E^{\mathrm{A}}_{\mathrm{HF}} \right) \hat{C}_{\mathrm{A}} \right| \Psi^{\mathrm{A}}_{\mathrm{HF}} \right\rangle \tag{1.55}$$

$$+ E^{\mathrm{B}}_{\mathrm{HF}} + \left\langle \Psi^{\mathrm{B}}_{\mathrm{HF}} \left| \hat{C}_{\mathrm{B}} \left(\hat{H}_{\mathrm{B}} - E^{\mathrm{B}}_{\mathrm{HF}} \right) \hat{C}_{\mathrm{B}} \right| \Psi^{\mathrm{B}}_{\mathrm{HF}} \right\rangle \tag{1.56}$$

$$= \left\langle \Psi^{\mathrm{A}}_{\mathrm{CI}} \left| \hat{H}_{\mathrm{A}} \right| \Psi^{\mathrm{A}}_{\mathrm{CI}} \right\rangle + \left\langle \Psi^{\mathrm{B}}_{\mathrm{CI}} \left| \hat{H}_{\mathrm{B}} \right| \Psi^{\mathrm{B}}_{\mathrm{CI}} \right\rangle \tag{1.57}$$

which at first seems to imply that the CI energy is size consistent but we still need to simplify the denominator of Equation 1.51:

$$\left\langle \Psi_{\mathrm{CI}}^{\mathrm{A+B}} \mid \Psi_{\mathrm{CI}}^{\mathrm{A+B}} \right\rangle = 1 + \left\langle \Psi^{\mathrm{A_{HF}}} \left| \hat{C}_{\mathrm{A}} \hat{C}_{\mathrm{A}} \right| \Psi^{\mathrm{A_{HF}}} \right\rangle + \left\langle \Psi_{\mathrm{HF}}^{\mathrm{B}} \left| \hat{C}_{\mathrm{B}} \hat{C}_{\mathrm{B}} \right| \Psi_{\mathrm{HF}}^{\mathrm{B}} \right\rangle \tag{1.58}$$

$$= \left\langle \Psi_{\mathrm{CI}}^{\mathrm{A}} \mid \Psi_{\mathrm{CI}}^{\mathrm{A}} \right\rangle + \left\langle \Psi_{\mathrm{CI}}^{\mathrm{B}} \mid \Psi_{\mathrm{CI}}^{\mathrm{B}} \right\rangle - 1 \tag{1.59}$$

Clearly, the numerator and the denominator do not equal the sum of Equation 1.49 and Equation 1.50 and the energy is therefore not size consistent.

1.5 Alternative Correlation Methods

In the later chapters, we will be discussing results calculated using both DFT and CI, but these are not the only methods for calculating correlation energies.

Møller Plesset Perturbation Theory

One popular method in electronic structure is Møller–Plesset perturbation theory (MPPT), which is derived using Rayleigh-Schrödinger many-body perturbation theory[50], with the HF wavefunction as the zeroth order wavefunction. The most widely used form of MPPT is second order Møller–Plesset perturbation Theory (MP2), which contains the second-order energy correction in the perturbative series. The expression for the MP2 energy is:

$$E^{(2)} = -\frac{1}{4} \sum_{ijab} \frac{|\langle ij \,||\, ab \rangle|^2}{\varepsilon_a + \varepsilon_b - \varepsilon_i - \varepsilon_j} \tag{1.60}$$

where i, j and a, b are the canonical occupied and virtual orbitals respectively, ε are the eigenvalues from Equation 1.19, and we have used short hand for the two electron integrals:

$$\langle pq \,||\, rs \rangle = \int\int d\tau_1 d\tau_2 \phi_p(\tau_1)\phi_q(\tau_2) \frac{1}{|\mathbf{r}_2 - \mathbf{r}_1|} \left[\phi_r(\tau_1)\phi_s(\tau_2) - \phi_s(\tau_1)\phi_r(\tau_2)\right] \tag{1.61}$$

Since MP2 is a perturbative treatment, it has difficulty when the mean-field solution is a poor reference (i.e. the perturbation is large). Also, MPPT lacks a variational principle (the energy computed is not an upper bound to the exact energy). This can easily be seen as the denominator of Equation 1.60 approaches zero.

Coupled-Cluster Theory

Another set of methods for computing the correlation energy are the Coupled-Cluster (CC) family of methods, which were developed first by the nuclear physics community,[51] and eventually brought to quantum chemistry[49, 52–57], where they transformed what could

be done in terms of accuracy. In CC, the wavefunction is represented using an exponential ansatz:

$$|\Phi_{\mathrm{CC}}\rangle = e^{\hat{T}} |\Phi_0\rangle \tag{1.62}$$

where $|\Phi_0\rangle$ is typically the HF wavefunction and $\hat{T}$ is the cluster operator defined as:

$$\hat{T} = \sum_{\kappa}^{N} \hat{T}_\kappa \tag{1.63}$$

with

$$\hat{T}_\kappa = \frac{1}{(\kappa!)^2} \sum_{i,b} t_{i_1,i_2,\ldots,i_\kappa}^{b_1,b_2,\ldots,b_\kappa} \hat{a}_{b_\kappa}^t \ldots \hat{a}_{b_1}^t \hat{a}_{i_1} \ldots \hat{a}_{i_\kappa} \tag{1.64}$$

Here t are amplitudes, the $\hat{a}_{b_1}^t$ represents a creation operator, and $\hat{a}_{i_1}$ represents an annihilation operator. In order to solve for the t-amplitudes and the energy, one left projects and solves the resulting system of equations. Just like in CI theory, CC is always truncated at a given excitation level. Typical truncations are CCD ($\kappa = 2$) or CCSD ($\kappa = 1, 2$) and CCSDT ($\kappa = 3$), where most often because of its large computation cost the triples operator is handled perturbatively, (T). CC is one of the most accurate electronic structure methods, CCSD(T) being often referred to as the "gold-standard" in quantum chemistry. In contrast to the CI expansion shown before, the exponential ansatz of CC theory preserves size-consistency and size-extensivity, but these methods do suffer from a lack of a variational principle, just like MP2 does.

Spin-Flip Methods

Another family of methods for solving the correlation problem are the spin-flip (SF) methods, which have been used in conjunction with configuration interaction (CI)[58], DFT[59], and CC[60] frameworks. These methods begin with a high-spin reference and then employ linear combinations of spin-flipping excitations ($\alpha \rightarrow \beta$) to access states with the desired M_s value, such as the ground state. An important variant of the spin-flipping idea is the restricted active space spin-flip configuration interaction family of methods (RAS-SF)[61–63]. RAS-SF include general numbers of spin-flips and uses RAS techniques to include larger active spaces (a chosen set of occupied and virtual orbitals). In RAS-SF, the orbital space is partitioned into three sets: RAS I, II and III. The RAS II space contains the singly occupied orbitals of ROHF and full CI is performed in this space, which is usually limited to a relatively small number of electrons and orbitals, because of the exponential scaling. Excitations to and from the three spaces may then performed at a given level of excitation, so called hole and particle excitations. Despite their success, the RAS-SF methods still suffer from some deficiencies: the excitation energies can be sensitive to the quality of the high-spin reference, these methods lack a full treatment of dynamic correlation, and these methods have exponential scaling with respect to active space size.

Complete Active Space Self-Consistent-Field

Another important technique for evaluating the correlation energy is the complete active space self-consistent-field (CASSCF) method[64], and its second-order perturbation-corrected variant (CASPT2)[65]. CASSCF involves optimizing the orbitals over all the configurations within an active space and is mathematically equivalent to performing FCI in this space. In practice, the active space is limited to a few important orbitals and electrons, which makes the method tractable for much larger systems than FCI, but eventually the exponential scaling with the size of this active space makes the method computationally infeasible. The Density Matrix Renormalization Group (DMRG)[66] is the most promising recent development for reducing the exponential scaling of CASSCF. DMRG is an algorithm which replaces the CI solver in the CASSCF problem and is able reduce the scaling with respect to active space to non-exponential for pseudo-linear systems. The exponential cost does reappear when DMRG-CASSCF is applied to fully 3-dimensional systems, but still shows favorable scaling with respect to traditional CASSCF solvers.

Chapter 2

Localized Orbital Bonding Analysis

2.1 Introduction

Molecular transition metal based catalytic complexes are a ubiquitous motif in modern chemistry from biologically inspired catalysts to industrial applications. These catalysts often have complicated reaction cycles with transitory but important intermediates.

One property commonly used in analysis of these complexes is oxidation state. Oxidation state while formally defined but not often very useful in main-group elements, is of great importance in transition metal compounds. The properties of the various oxidation states are often very different, and being able to determine oxidation states is an important aspect of electrochemistry, and therefore catalysis.[67] With simple ligands, the oxidation states of transition metals can be determined from the stoichiometry and electronegativities of a complex and its salts.[68] However, in cases where there are complex or even bridging ligands, or when the complex is involved in catalysis, the assignment of oxidation state can be unclear.

In transition metal complexes, geometry is often indicative of oxidation state; the Bond Valence Sum (BVS) method has been recently used, particularly in the Cambridge Structural Database[69, 70], to characterize the oxidation state of metal complexes[71]. This method uses the distance between the metal and the ligand to determine the oxidation state, but relies heavily on so called R_0 parameters which are empirically determined from bond lengths of complexes with known oxidation states. The R_0 values have two problems: first they depend on both atoms which make up the bond, which limits their ability to be applied to systems with new bonding partners, and secondly they do not characterize species with bulky ligands and low coordination numbers[72], which may be the case for catalytic compounds.

In general both geometry and oxidation state are direct consequences of the electronic structure of the compound and thus it seems preferable to use the electronic structure to define the oxidation state rather than the geometry, a correlated observable. However, computationally and quantum mechanically, oxidation states suffer from a lack of rigorous definition and thus many different techniques for calculating approximate oxidation states

have been proposed. One of the earliest and simplest approaches is Mulliken population analysis[73–76], and the related Mayer Bonding analysis[77–79], but these suffer heavy dependences on the basis sets chosen. As an alternative, Löwdin population analysis[80, 81] shows reduced basis set dependence with the same essential features. While these total electron populations can be used to give an indication of oxidation state of a transition metal, as they do change with oxidation and reduction, the charges given are often much lower than the formal oxidation states of the metal, and without careful calibration are very difficult to interpret. Analysis of the spin populations on atoms in the molecule can also be used in some cases to determine oxidation states, but still requires some calibration, and is problematic in low spin systems. Recently it was argued that atomic charges should not be used as a measure of the oxidation state of a metal because this value is highly dependent on the ligands involved and less to do with oxidation state of the transition metal.[68]

A different route which has developed in order to treat similar problems are bond analyses. These methods typically characterize bonding within molecules and then use those characterizations to calculate the oxidation state by assigning electrons to the ligand or the metal. Methods of increasing levels of complexity have been developed, leading to the Natural Bonding Orbital (NBO) analysis[82–84], methods based on local spin[85–89], and topological approaches such as Electron Localization Functions[90] and Bader's Atoms-in-Molecules[91, 92] and related approaches. These methods require some levels of sophisticated analysis of the density to extract chemically meaningful information.

Despite these advances, the problem of determining the oxidation state of a metal in such complexes is still left without a satisfactory solution.

2.2 Localized Orbital Bonding Analysis

We propose an alternative, much simpler, bonding analysis, which accurately predicts the oxidation state of transition metal complexes. The method is based on the concept of localized orbitals, stemming from an analysis of Cu-P-Cu-P diamondoids by Rhee and Head-Gordon[93]. The canonical molecular orbitals, produced by traditional theoretical methods, are often extremely delocalized, and from them the bonding in even relatively small molecules can be difficult to interpret. Within single determinant methods like Density Functional Theory (DFT) and Hartree–Fock (HF) Theory, mixing amongst the occupied orbitals does not change the density or the energy, and we may produce localized orbitals by this mixing process. The sets of localized orbitals produced correspond to the lone pairs, non-bonding orbitals, single, double and triple bonds which make up the language of chemistry.

A number of localization procedures have been applied over the years, among them Boys orbitals[94], which minimize the radial extent of each orbital, Pipek-Mezey (PM) orbitals[95, 96], which maximize the locality of the projected population, and Edmiston-Ruedenberg (ER) orbitals[97], which maximize the electrostatic self-interaction of each orbital. In particular the latter ER orbitals may be thought of as producing the most 'classical' orbitals, as by maximizing the the exchange self-interaction within an orbital, they minimize the

non-classical exchange between orbitals.[1] Each method maximizes a localization metric, Z:

$$Z_{Boys} = \sum_i \left\langle \phi_i(\mathbf{r}_1)\phi_i(\mathbf{r}_2) \left| (\mathbf{r}_1 - \mathbf{r}_2)^2 \right| \phi_i(\mathbf{r}_1)\phi_i(\mathbf{r}_2) \right\rangle \tag{2.1}$$

$$Z_{PM} = \sum_I \sum_i \left| \langle \phi_i \left| P_I \right| \phi_i \rangle \right|^2 \tag{2.2}$$

$$Z_{ER} = \sum_i \left\langle \phi_i(\mathbf{r}_1)\phi_i(\mathbf{r}_2) \left| \frac{1}{|\mathbf{r}_1 - \mathbf{r}_2|} \right| \phi_i(\mathbf{r}_1)\phi_i(\mathbf{r}_2) \right\rangle, \tag{2.3}$$

where ϕ_i are occupied orbitals, I labels atoms and P_I is the Mulliken projection operator on a particular atom. Each of these methods, while differing in computational complexity, produces sets of localized orbitals, which correspond to the lone pairs, non-bonding orbitals, single, double and triple bonds which make up the language of chemistry.

By combining these methods with a population analysis, we find that bonds and oxidation states can be easily determined, in accordance with chemical intuition. To extract chemical information from localized orbitals, it is convenient to decompose each orbital into contributions upon atoms. The most obvious means of such decomposition are the same methods discussed before Mulliken and Löwdin population analyses, which are commonly used for the complete density, but have not been commonly applied to localized orbitals. As these are linear projections of the density, and the density is additive from the orbitals, the sum of all orbital contributions will result in the value for the total density.

If a molecule were to consist of ideal covalent bonds, we would expect the localized orbitals to fall into three categories: core orbitals, which form a complete shell and are fully localized; bonding orbitals, which contain contributions from two atoms, weighted in some way owing to differences in electronegativity; and non-bonding orbitals which are again completely local but formed from valence rather than core electrons. In practice, core electrons are usually very well localized, and can be easily distinguished, leaving any remaining well-localized orbitals as non-bonding orbitals.

More complicated bonding situations, such as delocalized electrons and ligand donation will cause orbitals to be spread over more sites, and so the distinction between these types becomes blurred. In these complicated situations use of the values of the projections themselves can provide additional insight into the bonding. In the subsequent sections we have applied these methods to a series transition metal complexes to validate the effectiveness of this analysis and to demonstrate how the method relates to bonding. We conclude with an application to a potential water oxidation catalyst, showing the location of the successive oxidations along part of a proposed catalytic cycle.

[1] The self-interaction energy is an unphysical contribution to the energy from allowing electrons to interact with themselves. In HF Theory, the Coulomb and exchange self-interactions exactly cancel. The residual self-interaction in many DFT methods is a well-known problem.

Computational Details

In this section we detail the computational methods used for calculation on Mn complexes. All calculations were performed in a customized version of the Q-Chem package[98]. Beginning with the crystal structure of the nitrate salt of **X** the structure of **O** was created by deletion and transmutation of the appropriate atoms. Experimental magnetic measurements[99] indicate a very slight (-36.6 cm$^-$1) antiferromagnetic coupling between the Mn atoms, resting in a singlet ground state. As the coupling is so slight, calculations were performed on both high- and low-spin complexes ($M_s = 3, 0$).

Initial guess densities were produced by the superposition of converged ligand and Mn_2O_2 fragment calculations with a 3-21G basis set, as the minimal basis STO-3G was not found to reliably converge to the correct state. Unrestricted SCF calculations were converged with the Relaxed Constraints Algorithm[100, 101], until a threshold of 10^{-3}, followed by Geometric Direct Minimization[102]. Functionals were calculated using a grid with 70 radial and 302 Lebedev angular points, as smaller grids led to intolerable inconsistencies between gradient and energy evaluations, and between Hessian and gradient. Density Functional Theory (DFT)[25, 103] in its formulation due to Kohn and Sham[26] was used for all calculations. As the accuracy of DFT functionals is not well-calibrated for systems such as these, we have used three functionals with differing treatments of exchange, B3LYP[40], BP86[33, 104], and ωB97X-D[43, 105], and agreement of results from these different functionals gives some confidence in the transferability of the results. Reliable convergence of the SCF calculations in these systems was found to be extremely difficult, and sensitive to the initial guess and convergence method used. Once a stationary point was found, it was subjected to stability analysis[106] and if a saddle point was found, the SCF was restarted after a step in a downhill direction. Geometries were then successively optimized with bases of 3-21G[107], 6-31G[108], and 6-31G*[109], with frequency calculations performed at convergence. Saddle-points were descended from until a minimum was reached.

Because of the eccentricities of convergence, for the B3LYP functional, SCF Metadynamics[110] was performed for each optimized geometry, and a number of the excited SCF solutions had their geometry optimized. The lowest competing geometry and state was 1.6 eV above the minimum found. Localizations were performed with standard Boys and Pipek-Mezey algorithms, and the Resolution of the Identity Edmiston-Ruedenberg method of Subotnik *et al.*[111] using the RIMP2-SVP[112] basis as the auxiliary basis.

Free energies were calculated using the harmonic approximation at 298K. For BP86 and ωB97X-D functionals, there was an imaginary frequency of the order 50cm^{-1} in the vibrational analysis, corresponding to a methyl group rotation. We consider this an artifact of the numerical quadrature, and so the lowest mode of all Mn complexes was removed in the calculation of the free-energy. The maximum effect of this was a change of 0.05eV, and is not considered a significant effect. As the charge of the species remains conserved we expect gas-phase calculations to be sufficient as solvent reorganization energies are likely to be small. Relative energetics were calculated for reactions such as $\mathbf{O}^{2+}(\mathrm{g}) \longrightarrow \mathbf{A1}^{2+}(\mathrm{g}) + \mathrm{H(g)}$, and using standard experimental values[113, 114] $\Delta_f G^\circ_{298K}(\mathrm{H(g)}) = 2.11eV$ and $E^\circ(\mathrm{Ce}^{3+}(\mathrm{aq})$

Table 2.1: Mulliken populations of the metal atom for various transition metal complexes. "hs" and "ls" indicate the high-spin and low-spin configurations respectively.

	Cl^-	H_2O hs	H_2O ls	CN^-	CO
V^{II}	1.02	1.12		0.05	0.64
Mn^{II}	1.10	1.24	1.18	0.10	0.63
Mn^{III}	0.93	1.58	1.52	0.35	0.80
Fe^{II}	1.08	1.20	1.09	0.01	0.51
Fe^{III}	0.99	1.63	1.47	0.25	0.67
Ni^{II}	0.99		1.04	-0.19	0.31
Zn^{II}	1.02		1.06	-0.03	0.52

$\longrightarrow \ Ce^{4+}(aq) + e^-) = -1.72V.$

2.3 Case Studies

With the Localized Orbital Bonding Analysis, from the number of non-bonding and donating orbitals it is possible to gain a measure of the oxidation state of a metal. In this section we compare the Mulliken total and spin population analyses to both NBO analysis and LOBA for 32 complexes of common transition metals and ligands, spanning the electrochemical series. In Tables 2.1–2.5 each cell corresponds to a complex formed from the metal and six octahedrally coordinated ligands. The total charge of the complex was the combination of the formal metal ion and the charges on the ligands. Cl^- complexes were calculated as high spin, and CN^- and CO as low spin. Complexes were optimized with the B3LYP functional in Unrestricted Kohn-Sham DFT, with a 6-31G* basis.

From Table 2.1 and 2.3 it can be seen that there is no systematic relationship between Mulliken charge and oxidation state of the metals. As seen in Table 2.2 the spin population is a better predictor of oxidation state but still requires *a priori* knowledge of the electronic structure. For example the spin population of 1.09 as seen in $Fe(CN)_6^{3-}$ only indicates there are an odd number of d-electrons on the iron: either 1, 3, or 5 corresponding to oxidation states of V, III, and I respectively. In these simple cases the correct choice is apparent, but this may not hold for less intuitive systems. Also Table 2.7 shows that for the $Mn^{IV}O_2$ species the spin population does not determine the correct oxidation state, rounding to 4 unpaired spins when there are in fact only 3.

This lack of correspondence between oxidation state and these population analyses was a major driving force for the creation of a new method for oxidation state characterization. From LOBA results on a series of small molecules, it was seen that a typical homonuclear covalent bond showed the expected population of 50% on each atom, and a heteronuclear

Figure 2.1: A calibration plot for all transition metal complexes and MnO_x species studied. On the left are plots of the difference between nominal oxidation state and Mulliken total charge on the metal. A LOBA oxidation state is based on a minimum population threshold for an orbital to count as localized on a metal. The errors in the LOBA oxidation states of the metals are plotted against the threshold used. The wide plateau shows a sensible choice for this to be in the region 40-75%. Values of minimum and maximum metal orbital occupations can be found in Tables 2.1–2.6

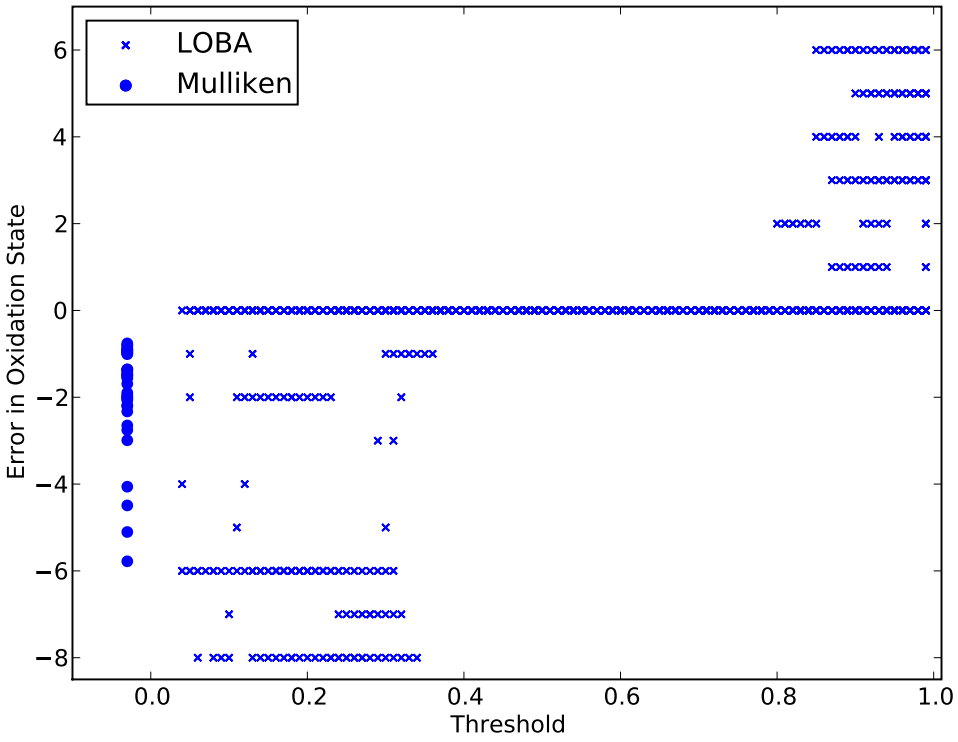

Table 2.2: Mulliken spin populations of the metal atom for various transition metal complexes. "hs" and "ls" indicate the high-spin and low-spin configurations respectively.

	Cl^-	H_2O hs	H_2O ls	CN^-	CO
V^{II}	2.97	2.99		2.84	2.79
Mn^{II}	4.96	4.88	0.99	1.08	1.07
Mn^{III}	4.25	3.85	2.04	2.10	2.15
Fe^{II}	3.93	3.86	0.00	0.00	0.00
Fe^{III}	4.27	4.43	1.00	1.09	1.13
Ni^{II}	1.87		1.83	1.69	1.66
Zn^{II}	0.00		0.00	0.00	0.00

Table 2.3: Löwdin populations of the metal atom for various transition metal complexes. "hs" and "ls" indicate the high-spin and low-spin configurations respectively.

	Cl^-	H_2O hs	H_2O ls	CN^-	CO
V^{II}	0.38	0.51		-0.57	-0.19
Mn^{II}	0.53	1.06	0.78	-0.47	-0.11
Mn^{III}	0.25	1.00	0.86	-0.24	0.13
Fe^{II}	0.49	0.69	0.45	-0.55	-0.22
Fe^{III}	0.33	1.06	0.78	-0.33	0.01
Ni^{II}	0.37		0.52	-0.46	-0.19
Zn^{II}	0.44		0.60	-0.29	-0.03

bond showed polarized populations. This implied that the analysis could also be used to discuss the nature and strength of the bonds.

In order to use LOBA to count the number of electrons on a metal it was necessary to define a limit at which any given electron should be considered localized. Figure 2.1 plots population analyses for all 32 complexes and 4 MnO_x species together listed in Tables 2.1–2.6. The complexes used were cases in which the oxidation state of the metal is well known. From this calibration plot, it can be seen there is considerable flexibility in the choice of a threshold for locality, and 60% was chosen to be close to the center of the range. With this threshold in mind calculation of oxidation states becomes intuitively obvious; take the nuclear charge and subtract one for each localized electron. Throughout this study all core orbitals were found to be fully localized and thus will not be discussed.

As a simple example of the method Figure 2.2 shows the LOBA diagram for FeF_3, a D_{3h} compound. In these diagrams each set of shapes, other than stars, represents a single

Figure 2.2: An example LOBA plot of $Fe^{III}F_3$. The symbols are explained in the text.

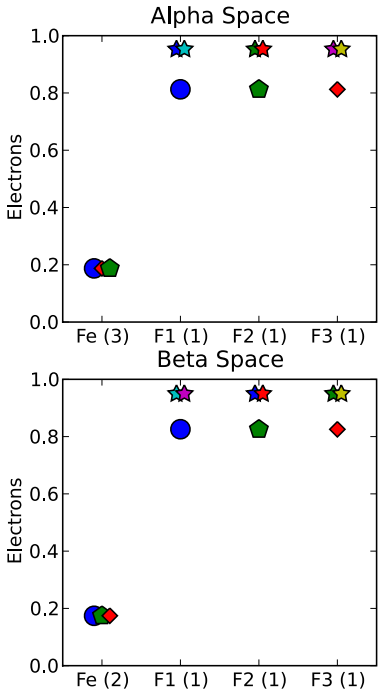

occupied localized orbital, which may be thought of as an electron. Each star represents an orbital which only has a contribution on one atomic center, e.g. the star above F1 is an electron primarily localized on that atom. The other shapes, in this case blue circles, green pentagons, and red diamonds are electrons primarily (∼80%) located on the fluorines, but with ∼20% donation to the Fe center. The numbers in parentheses to the right of the atomic symbols are the counts of valence electrons which are totally localized >90% on the atom. Therefore the oxidation state for Fe is obtained by 8 (sum of charge on nucleus and all 18 core electrons) - 3 (α-space fully localized electrons) - 2 (β-space fully localized electrons) = 3 or for the fluorines 7 - 1 - 1 (α- and β-space fully localized) - 6 (α- and β-space >60% localized) = -1.

Using this threshold, LOBA reproduces the oxidation states readily, and in addition provides information as to further electronic effects. Table 2.4 shows the maximum population on the transition metal in acceptor orbitals (population significantly less than 50%); the donation from the ligand is greater in the charged, π-donor and π-acceptor ligands. Similarly, Table 2.5 shows the minimum population on the metal of an orbital which donates to the ligands. As is chemically intuitive, only the π-acceptor ligand complexes have any significant metal-ligand donation (back-bonding). None of the complexes contained any metal-ligand

Table 2.4: Maximum occupations of metal accepting orbitals for various transition metal complexes calculated with ER/Mulliken LOBA. Where there are no acceptor orbitals (i.e. metal population < 0.05), a blank has been left. "hs" and "ls" indicate the high-spin and low-spin configurations respectively.

	Cl^-	H_2O hs	H_2O ls	CN^-	CO
V^{II}				0.19	0.16
Mn^{II}				0.20	0.18
Mn^{III}	0.23	0.06	0.13	0.23	0.22
Fe^{II}	0.05			0.20	0.19
Fe^{III}	0.14	0.07	0.09	0.24	0.23
Ni^{II}	0.07		0.07	0.20	0.18
Zn^{II}	0.12			0.16	0.25

orbitals of a covalent nature (populations close to 50%). Using a Löwdin population analysis rather than a Mulliken gave very little difference, aside from small changes in atomic populations of local orbitals.

It is also possible to perform LOBA on top of an NBO analysis, by considering the contribution on an atom from a natural orbital to be the product of the population of the natural orbital and its percentage projection on that atom. Such analysis led to somewhat similar results, with the number of localized orbitals being correctly calculated. The nature of the metal-ligand bonding differed however, as in a number of systems (notably Fe^{III} and Mn^{III} complexes with Cl^-, CN^-, and CO) displayed an asymmetry, with three metal-ligand bonds and three partially occupied orbitals localized on the remaining ligands. In contrast, all of the LOBA results exhibited the correct symmetry of the complexes.

We have also investigated the oxidation states of the manganese oxides for later comparison with a Mn-oxo complex. The MnO_x species studied behave in a very similar manner to the transition metal complexes. None of the species had any donor orbitals, all localized electrons had populations $> 99\%$, and totaling the localized orbitals gave exactly the oxidation state expected, unlike the summed Mulliken charges on the metals (see Table 2.7 and Ref. [115]). The maximum populations of the acceptor orbitals on Mn is given in Table 2.6. During this investigation MnO_3^- and MnO_4^- were first found to converge to excited states corresponding to Mn^{III} and Mn^{V} respectively. While the Mulliken charges were not helpful in determining that this had happened (being 0.53 and 0.86 respectively, compared to the final results in Table 2.7), LOBA readily detected the wrong oxidation states and enabled the correct solution to be found.

Table 2.5: Minimum occupations of metal donating orbitals for various transition metal complexes calculated with ER/Mulliken LOBA. Where there are no donating orbitals (i.e. metal population > 0.95), a blank has been left. "hs" and "ls" indicate the high-spin and low-spin configurations respectively.

	Cl^-	H_2O hs	H_2O ls	CN^-	CO
V^{II}				0.88	0.87
Mn^{II}				0.81	0.80
Mn^{III}				0.87	0.90
Fe^{II}				0.85	0.86
Fe^{III}				0.90	0.92
Ni^{II}					
Zn^{II}					

Table 2.6: Maximum occupations of metal accepting orbitals for various manganese oxide ions calculated with Mulliken LOBA for the three localization schemes Boys, ER and PM, and separately a NBO/LOBA analysis.

	Boys	PM	ER	NBO
$Mn^{IV}O_2$	0.32	0.39	0.32	0.48
$Mn^{V}O_3^-$	0.29	0.36	0.29	0.33
$Mn^{VI}O_4^{2-}$	0.29	0.37	0.33	0.33
$Mn^{VII}O_4^-$	0.34	0.35	0.35	0.34

Table 2.7: Mulliken and Löwdin total population and spin analyses on the Mn atom for various manganese oxide ions.

	Total	Spin	Löwdin
$Mn^{IV}O_2$	1.01	3.88	0.73
$Mn^{V}O_3^-$	0.94	2.05	0.51
$Mn^{VI}O_4^{2-}$	0.90	1.10	0.36
$Mn^{VII}O_4^-$	1.22	0.00	0.57

Figure 2.3: (a) **X**, a potential catalyst for water oxidation; (b) **O**, an analogue of **X** with bipyridine ligands replaced by ethandiimines.

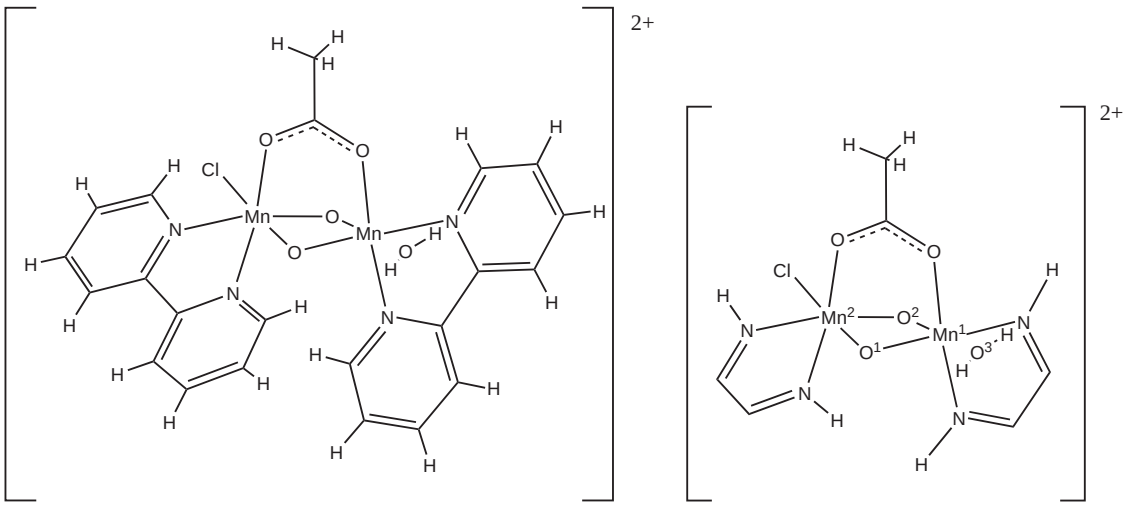

(a) **X** (b) **O**

2.4 A Model Water Oxidation Catalyst

The design of an efficient water oxidation catalyst is an important goal in the quest for renewable energy sources.[116, 117] The Oxygen Evolving Complex (OEC) of Photosystem II contains four oxo-bridged Mn centers and serves this function with four proton-coupled electron transfers, although the precise mechanism is not known. In particular, the oxidation states of the active Mn atoms in the latter stages of the catalytic cycle are uncertain[99, 118–121], and there has been much interest in the accurate modeling of such systems in the protein environment or in analogous molecules[120, 122–126].

In this section we consider a simpler catalyst with two manganese atoms bridged by two oxygen atoms, **X**, following the motifs of the OEC's structure. We investigate part of a possible catalytic cycle for water oxidation using this complex, and use LOBA to determine the location of the oxidations in this cycle.

Figure 2.3 shows the proposed resting state of the catalyst **X**. For computational convenience, we have replaced the bulky bipyrimidine ligands with ethandiimine ligands as their role is thought to be primarily that of steric protection. The model complex, **O** is also shown in Figure 2.3. The proposed catalytic cycle (Figure 2.4) involves two proton-coupled electron transfers, followed by an O-O bond formation, and the subsequent oxidation to form and release O_2, and is based on studies of similar complexes[127, 128] We have studied

Figure 2.4: Proposed catalytic cycle for water oxidation.

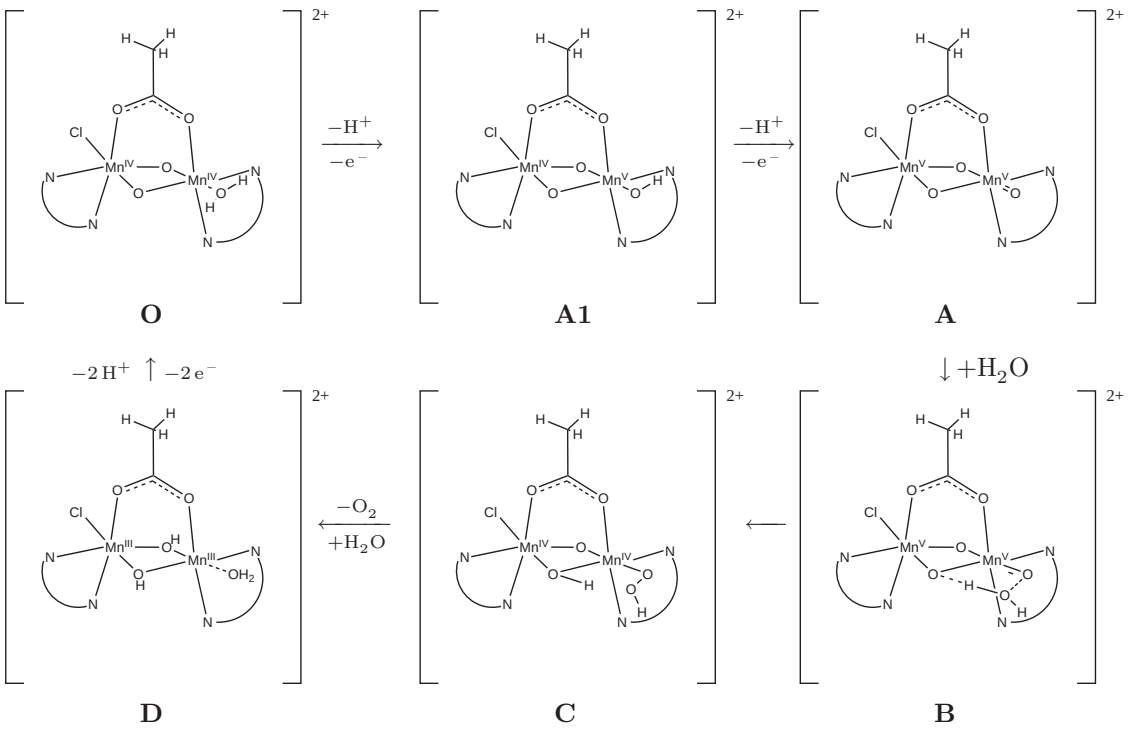

intermediates **O** to **B** to elucidate the locations of the initial oxidations.

Table 2.8: Relative free energies in kJ mol^{-1} of the catalytic cycle at 298K using various functionals. The first and second oxidations are shown relative to the reduction $Ce^{4+}(aq) + e^- \longrightarrow Ce^{3+}(aq)$. The third step is the association of a water molecule, and is relative to an isolated water molecule.

	BP86	B3LYP	ω-B97X-D
O	0·0	0·0	0·0
A1	−10·7	70·4	175·6
A	17·7	92·6	129·3
B	12·9	75·3	115·8

The calculated energetics of the catalytic cycle are shown in Table 2.8, and are within the feasible limits of the catalysis which uses Ce^{4+} as an oxidant, although, as is common with transition metal systems, there is considerable dependence upon functional, varying

Figure 2.5: Relative free energies of the catalytic cycle at 298K using the BP86 functional. Oxidation states marked in the diagrams are those of the proposed reaction cycle. The first and second oxidations are shown relative to the reduction $Ce^{4+}(aq) + e^- \longrightarrow Ce^{3+}(aq)$. The third step is the association of a water molecule, and is relative to an isolated water molecule.

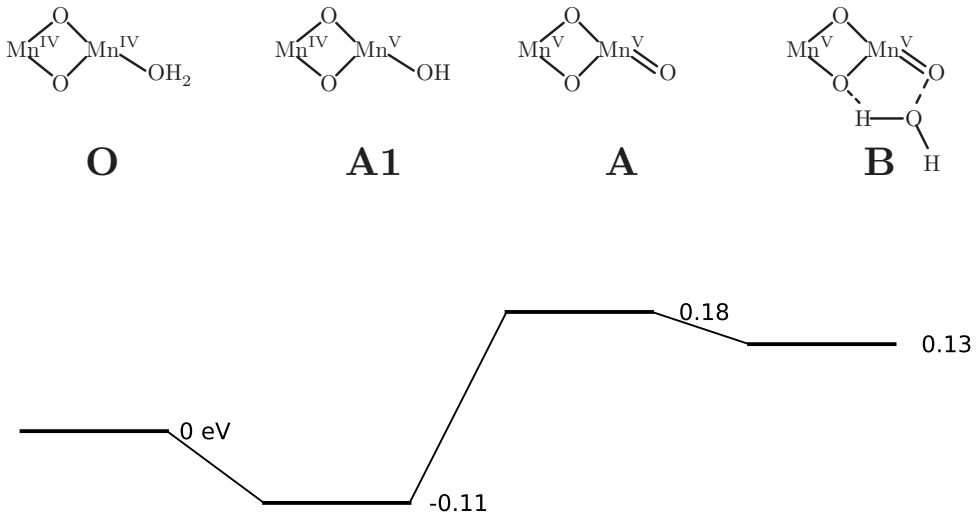

with amount of exact exchange included; the **A1** intermediate was found to be 0.73 and 1.82 eV higher than **O** for B3LYP and ωB97X-D functionals respectively.

LOBA calculations showed that the electronic structure changes throughout the cycle were not simply explainable by metal oxidations. The spectrum of functionals chosen produced very similar analyses, and so we concentrate on the results of the B3LYP functional here with systems being high spin. Low-spin calculations gave similar results, with spins in the appropriate opposite space, although with a slightly more delocalization.

Figure 2.6 shows LOBA plots of compounds **O**, **A1**, and **A**. There is much information contained within the plots, but we shall explain the key features of the oxidation; the detailed analysis of further bonding effects is beyond the scope of this paper. Owing to the heavy polarization from the positive charge on the Mn, we shall refer to all ligand-metal orbitals as 'donating', rather than distinguishing covalent orbitals. The nature of the localized orbitals on nitrogen and acetate ligands does not change significantly, and so they have been not been plotted. The analysis is displayed as chemical structure diagrams in Figure 2.7.

In **O**, each Mn has three localized α electrons, which on inspection very much resemble d-orbitals, and so each Mn is nominally Mn^{IV}. Cl may be considered Cl^- with a lone-pair

Figure 2.6: LOBA plots for the $ClMnO_2MnO$ core of complexes calculated with unrestricted B3LYP in a 6-31G* basis using Löwdin/Edmiston-Ruedenberg analysis. O2 and O1 are bridging oxygens. Mn2 has the Cl ligand and Mn1 the initial water ligand, whose oxygen is labeled O3. The parenthetical number following each atom is the number of non-core fully-localized electrons in that spin space which are not shown on the plots. Each symbol corresponds to a different localized orbital, plotting its population on each atom when larger than 0.1 electrons. Orbitals with substantial contributions on atoms not shown are omitted. In H_2O and OH they correspond to normal OH bonds, and the remainder are mostly localized on the other ligands.

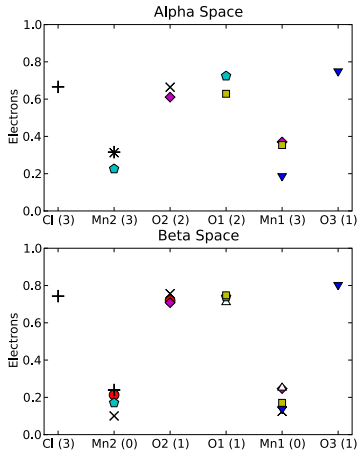

(a) **O** $S_z = \frac{6}{2}$. The Mn_2O_2 core consists of each oxo donating to each Mn, with further donation in the β-space. σ-bonds from O3 to its two hydrogen atoms have been removed from the plot. O3 donates a single lone pair to Mn1.

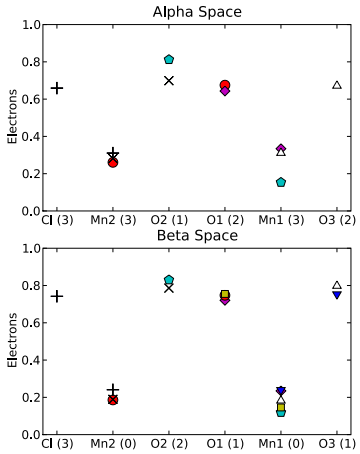

(b) **A1** $S_z = \frac{5}{2}$. With H^+ removed from it, O3 donates an additional β electron to Mn1. An α electron has been removed from O2.

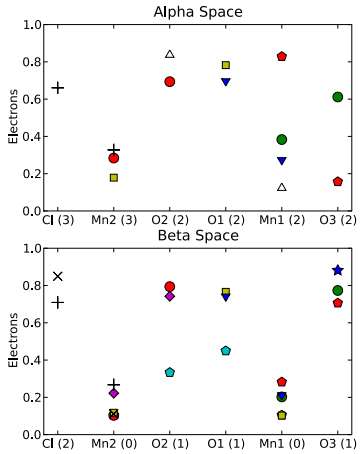

(c) **A** $S_z = \frac{6}{2}$. With a further H^+ removed from it, O3 now has only 3 α electrons, one of which is heavily donating to Mn1. The second oxidized electron has been removed from the β space of O2 and O1, resulting in a delocalized β-electron bridging both.

Figure 2.7: An interpretation of the LOBA as chemical structure diagrams. Full lines or arrow indicate a pair of electrons, dotted indicate single α electrons, and dashed indicate β electrons. Atoms are labeled with charge or oxidation state derived from the LOBA. Lines indicate covalent bonds and arrows indicate dative bonds (where the electrons are still considered localized on the donor). Unpaired localized electrons are indicated by $\cdot$ with the spin superscript. The remaining localized electrons electrons on the Mn atoms are α-spin.

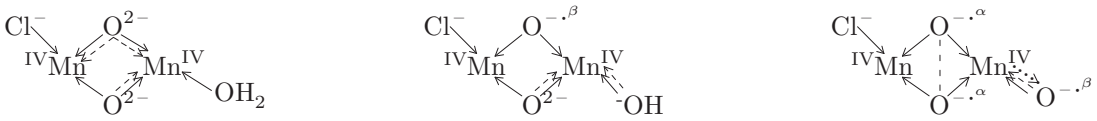

Figure 2.8: Isosurface (0.07 a.u.) plots of some of the localized ER orbitals shown in Figure 2.6. (a) In **O**: A localized Mn α d orbital. Each Mn has three of these; (b) In **O**: An O-Mn α σ bond. There is one of these between each Mn and bridging O; (c) In **A**: The Mn-O α donor orbital with π character; (d) In **A**: The Mn_2O_2 delocalized β orbital.

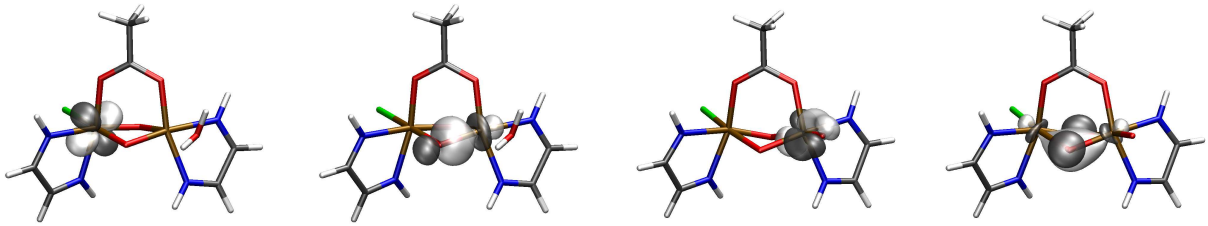

(a) (b) (c) (d)

heavily donating to Mn2. Similarly each oxo donates a lone pair to each Mn. The terminal O from H_2O has donated a lone pair to Mn1.

In **A1**, H^+ and an α electron have been removed. The terminal O3 donates a further β electron to Mn1. The oxidized electron is a localized α electron removed from O2. The α HOMO of **O** is delocalized around Mn2 (14%), O1 (23%) and O2 (28%), and so a first guess that this is ionized might fortuitously arrive at a similar conclusion, although the effects of geometry relation and the removal of an additional proton are likely to be at least as significant.

In **A**, a further H^+ and a β electron has been removed. Cl is now donating an additional β electron to Mn2. O3 now has only 3 α electrons, one of which is donating very strongly to Mn1. The β space of the bridging O2 and O1 now contains only one electron each, with a further β electron delocalized between the two. The β HOMO of **A1** is mostly localized on the Cl (82%), and so would not have predicted these electronic effects. Plots of some of

the relevant localized orbitals are shown in Figure 2.8.

Overall, the nature of the oxidation sites in **A1** and **A** is quite different. However, it is notable that the oxidation does not occur on the Mn atoms as proposed, but rather on the bridging oxygens and terminal oxygen. In particular, this is not a disability of the electronic structure method to describe the high oxidation states of Mn, as they have been seen to be well described earlier.

2.5 Conclusion

In contrast to Mulliken and Löwdin population analyses, and Mayer bond orders, the bonding and oxidation states produced by LOBA are very compatible with chemical intuition, and are relatively insensitive to the population analysis and localization method used. Comparison of NBO analysis and LOBA gives similar results in most cases, although LOBA does not seem to produce the undesirable symmetry breaking seen in some transition metal complexes with NBO analysis. We suggest that, though it is only currently possible for single-determinant theories, LOBA is to be preferred because of its simplicity. We also note that despite the fact that there is no quantum mechanical operator for oxidation state LOBA naturally produces the quantity chemists have been using for over a century to characterize transition metal chemistry.

A study of a manganese-based potential water oxidation catalyst showed a complex electronic structure, but revealed a non-intuitive oxidation of the bridging oxo ligands in preference to a metal oxidation as was proposed.

Chapter 3

Hydrogen Generation from Water by a Molecular Molybdenum-Oxo Electrocatalyst

3.1 Introduction

Due to growing concerns on the impact of anthropogenic climate change, the search for carbon-neutral sources of renewable energy has become a prominent area of scientific research [117]. Solar energy capture in conjunction with a chemical energy storage system has been proposed as one potentially feasible solution to the global energy crisis [129]. One proposed strategy for chemical storage is the use of hydrogen as a fuel, because of its benign combustion by-products, large energy density by mass (143 MJ/kg), and the potential to use H_2O to produce the fuel [130].

In order for hydrogen to be useful as a fuel or energy storage technology, it must be produced sustainably and economically using earth-abundant, inexpensive catalysts. While naturally occurring hydrogenase enzymes containing iron and nickel cofactors are capable of significant turnover frequencies and low thermodynamic potentials, [131–135] these enzymes suffer from instabilities under industrial conditions which inhibit their deployment in a commercial setting. On the other hand, heterogeneous precious metal catalysts such as Pt exhibit high activity at low overpotentials (applied potential beyond the thermodynamic potential of the reaction) in acidic or basic media, but their high costs prohibit large scale deployment of these systems. Consequently, significant research has been carried out on catalysts containing earth abundant elements for the production of hydrogen. However, many of the resulting molecular H_2-evolving catalysts to date require organic solvents and additives or organic acids to reach high levels of performance [136–142]. For a comprehensive comparison of some of the latest hydrogen evolving catalysts, see the review by Cook et al.[130].

An exciting potential candidate for a hydrogen-evolving catalyst is the molybdenum-oxo

Figure 3.1: $[(PY5Me_2)MoO]^{2+}$. Shown schematically (a) and its 3D computed structure (b).

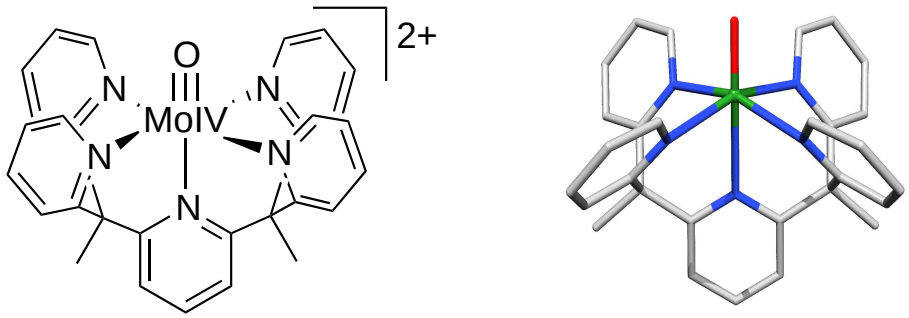

(a) (b)

complex recently reported by Karunadasa et al.[143]. Specifically the system consists of the pentadentate ligand-framework 2,6-bis(1,1-bis(2-pyridyl)ethyl)pyridine ($PY5Me_2$) supporting a molybdenum-oxo species (Figure 3.1). This complex shows high catalytic activity, a turn-over-frequency of at least 2.4 s^{-1}, and stability in pH 7 aqueous media and sea water. Since the catalyst is of molecular origin, the substantial tools of synthetic organic chemistry may be leveraged to improve upon its performance. Perhaps the most important target would be lowering the overpotential required for catalysis, which was reported as approximately -0.5 V. Experimental steps have already been taken in this direction. In particular, Sun et al.[144] showed that para-substitution of the axial pyridine ring of $[(PY5Me_2)Co]^{1+}$ lowered the catalytic potential significantly in water.

To provide both fundamental understanding and a rational basis for synthetic modifications of $PY5Me_2$-based catalysts, it is desirable to understand the mechanism of catalysis in molecular detail and characterize the electronic structure of all intermediate species. The purpose of this paper is to present computational and experimental studies directed at this goal. In the original report, a Hg electrode was used as the working electrode due to its high overpotential for proton reduction. However, a recent report showed that the reduced Mo species forms an adsorbate on the Hg surface, thereby complicating further characterization of the active species. It was also reported that the $[(PY5Me_2)MoO]^{2+}$ can catalyze the reduction of acetic acid to hydrogen in an acetonitrile solution on a glassy carbon disk electrode where the active catalyst was freely diffusing in solution.[145] Cyclic voltammetry experiments further showed that a third electron is necessary for proton reduction both in water and organic media on a glassy carbon electrode. In light of these considerations, the set of intermediates shown in Figure 3.2 constitute a potentially complete description of the viable intermediates associated with catalysis, and will be explored herein.

Within the last twenty years, electronic structure calculations have proven useful in assisting interpretation of experimental results, eliminating high energy reaction pathways, and providing insight for rational design of synthetic changes in chemical systems. Typically,

Figure 3.2: Cartoons of the species potentially involved in the electrocatalytic cycle of $[(PY5Me_2)MoO]^{2+}$ and their reactions. The $PY5Me_2$ ligand is represented by a circle for clarity. The double dagger symbol, ‡, indicates the species are coupled through a transition structure. Metal oxidation states are those given by electron counting. The bold letters labeling species will be used as their designation in the text.

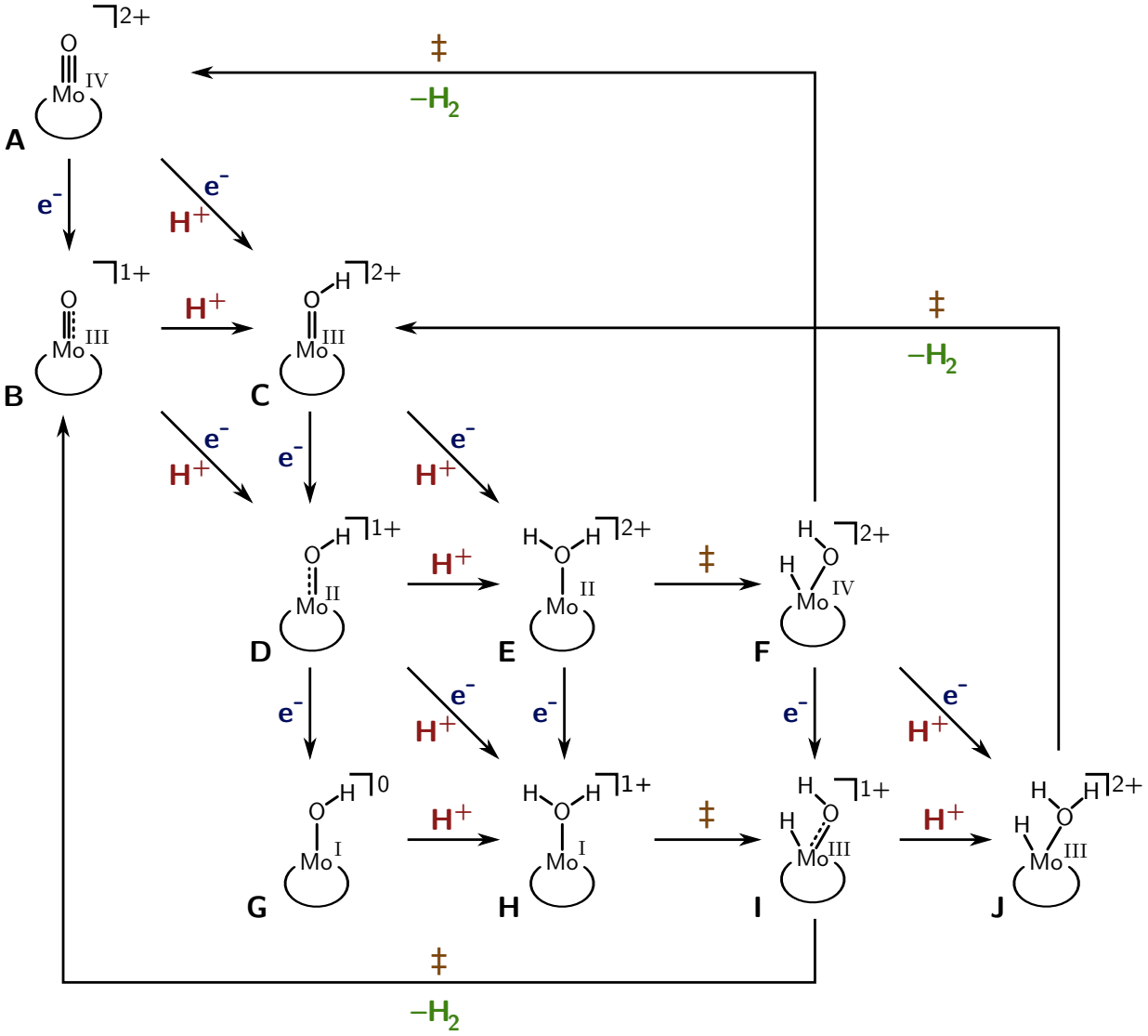

Density Functional Theory (DFT)[25, 26, 103] has been the tool of choice for the computation of redox potentials[146, 147] and the modeling of catalytic processes[148]. With modern functionals, sufficient accuracy is obtained to yield useful insight into catalytic cycles without requiring prohibitive computational effort. However, electronic structure calculations, even if satisfactorily accurate, are essentially just numerical experiments, requiring other methods for analysis and chemical insight. For instance, Localized Orbital Bonding Analysis (LOBA) [149] is useful for the computational description of oxidation states and understanding the extent of electron or hole localization associated with redox changes.

Very recently, the catalytic cycle originating with $[(PY5Me_2)MoO]^{2+}$ was studied using DFT calculations by Li and Yoshizawa[150], who showed the energetic validity of H_2 generation by reductive cleavage of water and α-H abstraction and identified a role for three reductions. The computational and experimental work reported here will validate these basic conclusions. However some important distinctions will also emerge. First, combining our calculations with new experiments reported here, we will conclude that the nature of the reductive steps is quite different from those reported by Li and Yoshizawa[150]. We find that the first two reductions are proton-coupled, rather than involving multiple intermediates and the mechanism of the third reduction also differs. Second, we have found a new mechanism for the α-H abstraction step that involves a bridging water acting as a proton relay. Third, the calculated kinetics we obtain are in more satisfactory agreement with experimental values. Additionally we extend the study of the mechanism in several distinct ways. We examine computationally in some detail the manner in which electrons are added to the complex in the three reductions. Then, based on this knowledge, we perform computational experiments on the effect of chemical modifications to the $PY5Me_2$ ligand platform to explore the effect on the predicted overpotential. Finally, we also explore the stoichiometric reaction of reacting $[(PY5Me_2)Mo]^{2+}$ with H_2O to produce $[(PY5Me_2)MoO]^{2+}$ and H_2 and its possible use as an electrocatalytic pathway.

The rest of this article is laid out as follows: we will begin by describing the computational tools used to study this system. Next, we will discuss the reductive steps of the catalytic cycle, followed by the kinetics associated with the steps occurring after the final reduction, which will include our new mechanism for H_2 formation. We will then briefly describe the stoichiometric reaction, $[(PY5Me_2)Mo]^{2+}+H_2O \longrightarrow [(PY5Me_2)MoO]^{2+}+H_2$, and its possible use as an electrocatalytic reaction. Finally we will finish by describing substituent effects and how they may be used to reduce the overpotential of the catalyst.

3.2 Computational Detail

Choice of Density Functional

Three different functionals with differing treatments of exchange were explored: B3LYP[40], BP86[33, 104], and ωB97[43]. The results necessarily depend on the choice of functional, and since different approximate functionals perform with different levels of accuracy on different

problems, an appropriate choice for the systems at hand is important. The energetic results found with the BP86 functional most closely correspond to the experimental reduction potentials; indeed the B3LYP and ωB97 functionals give the wrong sign for the first reduction. Throughout the rest of this study, we present BP86 results unless otherwise specified. The relative energies obtained with all functionals are given as part of the Appendix A in Table A.2. The choice of BP86 has many precedents: it has already been widely used in many successful studies of transition metal containing systems[151–158], including those where hydrogen binding and release is involved[159–161].

Quadrature Grids and Basis Sets

Exchange-correlation functionals were calculated with a larger than standard numerical quadrature grid with 70 radial points and 302 Lebedev angular points, in the interest of keeping energy, gradient, and Hessian calculations numerically consistent. Three basis sets were used in the calculations. First, a medium-sized basis including the SRSC effective core potential[162] for the Mo and cc-pVDZ[163] for all other atoms was used for the initial transition structure searches. Second, a medium-sized basis set consisting of the all electron SV + polarization of Ahlrichs et al.[164] on Mo and 6-31G*[165] for all other atoms (denoted SV-P/6-31G*) was used with the B3LYP functional for optimizations and frequencies. Third, a larger basis denoted as TZV-P/6-311G** was used for single point energy calculations. It consists of the all electron TZVP basis[164] with the original f function split into two f's and a g with contraction coefficients of 0.533380331, 1.60014099, 1.04835114 respectively on Mo and 6-311++G** functions on H and N, and 6-311G** functions on C and O.

Software and Algorithms

All calculations were performed in a customized version of the Q-Chem package[98], using unrestricted orbitals. Guess densities for all calculations were produced by superposition of converged fragments of the ligand and molybdenum-oxo core[166]. Unrestricted SCF calculations were performed using the Relaxed Constraints Algorithm (RCA)[100, 101], until a threshold of 10^{-3} or 10^{-5} Hartrees as necessary, followed by Geometric Direct Minimization[102] to a convergence of 10^{-9} Hartrees; for certain cases where convergence was difficult to reach RCA alone was used to reach the 10^{-9} Hartrees target. After stationary points of the wavefunction were found, a stability analysis [106] was performed on all solutions to determine its nature; if a saddle point was found, a downhill step was taken and then reminimized. Frequency calculations within the harmonic approximation were used to compute gas phase free energies G(298.15 K). Since the lowest energy spin state for transition metal species is not obvious, at least two spin states for each species were calculated, the respective geometries were minimized, and the lowest energy spin state was then selected. Table A.2 contains the absolute energies of all calculated spin states.

Localized Orbital Bonding Analysis (LOBA)

LOBA[149] is employed for analyzing the oxidation state of the Mo through-out the catalytic cycle, and to assess the extent to which Mo electrons are delocalized. It is a combination of two parts: first a localization of molecular orbitals and then a subsequent orbital-by-orbital population analysis to determine metal oxidation states. The population value provides a measure of the density at a metal center for each electron and thus allows one to count the number of electrons at that center and calculate the oxidation state. The Pipek-Mezey algorithm[96] was utilized for the localization procedure. LOBA was performed using Löwdin population analyses[80, 81]. All oxidation states were calculated using LOBA at the BP86/TZV-P/6-311G** level of theory.

Optimizations and solvation

As a starting point, the solid state structure of the di-cation ($[(PY5Me_2)MoO]^{2+}$) obtained from single crystal x-ray diffraction studies was optimized so as to relax to its gas-phase geometry. This relaxation was performed so the species for which crystal structures are unavailable may be be compared consistently. The subsequent species in the cycle were created by addition of hydrogen atoms and electrons followed by relaxation to their individual gas-phase geometries. All transition structures were confirmed following the intrinsic reaction coordinates to products and reactants. While solvation is entirely neglected in the optimizations, it is manifestly critical in assessing the relative energies of intermediates that have different charges, and may also be important for the relative energies of intermediates with the same charge. However, for a hydrogen bonding solvent like water, there are well-known limitations and ambiguities with even the most useful of polarizable continuum solvation (PCM) models[167–169]. These models disregard specific solvent-solute interactions, such as hydrogen bonds, which in our context amounts to disregarding the interactions between waters and the molybdenum-oxo or hydroxy species, which are potentially significant. Therefore, as will become clear in Results and Discussion, we instead use experimental information to infer the change in solvation energy for species with different charges. To briefly introduce the approach taken in this study: the experimental evidence indicates the protonated species **C** exists in solution; therefore it must have a lower free energy than that of the unprotonated species **B**. However because of the reduction in charge, in the gas phase the energy of **B** is lower than that of **C**, and this difference needs to be made up by solvation and thus sets a lower bound on the differential solvation energies. We neglect any possible change in solvation energy for species with the same charge (including transition structures), which is partly justified by the fact that different intermediate species in the catalytic cycle have roughly the same cavity size and thus solvent reorganization energies are likely to be small.

Figure 3.3: The thermodynamic cycle of the first reaction used to relate calculations to experimental $E_{1/2}$ values. $\Delta G_{(sol)}$ is the free energy of solvation. The letter L is used in place of $PY5Me_2$ for simplicity. Other reactions follow a similar pattern with $[(LMoO)]^{2+}$ and $[(LMo)OH]^{+}$ replaced by the pertinent species and the appropriate number of protons and electrons for the reaction.

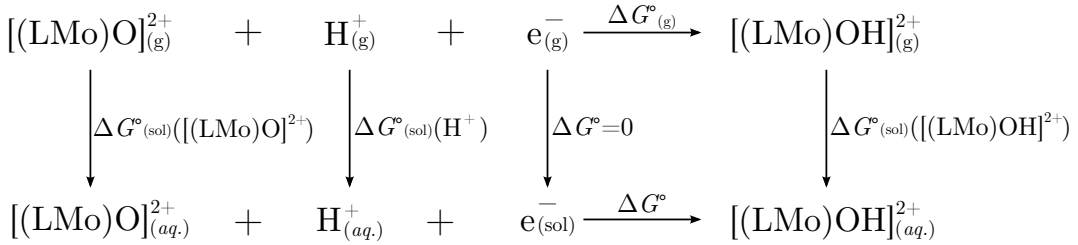

Electrochemical Aspects

In order to compare the results of gas phase electronic structure calculations to solution phase electrochemical measurements, thermodynamic cycles of the form shown in Figure 3.3 were modeled[170]. The gas phase calculations, including frequency calculations to account for the thermal and entropic contributions, allow for the computation of the upper portion of the cycle. The free energy for the reaction is given by Equation 3.1.

$$\begin{aligned}\Delta G^{\circ} = {} & G_{(g)}([(\mathrm{LMo})\mathrm{OH}]^{2+}) + \Delta G^{\circ}_{(sol)}([(\mathrm{LMo})\mathrm{OH}]^{2+}) \\ & - \left[G_{(g)}([(\mathrm{LMo})\mathrm{O}]^{2+}) + \Delta G^{\circ}_{(sol)}([(\mathrm{LMo})\mathrm{O}]^{2+}) + \Delta G_{(sol)}(\mathrm{H}^{+})\right]\end{aligned} \tag{3.1}$$

To relate the values calculated to experimental values obtained by cyclic voltammetry, the reaction free energy must be shifted relative to the absolute potential of the standard electrode used in the given experiment, which is the Standard Hydrogen Electrode (SHE). There have been many values published for the absolute potential of the SHE (98.7 to 102.4 kcal/mol)[171–174]. We have chosen the value of Isse and Gennaro 98.72 kcal/mol[174], because this value was computed using the reference state for the electron (0 level for the electron energy in a vacuum at 0 K), which relates most directly to computational chemistry calculations. Another piece necessary to compute the free energy of this reaction is a sufficiently accurate reference value for the solvation free energy of the proton ($\Delta G_{(sol)}(\mathrm{H}^{+})$). A number of values [173–177] were considered, all of which lay in the range of -266.7 to -263.12 kcal/mol and the value of -263.12 kcal/mol reported by Isse and Gennaro's [174] was chosen for consistency with the value chosen for the shift with respect to SHE. Finally, a correction to relate the standard state concentrations (1 M) to the experimental concentration of H^{+}

(10^{-7}M) must be added (see Equation 3.2 where Q is the reaction quotient)

$$\Delta G^{\circ\prime}_{(\mathrm{T=298.15K})} = \Delta G^{\circ} + RT\ln\left(\frac{Q^{\circ\prime}}{Q^{\circ}}\right) \tag{3.2}$$

$$= \Delta G^{\circ} + RT\ln\left(\frac{\frac{1\ \mathrm{M}\ [(\mathrm{LMo})\mathrm{OH}]^{2+}}{1\ \mathrm{M}\ [(\mathrm{LMo})\mathrm{O}]^{2+}\cdot 10^{-7}\ \mathrm{M}\ \mathrm{H}^{+}}}{\frac{1\ \mathrm{M}\ [(\mathrm{LMo})\mathrm{OH}]^{2+}}{1\ \mathrm{M}\ [(\mathrm{LMo})\mathrm{O}]^{2+}\cdot 1\ \mathrm{M}\ \mathrm{H}^{+}}}\right) = \Delta G^{\circ} + 9.55\ \mathrm{kcal/mol} \tag{3.3}$$

Recently, Solis and Hammes-Schiffer[178] have employed isodesmic reactions to compute reduction potentials and pK_as of Cobaloximes participating in hydrogen evolution reactions. This approach is quite powerful since it accounts for the systematic computational error in DFT due to approximate functionals and basis set incompleteness. However, in order to be exploited fully, it is beneficial to have reference reduction potentials for reactions which are of a similar nature (i.e. oxidation state and ligand species) to those being studied. Reference reactions similar to the ones studied in this paper are difficult to obtain due to the rarity of high Molybdenum oxidation states and recent development of the ligand. Therefore, isodesmic reactions were not utilized in this study.

3.3 Results and Discussion

Reductions

In order to be able to realistically model the catalytic cycle of $[(\mathrm{PY5Me_2})\mathrm{MoO}]^{2+}$ we first need to prove we are able to obtain accurate geometric structures for these species. The geometry of the resting state, **A** in Figure 3.2, was reproduced to serve as a benchmark for the geometry optimization of the subsequent species in the catalytic cycle. Table 3.1 shows that the calculated structure is in reasonable agreement with the crystal structure; for an image of the crystal structures see the Figure A.1 and for images of the calculated structures see Figure A.3. The same level of theory was then used to compute the geometries for the rest of the species in Figure 3.2.

The first fork in the reaction pathway occurs at $\mathbf{A} \longrightarrow \mathbf{C}$ or $\mathbf{A} \longrightarrow \mathbf{B}$ in Figure 3.2. Because the electronic structure calculation favors the reduction of net positive charge, the gas phase energy of **B** is much lower than that of **C**. Therefore, in order to distinguish between these two pathways, the pH dependence of the first reduction of $[(\mathrm{PY5Me_2})\mathrm{MoO}]^{2+}$ over a pH range of 4.1 to 7.7 was studied at a glassy carbon electrode using cyclic voltammetry, as shown in Figure 3.4. The plot of the peak potential, E_{p}, of the first reduction versus pH shows a linear fit with a slope of 44 mV. If this was a reversible single proton-coupled-to-electron event, we would expect a slope of 59 mV; however, the deviation in our value may be a result of the irreversibility of the first redox event. Thus, the experimental evidence indicates that the first reduction involves a protonation, favoring **C** as the chemically relevant species. In order to make the experimental and theoretical results consistent, it is necessary to consider the solvation energy of the **B** and **C** species, because the more

Table 3.1: Averaged values for parameters from two $[(PY5Me_2)MoO]^{2+}$ molecules in the unit cell of $[(PY5Me_2)MoO](CF_3SO_3)_2$, standard deviations in parentheses, compared to the calculated geometry of the resting state **A**.

	Bond Lengths (Å)			Angles (°)		
	Mo-O	Mo-N_{ax}	Mo-N_{eq}(avg)	N_{ax}-Mo-O	N_{ax}-Mo-N_{eq}(avg)	Mo-N_{ax}-C_{ax}
Experiment	1.685(3)	2.315(3)	2.159(1)	175.9(1)	81.1(4)	178.5
Calculated	1.662	2.385	2.205	179.8	80.5	179.2
Abs. Error	0.02	0.09	0.05	4.0	0.6	0.7
% Error	1.4	3.0	2.2	2.2	0.8	0.4

Figure 3.4: (a) Cyclic voltammogram of $[(PY5Me_2)MoO]^{2+}$ (**A**) in 1.0 M buffered aqueous solutions at pH 7.7 (red), 6.9 (green), 6.3 (magenta), 4.9 (blue), and 4.1 (black) on a glassy carbon disk electrode. (b) Plot of the first and second reduction potential versus pH. Blue squares are the peak potentials of the first reduction, E_p, with a linear least squares fitted slope of 44 mV in black and red circles are the $E_{1/2}$ of the second reduction with a linear least squares fitted slope of 66 mV. Both these slopes are comparable to 59 mV, which is indicative of a proton-coupled electron transfer event. For the experimental details see the Appendix A

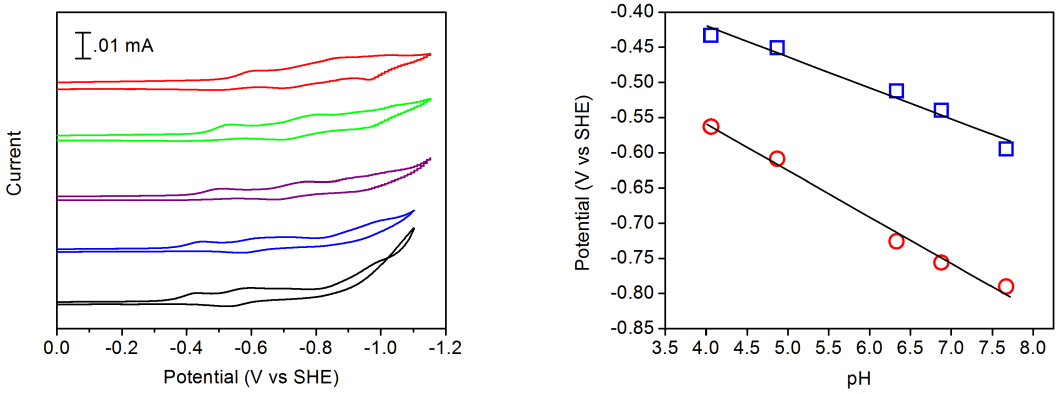

(a) (b)

highly charged species, **C**, will be favored in aqueous media. Using the experimental result ($G_{aq.}(\mathbf{C}) < G_{aq.}(\mathbf{B})$) as a guide, we find a lower bound on the solvation free energy difference, $(\Delta G^{\circ}_{(sol)}(\mathbf{C}) - \Delta G^{\circ}_{(sol)}(\mathbf{B}))$, of 3.7 eV. The computed reduction potential of $\mathbf{A} \longrightarrow \mathbf{C}$ is 0.48 V, which compared to experiment, $E_p = 0.55$ V, is quite satisfactory.

Now that the calculated result is consistent with the experiment, the electronic structure of species **B** and **C** may be examined in more detail. By comparing the LOBA result of **B**

to that of **A** (Figure A.2), we are able to say that the additional electron has been added to an orbital of antibonding character, which reduces the bond order of the Mo−O bond (based on the LOBA analysis, it changes from 3 to 2.5). This weakening of the bond makes the oxo ligand more nucleophilic which in turn increases its pK_a, explaining why **C** is the more thermodynamically stable species. The electronic structure of species **C** is what one would expect for a molybdenum-hydroxy species with a LOBA calculated oxidation state of 3+.

For a second reduction starting from **C**, the possible pathways are either direct reduction, $\mathbf{C} \longrightarrow \mathbf{D}$, or a proton-coupled reduction, $\mathbf{C} \longrightarrow \mathbf{E}$. CV experiments were again employed with computation to distinguish between these pathways. Experimentally, the second reduction process is quasi-reversible with a well-defined $E_{1/2}$. When the $E_{1/2}$ is plotted against pH, a linear fit with a slope of 66 mV was obtained, suggesting a second one-proton, one-electron coupled process (Figure 3.4). The same logic concerning solvation effects may be applied, resulting in a lower bound on the solvation energy difference favoring **E** over **D** by 4.0 eV. This becomes our sharpened estimate of the differential solvation of the 2+ and 1+ species, and this value was added to the free energies of **B**, **D**, **H** and **I** to define the relative energetics. The computed reduction potential of this step is then 0.47 V which is ∼0.3 V under the experimental $E_{1/2}$ of 0.76 V. This larger difference may be due to our assumption that the solvation free energy of **A** and **C** are exactly the same. Another source of computational error comes from the intrinsic errors associated with the density functional[146]. In addition, these errors may be due to omission of the electrode surface in the modeling.

The next step of the cycle involves either hydride migration, $\mathbf{E} \overset{\ddagger}{\rightarrow} \mathbf{F}$, or the third reduction, $\mathbf{E} \longrightarrow \mathbf{H}$. When the free energies of these species are compared, including the solvation correction discussed above, the energy of **H** is almost equal that of **F**, but the pathway to **F** is impeded by slow kinetics, which will be discussed later. Furthermore, it is experimentally known that the electrocatalysis contains three reductions and thus even if $\mathbf{E} \overset{\ddagger}{\rightarrow} \mathbf{F}$ were to occur it would be further reduced to **I**, where it will rejoin the other pathway. The computed potential for the reduction of $\mathbf{E} \longrightarrow \mathbf{H}$ is 0.77 V; this is to be compared to the experimental onset potential of the catalytic wave ∼1.1 V vs. SHE at a glassy carbon electrode. Our potential is under this experimental value by ∼ 0.3 V, similar to the deviation for the second reduction, for the same possible reasons listed above. The minimum potential required for $[(PY5Me_2)MoO]^{2+}$ to be employed electrocatalytically is the same as is required to produce species **H** and thus this potential should be most directly related to the overpotential for the catalyst.

Based on the LOBA analysis, the electronic character of **H** differs from **E** by much more than the addition of an extra electron to Mo. The localized orbitals that are primarily on molybdenum have much lower populations for species **H** than those found in **E** (Table A.3), indicating the molybdenum electrons in **H** are partially delocalized. This delocalization can also be seen visually in the localized molecular orbitals shown in Figure 3.5, where panel (a) for **E** is well-localized, while panel (b) for **H** exhibits clear delocalization onto the axial pyridine group. An electron-donating group may be able to stabilize these partially

Figure 3.5: Isosurface (0.07 a.u.) plots of a representative localized orbital of **E** and one of the orbitals of **H**, which by contrast shows substantial delocalization to the pyridine rings. This indicates functionalization of the pyridine rings may result in changes in the relative energetics and consequently the overpotential. The delocalization in **H** is in contrast to **I** where the only metal electrons that exhibit delocalization are now forming the Mo−H bond with a bond length of 1.7 Å.

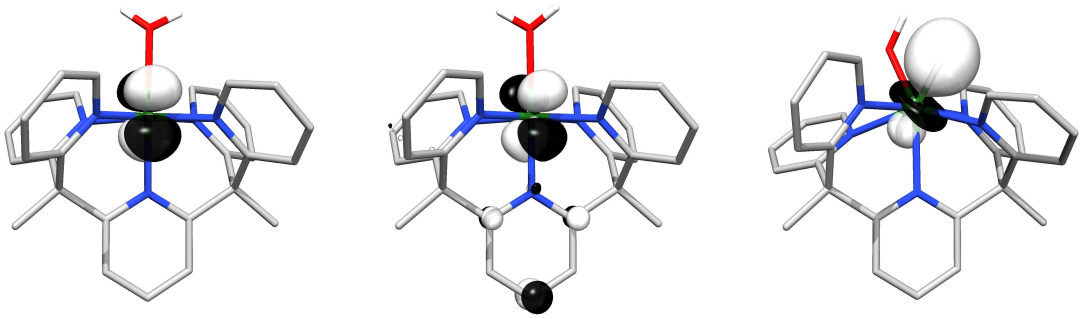

(a) **E** (b) **H** (c) **I**

delocalized orbitals, which is significant since the stability of **H** connects to the overpotential of the catalyst. We shall return to this topic in the subsection on Substituent Effects.

Following the formation of **H**, either intramolecular hydride transfer to **I** or proton addition to **J** could be the next intermediate in the cycle. We eliminate **J** as it is substantially higher in energy (0.5 eV) than **I** despite inclusion of the solvation correction. **I** is connected to **H** by a transition structure which is discussed in the next section, **Kinetics**; here, we shall focus on the electronic structure of the thermodynamically stable **I**. The LOBA calculated oxidation state of **I** is 3+ which agrees with standard electron counting. The d-orbitals on the molybdenum center no longer show the significant delocalization that they did in species **H**, apart from two electrons that yield the metal hydride bond as shown in panel (c) of Figure 3.5.

Kinetics

The chemical transformations associated with intramolecular hydride transfer, **H** $\longrightarrow$ **I**, and subsequent H_2 release are likely to have significant barriers, and therefore exert kinetic control on the overall turnover rate of the catalyst. We shall investigate the kinetics of proton reduction under the assumption that the electron transfer steps are not rate limiting.

Two transition structures for the evolution of hydrogen by $[(PY5Me_2)MoO]^{2+}$ were found; one for the transformation from **H** to **I** and the second from **I** to the release of hydrogen gas shown in Figure 3.6 and energetically summarized in Figure 3.7. Using the standard

Figure 3.6: Geometries of transition states for (a) the transformation to a metal hydride and (b) the direct release of H_2. The bonds being broken are the dashed lines.

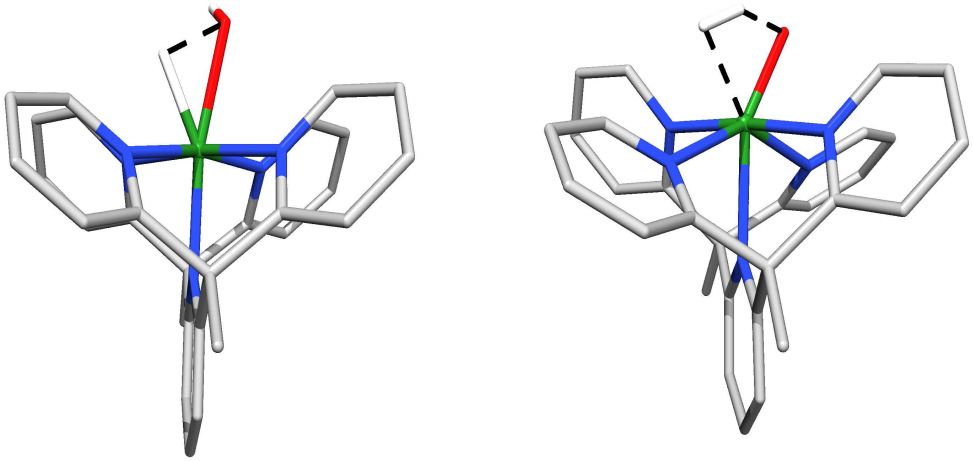

(a) $\mathbf{H} \xrightarrow{\ddagger} \mathbf{I}$ (b) $\mathbf{I} \xrightarrow{\ddagger} \mathbf{B}$

formulation of transition state theory (TST)[179, 180] (Equation 3.4), the rates in Table 3.2 were calculated. For the overall rate, a steady-state approximation ($d\mathbf{I}/dt = 0$) was made and the total rate was calculated using $\Delta G^{\ddagger} = G(\ \mathbf{H} \xrightarrow{\ddagger} \mathbf{I}\ ) - G(\mathbf{H})$. Some comparison against experimentally measured kinetics is possible though caution is necessary. We emphasize that the experimental rate is the lower limit for the catalytic rate[143] which was obtained under an applied overpotential. Nevertheless, to roughly assess the calculated barriers, the experimental rate of 2.4 $\mathrm{mol_{H_2}/mol_{catalyst}} \cdot \mathrm{s}$ has been back-converted to a $\Delta G^{\ddagger}$ using the inverse of Equation 3.4, resulting in a value of $\sim$ 17 kcal/mol; it should also be noted that because only one temperature measurement was taken, there are large uncertainties associated with this computed $\Delta G^{\ddagger}$.

$$k_{TST} = \frac{k_B T}{h} e^{\frac{-\Delta G^{\dagger}}{RT}} \tag{3.4}$$

As a hydrogen-bonding solvent, water can play an explicit role in stabilizing transition structures. We investigated this effect by including a water near **I** (Figure 3.9), but instead found a completely new transition structure for the release of hydrogen. The water molecule acts as a bridge between the two hydrogens of **I**, reducing the distance between the reacting hydrogens by 0.2 Å, which in the original computed structure were quite distant, 1.98 Å. In the transition structure the water acts a proton relay losing one of its hydrogens to form H_2 while simultaneously abstracting the hydrogen from the hydroxy species to regenerate

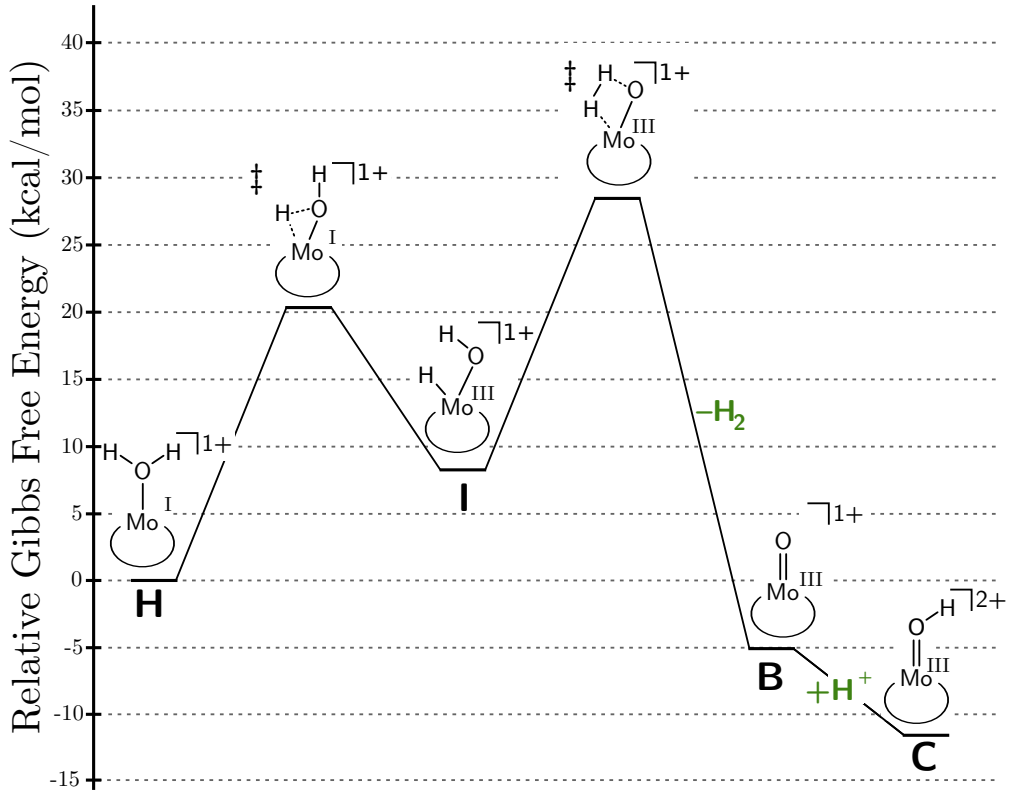

Figure 3.7: The Gibbs free energy diagram for the liberation of hydrogen from **H** and the reformation of **B**. The release of H_2 is exergonic by 5.0 kcal/mol and the total reaction by 11.5 kcal/mol. All species are treated with the solvation correction from the text, which is constant for all species with the same net charge.

Table 3.2: Rates from TST, using barriers calculated at the BP86/TZV-P/6-311G** level of theory using the assumptions described in the text, versus experimental values. [a] It should be noted that the experimental rate is for the overall reaction and this value is a lower limit because it was obtained under an applied overpotential.

	$\mathbf{H} \xrightarrow{\ddagger} \mathbf{I}$	$\mathbf{I} \xrightarrow{\ddagger} \mathbf{B} + H_2$	$\mathbf{I} + H_2O \xrightarrow{\ddagger} H_2$	Overall	Overall + H_2O	Experimental[a]
$\Delta G^{\ddagger}$ kcal/mol	20.3	20.1	16.9	28.4	25.1	16.9
$k_{TST}(s^{-1})$	8.22×10^{-3}	9.86×10^{-3}	2.62	9.21×10^{-9}	2.44×10^{-6}	2.4

Figure 3.8: The Gibbs free energy diagram for the liberation of hydrogen from **H** and the reformation of **B**. The release of H_2 is exergonic by 5.0 kcal/mol and the total reaction by 11.5 kcal/mol. All species are treated with the solvation correction from the text, which is constant for all species with the same net charge. Rather than spuriously attempt to take into account the complications involved in calculating the water association energies for a molecule already solvated in water, the complexation energy was set to zero.

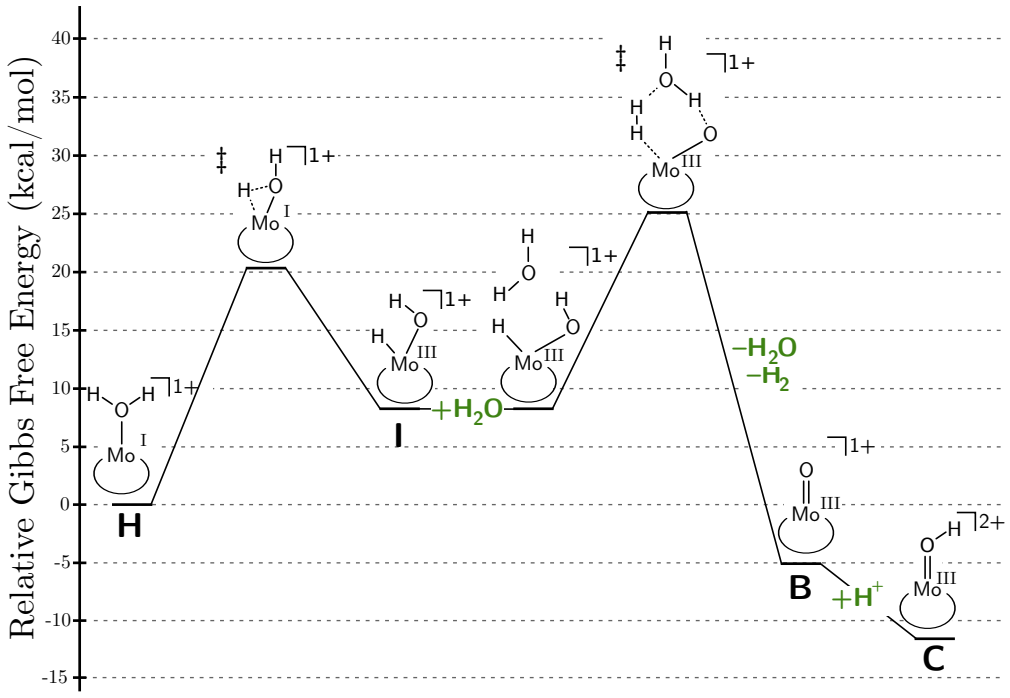

itself. The energetics for this new mechanism are shown in Figure 3.8 and the rate and barrier are shown in Table 3.2. The barrier for this new mechanism is ∼3 kcal/mol lower in energy and the rate is accordingly much higher (2.62 s^{-1}) for this step of the reaction. p This decrease in the reaction barrier indicates that it is important, if not essential, to consider explicit interactions between a solvent molecule and the reaction center, especially when the solvent may catalyze the reaction due to its molecular composition. Using this new transition structure to compute the overall rate (still assuming a steady-state of **I**) we obtain a a barrier of 25.1 kcal/mol. This barrier is only 8 kcal/mol larger than that of the calculated experimental one. This is likely to be within the errors associated with our calculations (approximate functionals, simple solvation treatment, and neglect of tunneling) and the error in determining the experimental barrier.

Figure 3.9: Geometries of the (a) **I** in the presence of a water molecule and (b) the transition state for the release of H_2 including the bridging water. The bonds being broken are the dashed lines.

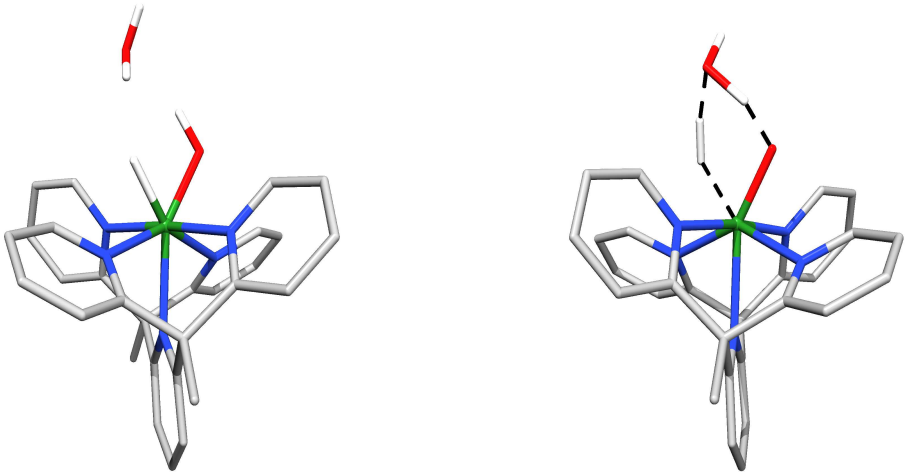

(a) $\mathbf{I} + H_2O \xrightarrow{\ddagger} \mathbf{I}$ (b) $\mathbf{I} + H_2O \xrightarrow{\ddagger} \mathbf{B} + H_2 + H_2O$

Stoichiometric Reaction

As previously reported, [143] the stoichiometric reaction between $[(PY5Me_2)Mo(CF_3SO_3)]^{1+}$ and water leads to the formation of $[(PY5Me_2)MoO]^{2+}$ and evolution of H_2. Hydrogen production was confirmed by mass spectrometry and the oxo was shown to originate from water by observing the isotopic shift in the infrared spectrum of the Mo=O bond upon reaction in $H_2^{18}O$. If the triflate is labile and exchanges with a water, the species initially formed is $[(PY5Me_2)Mo(OH_2)]^{2+}$, **E**, and the subsequent loss of H_2 may be analyzed using the same computational tools employed for the catalytic cycle above. The experimental lability of triflate was confirmed when a crystal structure obtained upon crystallization from a solution of $[(PY5Me_2)Mo(CF_3SO_3)]^{1+}$ in acetonitrile showed substitution by a solvent molecule, as shown in Figure A.1 of Appendix A.

Accordingly, we have found transition structures for the intramolecular hydride migration, $\mathbf{E} \rightarrow \mathbf{F}$, and for the subsequent evolution of H_2, yielding **A**. The structures are qualitatively similar to those discussed previously, as can be seen by comparing Figure 3.10 with Figure 3.6. The energetics of these reaction are shown in Figure 3.11. Using Equation 3.4 to calculate the rate of reaction for these transition structures leads to the rates shown in Table 3.3. Again, for the overall rate, a steady-state approximation ($d\mathbf{F}/dt = 0$) was made and the total rate was calculated using $\Delta G^{\ddagger} = G(\ \mathbf{F} \xrightarrow{\ddagger} \mathbf{A}\ ) - G(\mathbf{E})$. Note that a spin cross-over occurs in this reaction, since the transition structure $\mathbf{F} \xrightarrow{\ddagger} \mathbf{A} + H_2$ is a singlet

Figure 3.10: Geometries of transition structure involved in the stoichiometric reaction, $[(PY5Me_2)Mo(CF_3SO_3)]^{1+} \xrightarrow[-CF_3SO_3^-]{+H_2O} [(PY5Me_2)MoO]^{2+} + H_2$ (a) conversion to a metal hydride and (b) release of H_2.

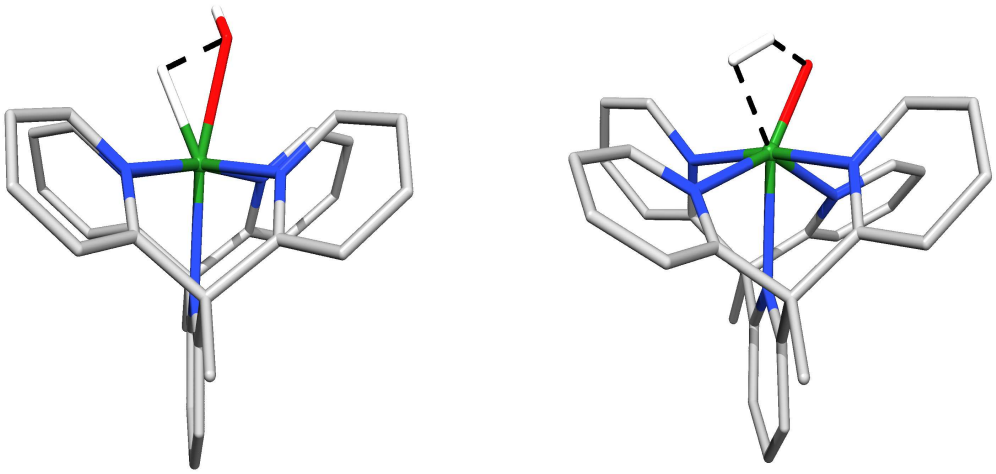

(a) $\mathbf{E} \overset{\ddagger}{\rightarrow} \mathbf{F}$ (b) $\mathbf{F} \overset{\ddagger}{\rightarrow} \mathbf{A}$

Table 3.3: Rates from TST for the stoichiometric reaction at the BP86/TZV-P/6-311G** level of theory.

	$\mathbf{E} \overset{\ddagger}{\rightarrow} \mathbf{F}$	$\mathbf{F} \overset{\ddagger}{\rightarrow} \mathbf{A} + H_2$	Overall
$\Delta G^{\ddagger}$ kcal/mol	25.5	18.2	36.0
$k_{TST}(s^{-1})$	1.4×10^{-6}	0.27	2.41×10^{-14}

whereas the **F** itself is a triplet. This spin crossover could also lower the overall rate of this reaction, though this need not be the case [181]. Finally, it is also possible that water-assisted transition structures exist, as was shown in the previous section.

Regardless, the calculated rates of $\mathbf{E} \overset{\ddagger}{\rightarrow} \mathbf{F} \overset{\ddagger}{\rightarrow} \mathbf{A} + H_2$ are very interesting when compared to the rates of $\mathbf{H} \overset{\ddagger}{\rightarrow} \mathbf{I} \overset{\ddagger}{\rightarrow} \mathbf{B} + H_2$, the species believed to participate in electrocatalysis. This comparison explains why the third electron is necessary for electrocatalysis, despite the reduction of hydrogen being a two electron process. The slowest rate of the +1 species is approximately 4 orders of magnitude larger than that of the +2 species (8.2×10^{-3} s^{-1} vs 1.4×10^{-6} s^{-1} respectively). Thus on the timescale of a CV experiment (> 20 s), the species **F** is unable to form in any significant amount and the system is only a functioning catalyst

Figure 3.11: The Gibbs free energy diagram for the liberation of hydrogen from **E**. The release of H_2 is exergonic by 4.9 kcal/mol. All species are treated with the solvation correction from the text, which is constant for all species with the same net charge.

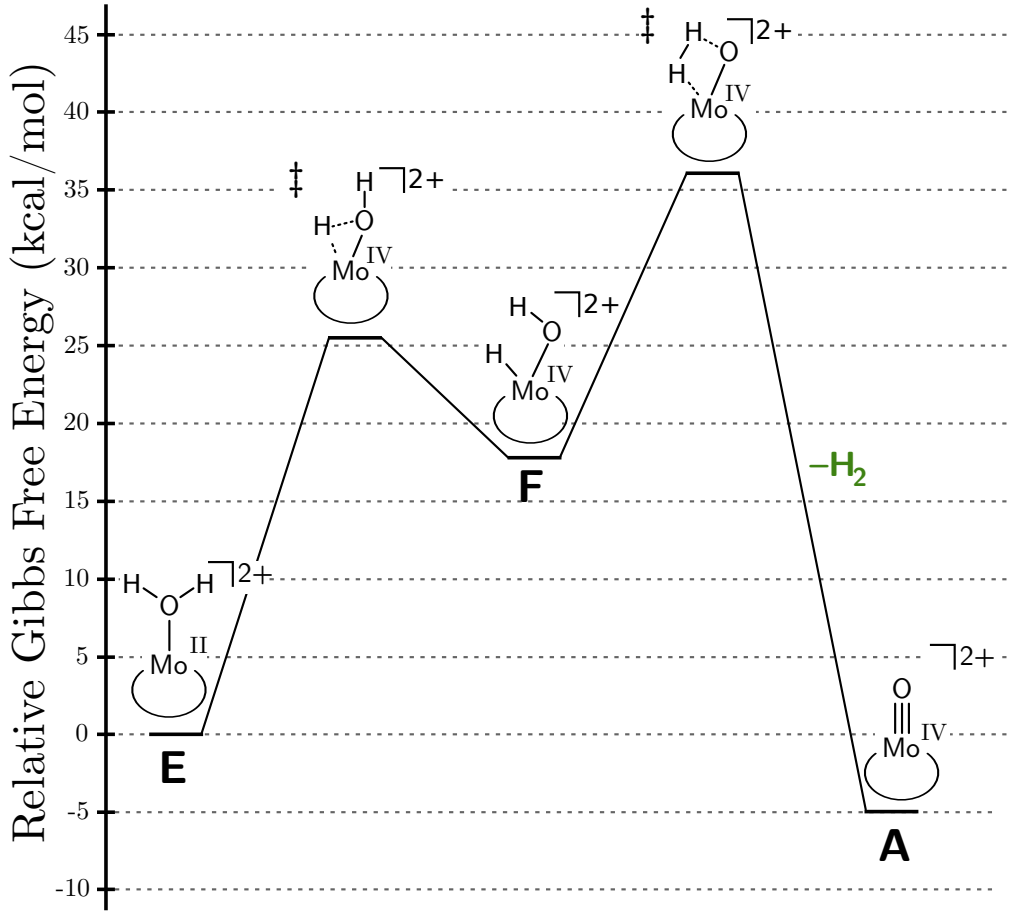

after a third reduction.

However, the stoichiometric reaction opens up an interesting possibility. If the rate of this reaction could be increased to be comparable to that of $\mathbf{H} \xrightarrow{\ddagger} \mathbf{B} + H_2$, it may be possible to bypass the third reduction which should significantly lower the overpotential of the catalyst. The proposed cycle for this reaction is shown in Figure 3.12. Of course such modifications may be synthetically challenging, or not be possible without undermining some of the positive properties of the existing catalyst. However, it certainly indicates the potential for further explorations of this catalyst architecture.

Figure 3.12: The proposed two electron cycle for $[(PY5Me_2)MoO]^{2+}$, which utilizes the same mechanism as the stoichiometric reaction.

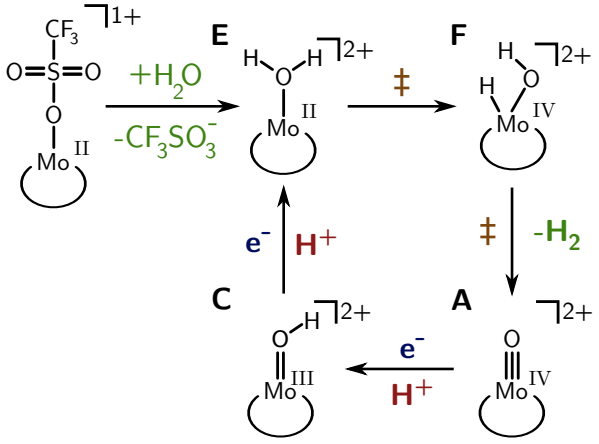

Substituent Effects

Let us briefly summarize the implications of the **Reductions** subsection for tuning the catalyst. The third reduction leads to intermediate **H**, and the relative energy of this species versus the prior intermediate, **E**, formally controls the overall potential bias needed for catalysis. Stabilizing **H** by ligand substitutions therefore is a path to reducing the overpotential associated with catalysis (though overpotential is also influenced by other factors as well). Comparative LOBA analysis of **H** and **E** suggests that such an effect is possible because Mo electrons in **H** exhibit delocalization onto the ligand that is not present in **E** (see Figure 3.5). Therefore, **H** may be stabilized and the overpotential reduced by adding electron-withdrawing groups on the para positions of the $PY5Me_2$ ligand platform.

In order to explore this possibility computationally, electron-withdrawing (fluorine) and electron-donating (methyl) groups were substituted at the para positions of all the pyridine rings (Figure 3.13), which are in principle synthetically feasible sites for modification. These groups were added at the bond lengths and angles equivalent to those found by performing an optimization (B3LYP/6-31G*) on just a single substituted pyridine ring; the rest of the structure remained the same as the unsubstituted catalyst. Single point calculations were then performed at the BP86/TZV-P/6-311G** level of theory. We assumed that the solvation corrections were unaffected by the substitutions. The shifts in reduction potentials and reaction barriers are then evaluated by isodesmic cycles, which should lead to favorable error cancellation.

First, let us summarize the calculations of substituent effects on the reduction potentials. For the first reduction, there is no change: the relative energy of **A** and **C** shifted by only 0.01 V for both substitutions. Chemically, we expect the change to be small because the relatively localized d-electrons of both **A** and **C** should be unaffected by these distant substitutions. For the second reduction, the relative energy between **C** and **E** increased by

Figure 3.13: Schematics of the fluorine (a) and methyl (b) substituted species of **A**.

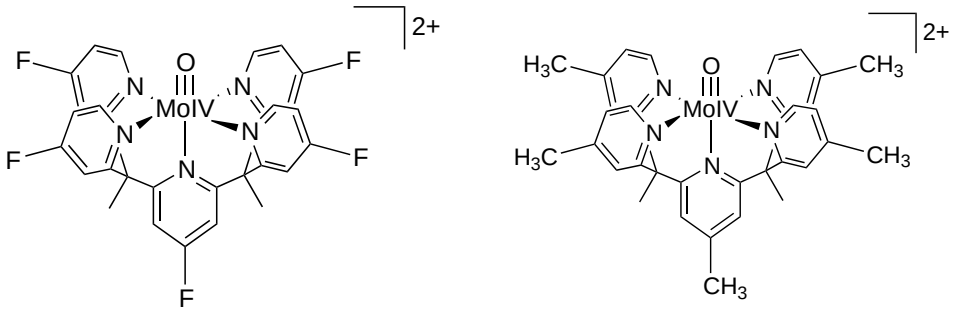

(a) (b)

0.04 V for the fluorination and 0.10 V for the methyl substitution. Once again these small shifts can be explained by LOBA; any electron delocalization of **E** is minor in comparison to that of species **H**. For the targeted third reduction, substituent effects stabilized **H** relative to **E** by 0.20 V for the fluorinated complex, while they led to a destabilization of 0.40 V for the methylated complex. These results demonstrate the utility of the LOBA analysis, and provide encouragement for further experimental studies.

However, it is possible that chemical substitutions in the ligand support will have implications for the kinetics of the resulting catalyst. In order to assess if the rate of the reaction is affected by the substitutions, we applied the same fluorination and methylation modifications to the transition structures for intracomplex hydride migration and H_2 elimination.

These results are interesting in that both the fluorination and methylation slightly stabilize $\mathbf{H} \stackrel{\ddagger}{\rightarrow} \mathbf{I}$, **I**, and $\mathbf{I} \stackrel{\ddagger}{\rightarrow} \mathbf{B} + H_2$ relative to **H** by approximately 0.1 V, as shown in Figure 3.14. In contrast, the two substitutions had opposite effects on the stability of **H** relative to the less reduced species. The stabilization reduces the barrier for the first rearrangement and thus increases the rate for the first step. The barrier for the α-H abstraction step was unaffected by the substitutions and is still lower than that for H_2O cleavage, which implies that the cleavage step is still rate-limiting. Therefore the reduction of this barrier by these substitutions increases the overall rate. Finally, referring back to the possibility of a two-electron redox cycle, our fluorination/methylation substitutions did not lower the rate for conversion from $\mathbf{E} \stackrel{\ddagger}{\rightarrow} \mathbf{F}$ enough to make it a viable pathway, and this remains an interesting challenge for future studies. A recent report by Solis and Hammes-Schiffer [182] showed for a wide variety of substituted cobaloxime complexes, all the redox couples' reduction potentials shifted in the same direction depending on the nature of the substituent (i.e. electron withdrawing or donating). This is in contrast to this study where we find that the first two reductions are minimally affected by substitution and only the last shows a significant shift.

Figure 3.14: The Gibbs free energy diagram for the liberation of hydrogen from **H**, including the two new species in Figure 3.13. The fluorinated species is the red line and the methylated species is a dotted green line; they lie almost on top of each other. The barrier for the first reaction is lowered and the second remains approximately the same. Again rather than spuriously attempt to take into account the complications involved in calculating the water association energies for a molecule already solvated in water, the complexation energy was set to zero.

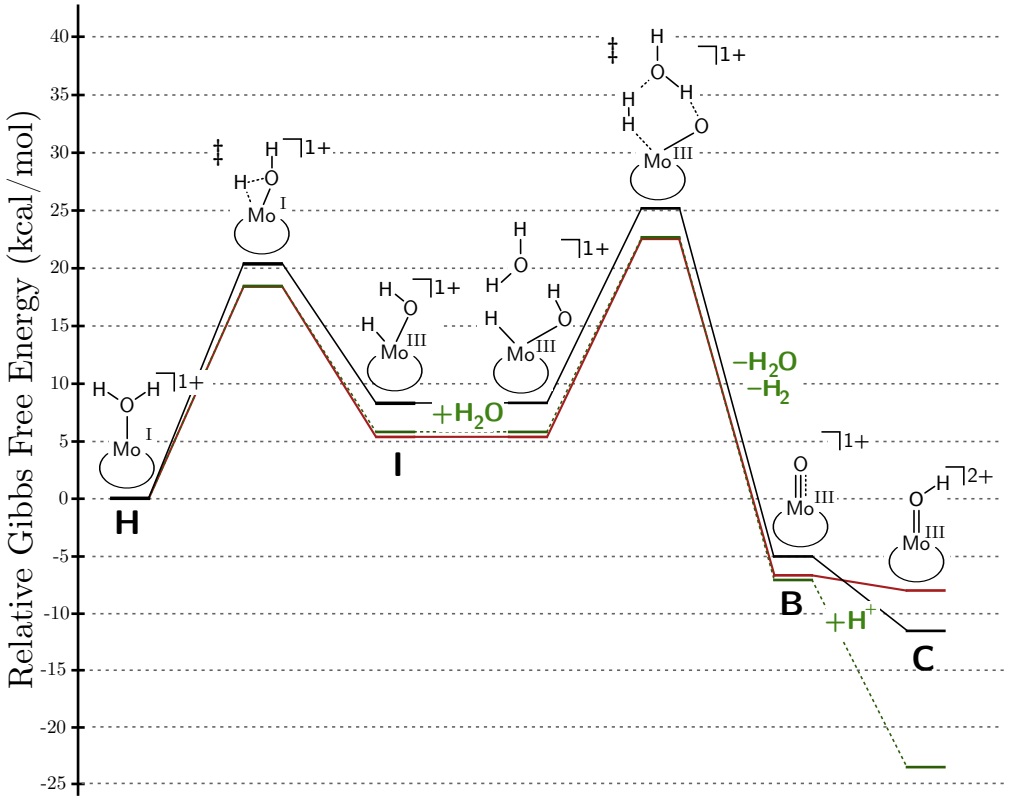

3.4 Conclusions

Based on extensive computational studies and additional experiments, our main findings on the mechanism of the catalytic generation of hydrogen from water by $[(PY5Me_2)MoO]^{2+}$ are as follows:

(1) We have identified an experimentally and computationally consistent mechanism involving three electrochemically generated intermediates (i.e. three reductions) and two transition structures. Referring to Figure 3.2, our overall pathway is $\mathbf{A} \longrightarrow \mathbf{C} \longrightarrow \mathbf{E} \longrightarrow \mathbf{H} \overset{\ddagger}{\rightarrow} \mathbf{I} + H_2O \overset{\ddagger}{\rightarrow} \mathbf{B} + H_2O + H_2 + H^+ \longrightarrow \mathbf{C}$. Based on new experimental data, the first two reductions are proton-coupled.

(2) We calculated reduction potentials which are in acceptable agreement ($\pm$ 0.3 V) with

the experimental values. The two activated steps consist of reductive cleavage of ligated H_2O, which is rate-determining, and an α-H abstraction to yield H_2 that occurs most favorably when mediated by a bridging water molecule. Calculated kinetic barriers are in reasonable agreement with the barrier inferred from the experimental turnover rate.

(3) We presented a mechanism for the stoichiometric reaction of the triflate precursor, $[(PY5Me_2)Mo(CF_3SO_3)]^{1+}$, to yield **A** and H_2. It differs from the catalytic cycle above in that no intermediates with +1 charge state are accessed. It is conceivable to run this mechanism under potential bias as a catalytic cycle with a lower overpotential because this cycle avoids the third reduction. However, the calculated kinetics are very slow.

(4) We have performed detailed computational analysis of the nature of the three reductions of the catalytic cycle, showing that the third reduction leads to metal orbitals that delocalize significantly onto the ligand support in contrast to the earlier intermediates. This provides a basis for stabilizing the result of the third reduction with the use of electron withdrawing groups. As a proof of concept, we fluorinated at the para-positions of all the pyridine rings, which is predicted computationally to lower the potential for the final reduction by 0.2 V. The kinetics are predicted to be slightly enhanced as well.

Chapter 4

Non-Orthogonal Configuration Interaction for the Calculation of Multielectron Excited States

4.1 Introduction

With vital applications in the photophysics of vision, photosynthesis, and solar energy conversion, proper modeling of molecular excited states is an important challenge for quantum chemistry. Multielectron excitations are particularly interesting, as they play a significant role in molecules with extended conjugation, such as those in biology[183] and those used in organic photovoltaics[184], and are a necessary component for understanding multiexciton formation[185, 186], which could potentially lead to the enhancement of solar cell efficiencies. Modeling of multielectron excitations is difficult because the most commonly used and computationally efficient ground-state methods, when applied to excited states, fail to capture excitations of this character.

The most commonly used electronic structure method to compute excited states is the time dependent variety of density functional theory (TDDFT)[187, 188], but because the most computationally tractable solution to the TDDFT equations utilize a linear response formalism they are unable to treat multielectron excitations.[189, 190] Although there have been a number of developments toward a DFT-based theory to treat double excitations[191–193] these methods are not in common use and still suffer from many of the same issues which plague ground-state DFT: choice of functional, approximate functionals may yield non-variational energies, etc.

The coupled-cluster formalism is a successful ground state theory which when expanded to treat excited states is able to capture double excitations. These methods include equation-of-motion coupled-cluster[194] and linear response theories based upon approximations of this theory, CIS(D)[195], CC2, and CC3[196]. While coupled cluster is formally exact, in practice, the excitation level must be truncated at a given number of excited electrons,

typically single and double excitations (EOM-CCSD). In order to provide a satisfactory level of correlation for an excited state with an M electron excitation, an $M+1$ level of truncation is required[197]. Using a high-level truncation is problematic because the scaling of these methods are N^5 (CIS(D) and CC2), N^6 (EOM-CCSD), N^7 (CC3 and perturbative triples varieties of EOM-CC), and N^8 (EOM-CCSDT) where N is the size of the atomic orbital (AO) basis. Thus even a double excitation requires a 7th or 8th order scaling method.

Spin-flip (SF) methods, which have been utilized in configuration interaction (CI)[58], DFT[59], and CC[60] frameworks are another set of tools for treating mutlielectron excitations which do not suffer from the high scaling of the CC formalism. These methods begin with a high spin reference and then employ linear combinations of spin-flipping excitations ($\alpha \rightarrow \beta$) to access states with the desired M_s value, such as the ground state. The first of these methods was SF-CIS (spin-flip configuration interaction singles); this method did not provide spin eigenstates and thus SC-SF-CIS[198] (spin-complete SF-CIS) was developed to ameliorate this problem. SF-XCIS[199], which we shall apply to systems in this paper, is an extension to SC-SF-CIS which includes single excitations from the doubly-occupied space to the virtual space for all occupations of two electrons in the singly-occupied space. Restricted active space spin-flip configuration interaction variants (RAS-SF)[61–63] are the natural extension of SF-XCIS, which include larger numbers of spin-flips and use RAS techniques to include larger active spaces. Despite their success, the RAS-SF family of methods still suffers from some deficiencies: the excitation energies can be sensitive to the quality of the high-spin reference, these methods lack a full treatment of dynamic correlation, and these methods have exponential scaling with respect to active space size.

In order to properly treat multielectron excitations, quantum chemists typically resort to using a multiconfigurational wavefunction; of these, the most popular is the complete active space self-consistent-field (CASSCF) method[64], and its second-order perturbation-corrected variant (CASPT2)[65]. CASSCF involves optimizing the orbitals over all the configurations within an active space and thus scales exponentially with the active space size. This poor scaling limits this method to small basis sets and since appropriate active spaces generally grow with molecular size, to fairly small molecules. Substantial effort has been dedicated to reducing the exponential scaling of of CASSCF; one particularly promising direction is the Density Matrix Renormalization Group (DMRG)[66]. DMRG when paired with the CASSCF problem, effectively replaces the CI solver of CASSCF with the DMRG algorithm which is then able to solve the the CASSCF problem exactly in an active space with non-exponential cost for pseudo-linear systems. For 3-dimensional systems DMRG-CASSCF scales exponentially but still favorably with respect to traditional CASSCF solvers.

In this work we present an alternative multiconfigurational wavefunction for treating excited states, non-orthogonal configuration interaction (NOCI)[200, 201]. NOCI scales as $\mathcal{O}(M^2\max(n_e^3, N^2))$, where M is the number of determinants included, n_e is the number of electrons, and N is the size of atomic orbital basis. As we will show, the minimal size of M required to obtain qualitative results can be remarkably small for interesting molecules and thus this method is tractable for even large systems. In traditional CI approaches, one uses excitations out of the reference as the basis for interaction, typically truncating at some

number of excitations; singles, doubles, triples, etc. This basis is orthogonal because each state is formed from a combination of the canonical occupied and virtual orbitals which are mutually orthogonal spaces. Orthogonality is not a necessary requirement to perform CI, but chosen because of the ease with which one can compute the Hamiltonian matrix and thus diagonalize it to compute the energies and wavefunctions of the states.

When using different Hartree–Fock solutions as the basis for CI, as is done throughout this paper, the configurations are non-orthogonal. Non-orthogonality makes computation of the Hamiltonian in this basis slightly more complicated, but also potentially allows the basis to span more of the relevant configuration space than a truncated orthogonal one of the same size would. The NOCI wavefunction is a linear combination of multiple Slater determinants and thus applicable to both ground-state and excited-state multireference problems. NOCI may also be used to treat ground-state strong correlation problems, but that will not be our focus here. In order to provide more spin-pure excited states, we will be utilizing generalized Hartree–Fock (GHF)[202, 203] solutions. In GHF, the single particle functions are a linear combination of both up (α) and down (β) spin $|\chi_i(\mathbf{r},\xi)\rangle = |\psi_i^{\alpha}(\mathbf{r})\rangle\,|\alpha(\xi)\rangle + |\psi_i^{\beta}(\mathbf{r})\rangle\,|\beta(\xi)\rangle$[202]. Despite considerable discourse on symmetry breaking in HF[204–208], many of the broken-symmetry methods (other than simple unrestriction) never gained popularity within the quantum chemistry community, likely due to complications with interpretation (i.e. bad quantum numbers) and computational concerns.

Specifically we would like to point to the recent work of Scuseria and collaborators on the projected Hartree–Fock method (PHF)[209–212] (which is related to both NOCI and the older EHF)[213]. After being relatively ignored by the electronic structure community, GHF wavefunctions have been used by Scuseria and collaborators in their work on the projected Hartree–Fock method (PHF)[209–212]. In PHF, one applies projection operators to a broken-symmetry determinant to form an effective Hamiltonian which is then diagonalized until self-consistency. This scheme is a variation after projection (VAP) scheme which allows one to obtain the variationally minimum energy with respect to these broken-symmetry determinants. However, the variationally minimized wavefunction obtained only describes the ground state and thus PHF in the current form is not used to compute excited states for molecular systems (although research in this area is ongoing)[214]. Despite the recent success of this method it suffers from two flaws: it is neither size-consistent nor size-extensive[209]. By size-consistency we mean that the energy evaluated on two non-interacting fragments, A and B, is equal to the sum of their individually evaluated energies: $E_{AB} = E_A + E_B$. Size-extensivity implies that when treating an infinite system, a method calculates a correlation energy per particle which does not vanish. A final important property of an excited state method is size-intensivity, which denotes the ability of a method to produce excited state energies which do not change with the addition of non-interacting fragments.

It is well known that orthogonal varieties of CI truncated at a particular level of excitation beyond singles, e.g. configuration interaction single and doubles excitations (CISD), are variational but not size-consistent nor size-intensive. On the other hand NOCI or an orthogonal version of the same method may be made size-consistent and the excitation energies made size-intensive. This is because a non-interacting fragment which by its very

nature must not participate in the excitation will not affect the calculation of the excitation energy i.e. the Hamiltonian will be block diagonal in the fragments. Of course this has the caveat that the number of excited determinants required to obtain the same accuracy for the two fragment calculation, assuming the fragments are identical, would be the square of that required for the independent systems. We should also state that for an interacting system the number of determinants necessary would also increase, likely in a non-linear way. NOCI does not provide size-extensive correlation energies for infinite completely interacting systems, but this limitation does not prevent us from studying the bulk of chemistry.

The remainder of this article is organized as follows: 1) we shall recapitulate the basic theory of NOCI, 2) describe our new spin-purification scheme and discuss our choice of CI basis, 3) we shall explore NOCI's effectiveness in calculating excited states by applying the method to the first four all-trans linear polyenes and the β-carotene molecule, 4) finally we shall draw some conclusions about how this theory fits into the current quantum chemistry toolbelt and discuss some future extensions for the theory.

4.2 Theory

The notation utilized in this work is as follows: NOCI wavefunctions: Φ; Slater determinants: Ψ with indices w, x to distinguish between different solutions; Spatial Molecular Orbitals (MO): ψ; Spatial Atomic Orbitals (AO): ω; AO Indices: lower case Greek μ, ν...; Virtual MO indices: a, b; Occupied MO indices: i, j; Generic MO indices: l, k. Bold case is employed for matrices. We employ the Einstein summation convention and the tensor notation with both covariant (subscript) and contravariant (superscript) indices of Head-Gordon et al.[23]

Basics

The general idea of NOCI is to build and diagonalize the Hamiltonian in a basis of Slater determinants, henceforth basis states, which are in general non-orthogonal. The non-orthogonality of the basis states introduces an overlap metric, $\mathbf{S}$, into the standard CI eigenvalue problem:

$$\mathbf{HD} = \mathbf{SDE} \tag{4.1}$$

where $\mathbf{H}$ is the Hamiltonian matrix, $\mathbf{D}$ are the expansion coefficients and $\mathbf{E}$ is a diagonal matrix of the energies. Thus NOCI requires one to compute the overlap and Hamiltonian between two generally non-orthogonal basis states; our method for this is outlined below for more details see Reference Thom2009a. Let us consider two solutions (Slater determinants):

$$|^{w}\Psi\rangle \quad \text{and} \quad |^{x}\Psi\rangle \tag{4.2}$$

each formed from n orthogonal occupied molecular orbitals:

$$|{}^{w}\phi_i\rangle = \sum_{\mu} |\omega_\mu\rangle \, {}^{w}C^{\mu\cdot}_{\cdot i} \tag{4.3}$$

$$|{}^{x}\phi_i\rangle = \sum_{\mu} |\omega_\mu\rangle \, {}^{x}C^{\mu\cdot}_{\cdot i} \tag{4.4}$$

These orbitals are orthogonal within a given set but non-orthogonal between the sets. We would like to form two sets of orbitals such that the occupied overlap matrix between the determinants is diagonal:

$$\langle {}^{w}\phi_i \,|\, {}^{x}\phi_j\rangle = s_i \delta_{ij} \quad \text{and} \quad 0 \leq |s_i| \leq 1 \tag{4.5}$$

To obtain these sets we use the corresponding orbitals of Amos and Hall[215, 216], also known as Löwdin-Paired orbitals[217]. The classic equations (see the appendix of Amos and Hall[215]) suggest diagonalizing the product ${}^{wx}\mathbf{S}^{\dagger}{}^{wx}\mathbf{S}$, where ${}^{wx}\mathbf{S} = {}^{w}C^{*\cdot\mu}_{i\cdot} S_{\mu\nu} {}^{x}C^{\nu\cdot}_{\cdot i}$ and $S_{\mu\nu}$ is the atomic orbital overlap matrix. We found it more numerically stable to use the singular value decomposition (SVD):

$${}^{wx}\mathbf{S} = {}^{w}C^{*\cdot\mu}_{i\cdot} S_{\mu\nu} {}^{x}C^{\nu\cdot}_{\cdot j} \tag{4.6}$$

$${}^{wx}\mathbf{S} = \mathbf{U}\sigma\mathbf{V}^{t} \quad \text{(SVD)} \tag{4.7}$$

$${}^{x}\tilde{\mathbf{C}} = {}^{x}\mathbf{C}\mathbf{V}^{t} \tag{4.8}$$

$${}^{w}\tilde{\mathbf{C}} = {}^{w}\mathbf{C}\mathbf{U}^{t} \tag{4.9}$$

where σ is a diagonal matrix of the singular values. It must be noted that in the formulation presented above there is a loss of phase information in the eigenvalues of ${}^{wx}\mathbf{S}$. Early proponents of these orbitals computed the determinants of both transformation matrices in order to preserve the phase. In our implementation, we compute the eigenvalues of the non-Hermitian matrix, ${}^{wx}\mathbf{S}$, and compare the product of its diagonal to that of the transformed set, changing the sign as necessary. After each pair of basis states are made biorthogonal, a set of generalized Slater–Condon rules[201, 215] may be used to compute the Hamiltonian matrix elements and then the general eigenvalue problem can be solved.

Extended Spin-Purification Scheme

Here we present a new spin-purification scheme for NOCI utilizing GHF-type determinants. In prior implementations of NOCI, in an attempt to purify spin-contaminated UHF solutions, two degenerate configurations, per one original UHF determinant, were included in the expansion: the excess α configuration and the excess β configuration[201]. When applied to only one UHF determinant this concept is known as the Half-Projected Hartree–Fock Method, an approximation to PHF in which one applies a spin projection operator that selects for either the even or odd quantum number $\mathcal{S}$. Consider a given UHF solution which

is exactly a linear combination of two spin-pure components such as a singlet and a triplet, by interacting the excess α and excess β determinants one is able to obtain the two spin-pure configurations by adding and subtracting the determinants appropriately. Within NOCI, the diagonalization of the Hamiltonian provides the proper signs to accomplish this.

In order to extend this spin-purification to determinants which are linear combinations of more than two spin components, we interact non-collinear (GHF) determinants. Applying the same corresponding orbital treatment as above, one obtains a similar set of Slater–Condon rules for matrix elements of the Hamiltonian operator in a basis of GHF solutions. In order to use these wavefunctions for spin-purification, we apply an AO based unitary rotation parameterized by an angle θ to the coefficient matrix which changes the direction of the S_z axis without changing the energy. Choosing a rotation angle of $\frac{\pi}{2}$ transforms the α component of each orbital into the β component of each orbital and is exactly equivalent to the UHF spin-purification scheme discussed above. Although these basis states are degenerate with their unrotated counterparts, they provide a new set of overlap and Hamiltonian matrix elements with the other basis states in the expansion and provide more variational flexibility in the CI. In this work we shall use a quadrature of n_q points equidistant between 0 and $\frac{\pi}{2}$ to allow spin-contaminated states to purify. That is if one originally began with 5 UHF determinants and $n_q = 5$, the NOCI Hamiltonian and overlap would be square matrices of dimension 25. This idea is very similar to the discretization of the gauge integration used for spin-projection in the PHF method[209] and thus we suspect that a small number of quadrature points will remove much of the spin-contamination.

In order to compute $\langle S^2 \rangle$ for a given state we evaluate the $\langle S^2 \rangle$ matrix elements for each pair of GHF determinants and then use the eigenvectors of the CI diagonalization to calculate the value of a given state. The matrix element for a pair of determinants ($|^w\Psi\rangle$ and $|^x\Psi\rangle$) is:

$$\left\langle {}^w\Psi \left| S^2 \right| {}^x\Psi \right\rangle = \left\langle {}^w\Psi \left| S_x^2 \right| {}^x\Psi \right\rangle + \left\langle {}^w\Psi \left| S_y^2 \right| {}^x\Psi \right\rangle \tag{4.10}$$

$$+ \left\langle {}^w\Psi \left| S_z^2 \right| {}^x\Psi \right\rangle \tag{4.11}$$

$$\left\langle {}^w\Psi \left| S_\sigma^2 \right| {}^x\Psi \right\rangle = \left\langle {}^w\Psi \left| S_\sigma \right| {}^w\Psi \right\rangle \left\langle {}^w\Psi \mid {}^x\Psi \right\rangle \left\langle {}^x\Psi \left| S_\sigma \right| {}^x\Psi \right\rangle \tag{4.12}$$

$$+ \sum_{ia} \left\langle {}^w\Psi \left| S_\sigma \right| {}^w\Psi_i^a \right\rangle \left\langle {}^w\Psi_i^a \mid {}^x\Psi \right\rangle \left\langle {}^x\Psi \left| S_\sigma \right| {}^x\Psi \right\rangle \tag{4.13}$$

$$+ \sum_{jb} \left\langle {}^w\Psi \left| S_\sigma \right| {}^w\Psi \right\rangle \left\langle {}^w\Psi \mid {}^x\Psi_j^b \right\rangle \left\langle {}^x\Psi_j^b \left| S_\sigma \right| {}^x\Psi \right\rangle \tag{4.14}$$

$$+ \sum_{ia,jb} \left\langle {}^w\Psi \left| S_\sigma \right| {}^w\Psi_i^a \right\rangle \left\langle {}^w\Psi_i^a \mid {}^x\Psi_j^b \right\rangle \left\langle {}^x\Psi_j^b \left| S_\sigma \right| {}^x\Psi \right\rangle \tag{4.15}$$

where $\sigma = x, y, z$. Here we inserted the resolution of the identity for each determinant ($|^w\Psi\rangle$) noting that the occupied and virtual spaces of each determinant are orthogonal, the occupied spaces between the determinants have been made biorthogonal (corresponding orbitals), and the virtual spaces remain non-orthogonal between the two determinants. In order to simplify these resolutions, we have used the property that the spin component operators are one-

electron operators and therefore only the ground-state and single-excitations couple through them. In Appendix B, we present a derivation for each matrix element in the above equation, resulting in a computation of $\langle S^2 \rangle$ for each determinantal pair which scales as N^3 where N is the size of the atomic orbital basis.

Basis States

Below, we present the algorithm used to obtain the set of non-orthogonal Slater determinants which form the basis for NOCI. We begin by converging a symmetry-preserving RHF solution. From this "ground-state", we form some subset of singly- and doubly-excited orthogonal determinants which are of chemical relevance. These explicitly unrestricted determinants are then allowed to optimize using the Maximum Overlap Method (MOM)[218] combined with the Direct Inversion of the Iterative Subspace (DIIS) extrapolation method[219, 220] until the DIIS error vector is less than 1.0×10^{-8}. It has been discussed at length[110, 201, 218, 221–223] that these states provide approximations to excited states despite not being orthogonal to the ground state.

The orbital optimization allows for both valence and core relaxation in the presence of the constrained occupancy of what would be virtual orbitals. This relaxation is an important component of the non-orthogonal expansion of the wavefunction and results in a more compact representation than its orthogonal counterpart. As we shall show, an orthogonal set of the same determinants performs poorly in the case of wavefunctions with multireference character. Admittedly, this relaxation is only occurring at the mean field level and thus cannot fully account for these correlations. The relaxation in NOCI is not like that of a CASSCF type wavefunction where all the orbitals are optimized in the presence of all the configurations included in the active space, but rather is a basis state specific optimization.

A development version of QCHEM 3.2[98] utilizing the Armadillo linear algebra library[224] and 6-31G*[165] atomic orbital basis was used for all calculations. All geometries were obtained from optimizations performed with the same basis set using the B3LYP functional[40].

4.3 Results

Polyenes

The linear polyenes have long been used for testing new excited state methods in electronic structure theory. This is primarily due to the fact that two of the low singlet excited states are of significantly different character. The $1^1\mathrm{B}_u^+$ state is experimentally "bright" (dipole allowed) and primarily of single excitation character, while the $2^1\mathrm{A}_g^-$ state is "dark" (dipole forbidden) and has considerable double excitation character. These two excitations will be the main focus of this study because they are low in the energy spectrum for the whole range of systems investigated here. For the longer polyenes, it has been shown that the $1^1\mathrm{B}_u^-$ state

becomes lower in energy than the $1^1B_u^+$ state for $n = 7$, and by $n = 11$ (where n is defined by $C_{2n}H_{2n+2}$), the $3^1A_g^-$ state is also below the $1^1B_u^+$ state[225].

Due to the chemical similarities of the systems studied in this work (all-*trans* polyenes and β-carotene), the basis states chosen to represent the final wavefunction were the same. We limited the number of basis states to 10 for two reasons: this allowed us to use a higher number of quadrature points for the new spin-purification scheme and showed that even in this greatly reduced space, NOCI performs quite admirably. The set of basis states consisted of:

1. The symmetric RHF determinant.
2. $b_g \rightarrow a_u^*$ (HOMO $\rightarrow$ LUMO).
3. $a_u \rightarrow a_u^*$ (HOMO-1 $\rightarrow$ LUMO).
4. $b_g \rightarrow b_g^*$ (HOMO $\rightarrow$ LUMO+1).
5. $a_u \rightarrow b_g^*$ (HOMO-1 $\rightarrow$ LUMO+1).
6. $(b_g)^2 \rightarrow (a_u^*)^2$ (HOMO^2 $\rightarrow$ LUMO^2).
7. $(b_g)^2 \rightarrow (b_g^*)^2$ (HOMO^2 $\rightarrow$ LUMO+1^2).
8. $(a_u)^2 \rightarrow (a_u^*)^2$ (HOMO-1^2 $\rightarrow$ LUMO^2).
9. $b_g a_u \rightarrow (a_u^*)^2$ (HOMO, HOMO-1 $\rightarrow$ LUMO^2).
10. $(b_g)^2 \rightarrow a_u^* b_g^*$ (HOMO^2 $\rightarrow$ LUMO, LUMO+1).

Specifically determinant 6 was included in order to target the known double-excitation character of the $2^1A_g^-$ state in the polyenes. For all systems, the excited determinants were optimized within the UHF framework but despite this some of the double excitation 6-8 were found to be solutions of the RHF equations; the determinants had equal α and β coefficients.

Butadiene

For theoreticians, even the simplest of the linear polyenes, butadiene, has long been a challenge. Many theoretical techniques have been applied to butadiene, including configuration interaction singles (CIS), TDDFT[226], second-order algebraic diagrammatic construction (ADC(2))[227], equation of motion coupled-cluster (EOM-CC)[228, 229], CC2 and CC3[230], symmetry adapted cluster configuration interaction (SAC-CI)[231, 232], CASSCF[233, 234], CASPT2[233, 235], restricted active space SCF (RASSCF)[236], RASCI-SF[63], and multireference Møller-Plesset (MRMP)[234]. The relative ordering of the $1^1B_u^+$ and $2^1A_g^-$ states in butadiene has a long record of controversy in theoretical work, due to the sheer number of methods applied. Recently, this controversy has been laid to rest by the work of Watson and

Table 4.1: Absolute ground state energies (a.u.) and vertical excitation energies (eV) and $\langle S^2 \rangle$ for butadiene with various levels of GHF quadrature (n_q).

	$1^1A_g^-$		$1^1B_u^+$		$2^1A_g^-$	
State	a.u.	$\langle S^2 \rangle$	eV	$\langle S^2 \rangle$	eV	$\langle S^2 \rangle$
$n_q = 2$	-154.93643	0.001	7.63	0.007	6.72	0.353
$n_q = 5$	-154.93647	0.000	7.61	0.002	6.63	0.096
$n_q = 10$	-154.93647	0.000	7.61	0.002	6.63	0.095
$n_q = 30$	-154.93647	0.000	7.61	0.002	6.63	0.094

Chan[229]. They applied high-level EOM-CC theory, including extrapolation to the complete basis set limit and estimates for core excitations. They found that the vertical excitation energy of the $1^1B_u^+$ state (6.21 $\pm$ 0.02 eV) lies below the $2^1A_g^-$ state (6.41 $\pm$ 0.07 eV) in contrast to some previous results. In their work, they conclude that the most cited experimental value for the $1^1B_u^+$ excitation, 5.92 eV from electron impact energy loss spectroscopy[237], is likely not a truly vertical excitation and that the experimental results for the notoriously difficult dipole forbidden $2^1A_g^-$ state are not precise enough for comparison.

In order to assess the value of utilizing the non-collinear (GHF) quadrature for spin-purification, we applied the method with various values of n_q to butadiene. In Table 4.1, we present both the vertical excitation energies and the $\langle S^2 \rangle$ values. The character of all of the NOCI states were assigned by inspecting the components of the CI eigenvector for large weights on determinants of the approximately the correct symmetry and character. When only applying the two state spin-purification scheme ($n_q = 2$), despite having a reasonable excitation energy, the $2^1A_g^-$ state is fairly spin contaminated; this is likely due to the fact that this state contains a linear combination of two open shell singlets i.e. $a_u \rightarrow a_u^*$ (HOMO-1 $\rightarrow$ LUMO) and $b_g \rightarrow b_g^*$ (HOMO $\rightarrow$ LUMO+1), with $\langle S^2 \rangle$ values of 1.07 and 1.14 respectively. It looks as though increasing the non-collinear basis can only reduce spin contamination to a finite value without inclusion of more states. Small eigenvalues of the overlap matrix in the NOCI generalized eigenvalue problem are representative of linear dependencies in our basis states. If one investigates these values as n_q is increased from 10 to 30, the number of these below a threshold increases by almost the same number as the number of new determinants. This indicates that for this system, the Hilbert space has been saturated and increasing the quadrature beyond as $n_q = 10$ will not change the answer greatly. The fact that this saturation occurs before $\langle S^2 \rangle = 0$ is interesting and will be investigated in the future.

For butadiene it should be noted that the ordering of the two singlet excited states is incorrect with respect to the results of Watson and Chan[229]. This can be explained by the fact that we are primarily targeting static correlation in our basis states, the primary type of correlation for the $2^1A_g^-$ state; a proper treatment of the $1^1B_u^+$ state requires more dynamic correlation.

Table 4.2: Absolute ground state energies (a.u.), vertical excitation energies (eV), and $\langle S^2 \rangle$ shown in () for the all-*trans* polyenes $C_{2n}H_{2n+2}$ with $2 \leq n \leq 11$ from different theories. Here, OCI is a multireference CI where the only included configurations are the same configurations as those included in the NOCI, albeit their orthogonal unrelaxed counterparts.

n	State	CIS	SF-XCIS	NOCI ($n_q = 2$)	NOCI ($n_q = 10$)	OCI	Δ(OCI-NOCI)	CASCI-MRMP	CASPT2
2	$1^1A_g^-$		-154.98077	-154.93643 (0.00)	-154.93647 (0.00)	-154.93537	0.00110		
	$1^1B_u^+$	6.79	7.23	7.63 (0.01)	7.61 (0.00)	7.85	0.24	6.21[1]	6.27[3]
	$2^1A_g^-$	9.24	7.23	6.72 (0.35)	6.63 (0.10)	8.61	1.98	6.31	6.23
3	$1^1A_g^-$		-231.86320	-231.81963 (0.00)	-231.81965 (0.00)	-231.81768	0.00196		
	$1^1B_u^+$	5.69	6.22	6.57 (0.04)	6.51 (0.01)	6.38	-0.13	5.25[2]	5.19
	$2^1A_g^-$	8.12	6.53	6.32 (0.29)	6.23 (0.08)	7.37	1.14	5.10	5.01
4	$1^1A_g^-$		-308.75426	-308.70398 (0.00)	-308.70398 (0.00)	-308.70264	0.00134		
	$1^1B_u^+$	4.97	5.65	5.59 (0.07)	5.52 (0.02)	5.67	0.16	4.57	4.38[4]
	$2^1A_g^-$	7.23	5.36	5.22 (0.48)	5.09 (0.14)	6.69	1.60	4.26	4.42
5	$1^1A_g^-$		-385.63800	-385.58980 (0.00)	-385.58982 (0.00)	-385.58825	0.00157		
	$1^1B_u^+$	4.47	5.11	4.94 (0.09)	4.86 (0.03)	5.10	0.24	4.17	
	$2^1A_g^-$	6.54	4.90	4.73 (0.53)	4.59 (0.16)	6.27	1.68	3.68	
6	$1^1A_g^-$		-462.52693	-462.47573 (0.00)	-462.47575 (0.00)	-462.47427	0.00149		
	$1^1B_u^+$	4.11	4.83	4.45 (0.12)	4.35 (0.03)	4.70	0.34	3.87	
	$2^1A_g^-$	6.00	4.58	4.25 (0.67)	4.10 (0.21)	6.00	1.90	3.19	
7	$1^1A_g^-$		-539.41218	-539.36198 (0.00)	-539.36201 (0.00)	-539.36047	0.00154		
	$1^1B_u^+$	3.83	4.52	4.09 (0.14)	3.98 (0.04)	4.25	0.28	3.60	
	$2^1A_g^-$	5.55	4.25	3.93 (0.78)	3.77 (0.25)	5.37	1.60	2.80	
8	$1^1A_g^-$		-616.29917	-616.24832 (0.00)	-616.24837 (0.00)	-616.24692	0.00145		
	$1^1B_u^+$	3.61	4.34	3.80 (0.17)	3.67 (0.05)	4.05	0.37	3.38	
	$2^1A_g^-$	5.19	4.07	3.63 (0.92)	3.46 (0.33)	5.16	1.69	2.50	
9	$1^1A_g^-$		-693.18618	-693.13482 (0.00)	-693.13488 (0.00)	-693.13348	0.00140		
	$1^1B_u^+$	3.43	4.17	3.57 (0.21)	3.43 (0.06)	4.02	0.59	3.18	
	$2^1A_g^-$	4.88	3.91	3.39 (1.07)	3.19 (0.37)	5.63	2.44	2.25	
10	$1^1A_g^-$		-770.07316	-770.02148 (0.00)	-770.02157 (0.00)	-770.02012	0.00145		
	$1^1B_u^+$	3.29	4.06	3.39 (0.24)	3.24 (0.07)	3.89	0.66	3.00	
	$2^1A_g^-$	4.62	3.80	3.17 (1.25)	2.94 (0.48)	5.52	2.58	2.04	
11	$1^1A_g^-$		-846.96019	-846.90829 (0.01)	-846.90844 (0.00)	-846.90683	0.00160		
	$1^1B_u^+$	3.17	3.96	3.23 (0.29)	3.07 (0.09)	3.80	0.74	2.84	
	$2^1A_g^-$	4.40	3.71	3.11 (1.23)	2.83 (0.47)	5.31	2.49	1.86	

[1] Reference [234]. Basis set:Dunning "QZ3p" (Carbon:5s4p3d,Hydrogen:3s2p), Active Space: (4,8), Geometry: Experimental

[2] Reference [225]. Basis set: cc-pvDZ, Active Space: (10,10) Geometry: Møller-Plesset 2nd Order Perturbation Theory

[3] Reference [238]. Basis set: ANO (Carbon:4s3p2d,Hydrogen:3s2p)+diffuse functions, Active Space: Full π-space, Geometry: Experimental

[4] Reference [233]. Basis set: ANO (Carbon:4s3p1d,Hydrogen:2s1p)+diffuse functions, Active Space: Full π-space, Geometry: CASSCF

Linear Polyenes

We shall now test NOCI on the longer polyenes comparing to both reference methods and methods with similar scaling. In Table 4.2, the vertical excitation energies of the linear polyenes with NOCI $n_q = 2$ and $n_q = 10$ are shown in comparison with other obtained theoretical values. We have included CASPT2 because of this method's popularity in treating multireference excited states and the more recent CASCI-MRMP results[225] in order to provide a benchmark. It should be noted that when comparing these results, the excitation energies will be dependent on many computational parameters such as geometry and basis set and thus the CASPT2 and CASCI-MRMP results cannot be directly compared with those calculated in this work. In order to provide a comparison with methods which have similar scaling and expected accuracy, we have also included results from CI Singles (CIS) and SF-XCIS[199], calculated using the same geometry and basis set. We have chosen not to include TDDFT results despite previous work[226] because, as stated early, TDDFT would not accurately reproduce double excitations and will suffer from the same failings as CIS. Table 4.2 also includes data for "OCI", by which we mean an orthogonal version of CI including the same 10 states as NOCI albeit their unrelaxed counterparts.

First, we will consider the NOCI spin-purification scheme, comparing the results of $n_q = 2$ with that of $n_q = 10$ shows that the change in excitation energies increases as n increases, reaching a final value of ~ 0.3 eV for the $2^1\mathrm{A}_g^-$ state of 11-ene. These changes in energy are directly correlated with the amount of original spin-contamination in these states at the $n_q = 2$ level. Figure 4.1 shows the change in $\langle S^2 \rangle$ for both excited states as a function of chain length for both levels of quadrature. Again the quadrature is able to reduce spin-contamination by about a factor of three for all states. It seems it may be beneficial to increase n_q as the amount of spin-contamination increases in the basis states but in order to maintain a consistent comparison we have remained at $n_q = 10$.

Let us begin now compare the energies of OCI to those of NOCI; Table 4.2 contains a column for both OCI and energy change with respect to NOCI ($n_q = 10$) (Δ(OCI-NOCI)) and Figure 4.2 contains the OCI and NOCI ($n_q = 10$) results plotted with respect to chain length. Clearly, OCI does not provide an accurate description of the doubly excited $2^1\mathrm{A}_g^-$ state and the relaxation of the orbitals by NOCI decreases the energy of this state by greater than 1 eV for the whole set of molecules. NOCI is able to account for substantial additional correlation energy when compared to an orthogonal CI with the same number of determinants; i.e. NOCI contains a more compact representation of the true wavefunction and encompasses more of the relevant configuration space. The difference between OCI and NOCI is not as pronounced for the $1^1\mathrm{B}_u^+$ state, where the state is primarily a single configuration and thus treated comparably by both OCI and NOCI. As the chain length increases (approximately at $n = 8$), the single configuration picture of the $1^1\mathrm{B}_u^+$ breaks down and OCI and NOCI begin to diverge. This is an indication that the relaxation in the determinants which make up the $1^1\mathrm{B}_u^+$ state in NOCI are beginning to take on character of more than one orthogonal state.

A subset of the results in Table 4.2 are included in Figure 4.3 in order to highlight the

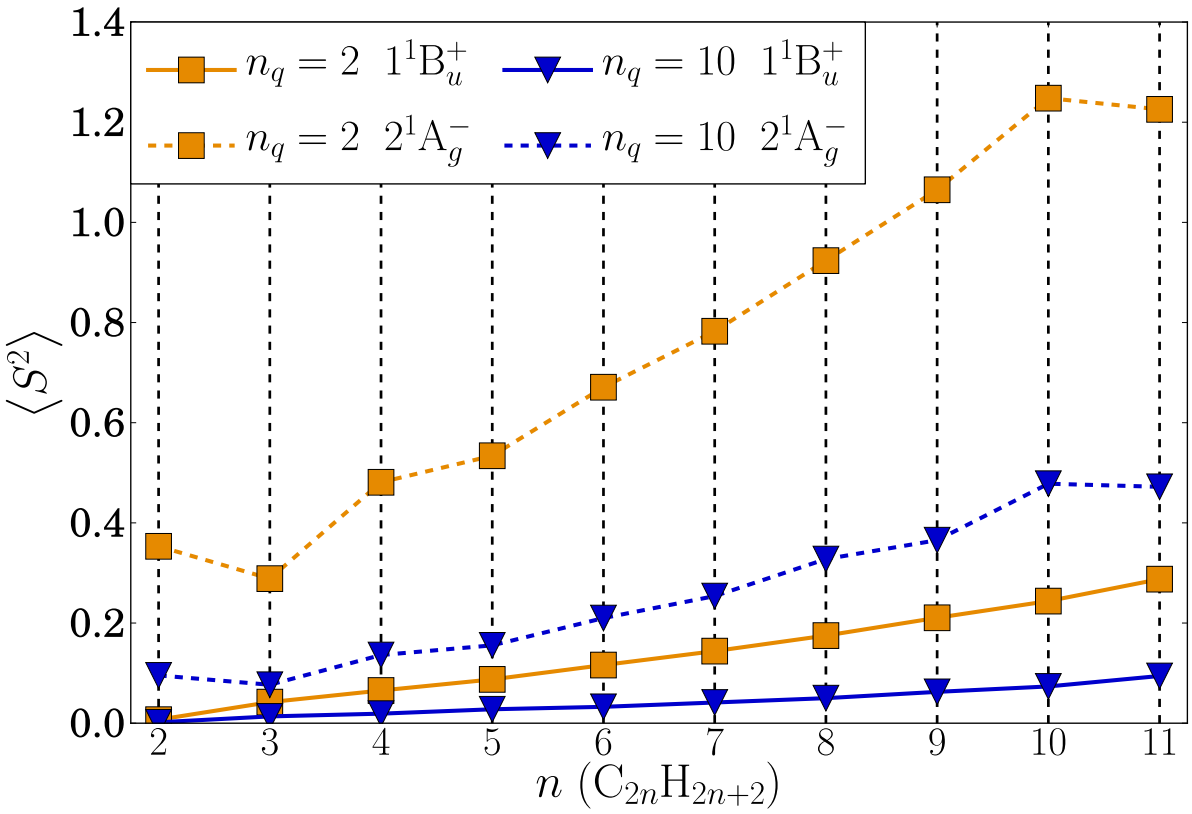

Figure 4.1: $\langle S^2 \rangle$ values for the linear polyenes for NOCI with a non-collinear (GHF) quadrature (n_q) of 2 and 10. Increasing the quadrature decreases the spin-contamination by a factor of 3 for all states. The ground states are not shown here as they are very close to zero and remain so with increasing quadrature.

trends of these methods as the chain length increases. Moving on to the results for CIS when compared to the reference CASCI-MRMP, we see that CIS cannot qualitatively reproduce the excitation energy of the $2^1A_g^-$ state. It places the $2^1A_g^-$ state well above the $1^1B_u^+$ state for all systems studied. This is not just an error in the excitation energy; CIS cannot correctly describe the character of the $2^1A_g^-$ state, due to a lack of double excitations. This deficiency also appears in the wavefunction where the two largest CIS amplitudes for the $2^1A_g^-$ state are HOMO-1 $\rightarrow$ LUMO and HOMO $\rightarrow$ LUMO+1; this same type of behavior would occur in TDDFT as well. On the other hand CIS treats the $1^1B_u^+$ state quite well, paralleling the CASCI-MRMP results.

Unlike CIS, SF-XCIS, by the inclusion of a (2,2) active space treats the doubly excited character of the $2^1A_g^-$ excited state appropriately. For all systems, the largest component of the SF-XCIS wavefunction of the $2^1A_g^-$ state is the HOMO $\rightarrow$ LUMO doubly excited state, with smaller components on other states of the correct symmetry. Although SF-XCIS shows the two states reversing order twice between $2 \leq n \leq 4$ (when the correct result is one crossing

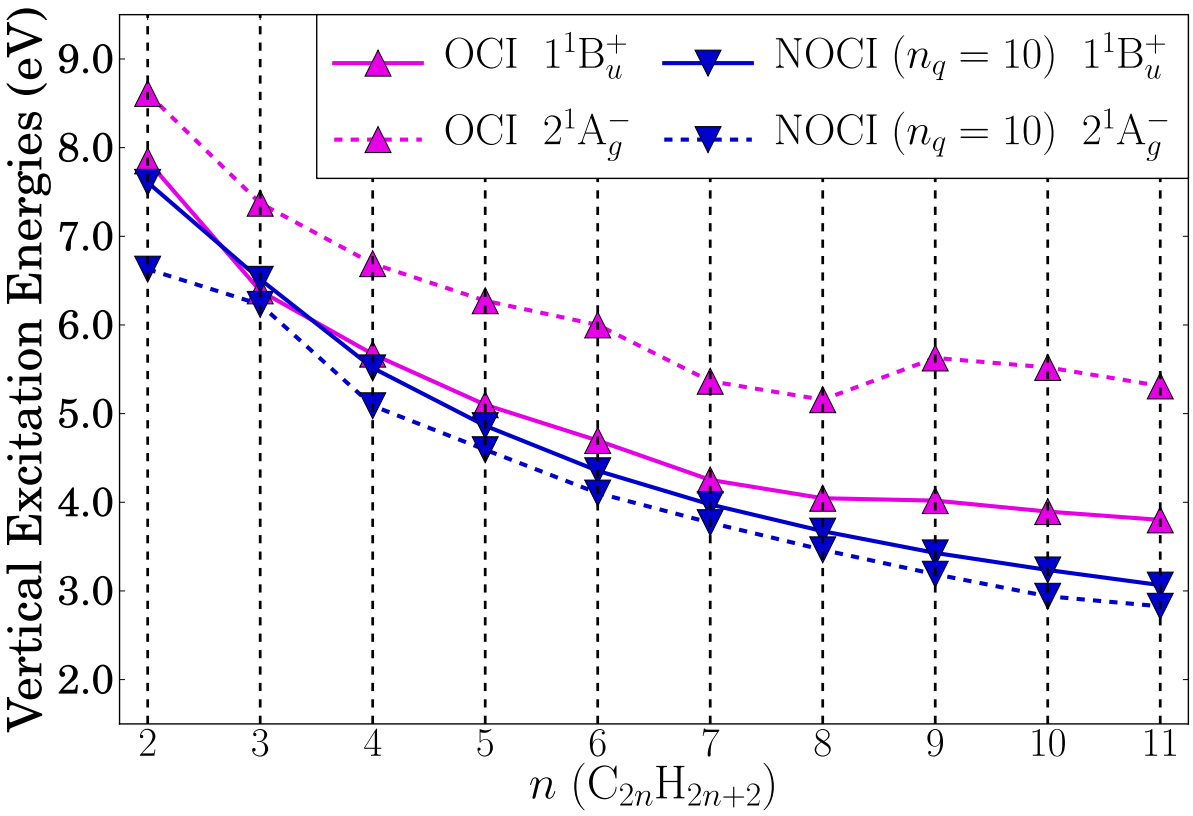

Figure 4.2: Polyene singlet vertical excitation energies (eV), comparing the NOCI ($n_q = 10$) and OCI results. OCI is a multireference CI where the only included configurations are the same configurations as those included in the NOCI, albeit their orthogonal unrelaxed counterparts.

around $n = 3$ (hexatriene)), the method does recover the correct ordering of these two states for the longer chains. Comparing NOCI with SF-XCIS, it is amazing that NOCI using only 10 determinants can compete with SF-XCIS, a method which includes more doubles excitations than NOCI, some triple excitations, and an increasing configuration space with molecular size. This again shows the power of using relaxed non-orthogonal configurations when compared to their orthogonal counter parts. For longer polyenes, the relative energy of these two states becomes constant in both NOCI and SF-XCIS, which is in contrast to the behavior of the reference method CASCI-MRMP, which for longer chains shows an increase in the separation of these two states. For SF-XCIS, this degradation indicates that one may need to increase the active space and potentially the number of spin-flips. For NOCI, one should use more than 10 determinants to treat a polyene chain of length $n = 11$ but for the purposes of illustrating the applicability of this method and for a fair comparison across these systems we thought this number of basis states to be sufficient.

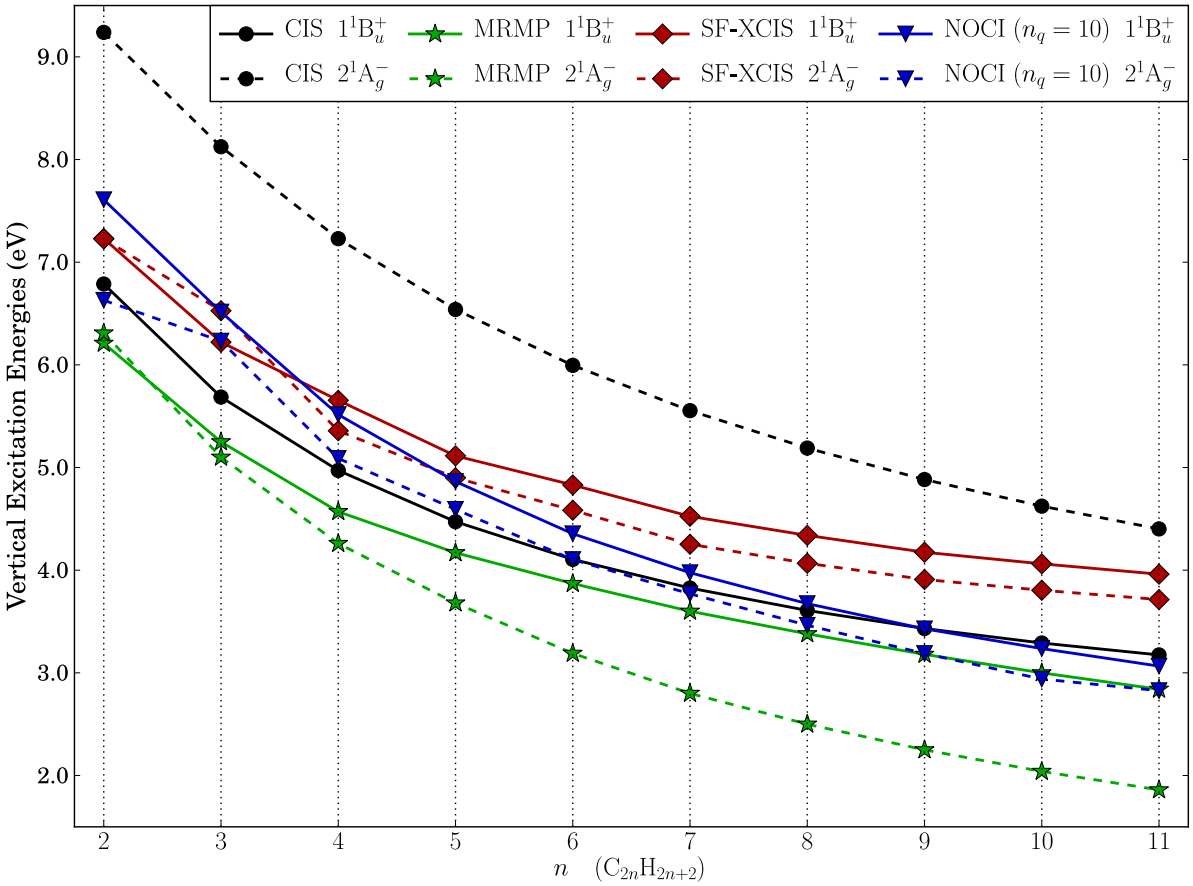

Figure 4.3: Polyene singlet vertical excitation energies (eV), comparing the NOCI ($n_q = 10$) results with CIS, SF-XCIS, and CASCI-MRMP. Solid lines: $1^1B_u^+$. Dashed lines: $2^1A_g^-$. Using CIS is insufficient to treat the $2^1A_g^-$ excited state. NOCI and SF-XCIS do comparably well for the shorter chains but NOCI outperforms SF-XCIS in the long chain limit.

β-Carotene

Carotenoids are an important class of biological molecules because they, along with chlorophylls, comprise a substantial fraction of the chromophores involved in light-harvesting in plants and cyanobacteria. Carotenoids provide two functions in photosynthetic organisms: they directly absorb light energy for use in photosynthesis and also participate in a photoprotection mechanism. For a thorough discussion of experimental and theoretical results for these systems, including the difficulty in peak assignment, we recommend the review of Polívka and Sundström.[239] Having been featured in two prior electronic structure studies, we chose β-carotene (a carotenoid with 11 double bonds) as a sample carotenoid to examine the performance of NOCI on these biologically-relevant molecules. This is an interesting test case for NOCI, because the lower symmetry of this molecule lends itself naturally to the breaking of spatial symmetry within the excited state determinants. Historically the

Table 4.3: Vertical excitation energies (eV) and $\langle S^2 \rangle$ shown in () for of the β-carotene with a variety of methods.

State	$2^1A_g^-$	$1^1B_u^+$	$\Delta E\left(1^1B_u^+ - 2^1A_g^-\right)$
NOCI ($n_q = 10$)	2.94 (0.53)	3.20 (0.08)	0.26
SF-XCIS	3.87	3.97	0.10
DMRG-CASSCF[1]	2.99	> 4.31	> 1.32
DFT/MRCI[2]	1.96	2.42	0.42

[1] Reference [240].
[2] Reference [242].

excited states of the carotenoids have been labeled S1, S2, etc; here we shall opt to reuse the polyene excited state nomenclature despite β-carotene having a lower point group symmetry. Table 4.3 shows the vertical excitation energies and $\langle S^2 \rangle$ values for β-carotene with NOCI, SF-XCIS and two other methods: Density Matrix Renormalization Group CASSCF (DMRG-CASSCF)[240], which was discussed in the Introduction, and DFT/MRCI[241, 242], which we shall describe briefly now.

DFT/MRCI is a semi-empirical procedure combining DFT for dynamic correlation and MRCI for strong correlations and excited states. This method involves a number of features including an efficient parallelization scheme, an extensive configuration selection, and use of the resolution of the identity (RI) approximation for four-index integrals. Despite these advantages, DFT/MRCI still possesses drawbacks such as choice of functional, empirical parameters for forming the effective Hamiltonian and use of an empirical recipe to avoiding double counting of correlation effects. Even with the considerable configuration selection, the method requires millions of configuration state functions for a molecule of the size of β-carotene. Because this method does include dynamic correlation, we will consider it a possible benchmark, keeping in mind that it is difficult to estimate the errors for a method which is non-variational.

To our knowledge, these are the only two studies of β-carotene applying modern electronic structure methods which can qualitatively treat double excitations. TDDFT has been applied to study the $S_0 \rightarrow S_2$ transition[243], but as stated previously, standard linear-response TDDFT cannot accurately treat double excitations[189, 190] and thus should not be trusted for any transitions involving the $2^1A_g^-$ state, including investigations of potential energy surfaces.

In the DMRG-CASSCF work, the authors averaged over the four lowest eigenstates and thus within their calculation were unable to obtain the $1B_u^+$ state. They found a state ordering of $1^1A_g^- < 2^1A_g^- < 1^1B_u^- < 3^1A_g^-$ with excitation to the $3^1A_g^-$ at 4.31 eV, which gives a lower bound to the $1B_u^+$ state. This ordering is correct within the active space but CASSCF does not include any dynamic correlation outside of this space (e.g. σ-π) , which is known to be important for the $1B_u^+$ state. In fact, DFT-MRCI, a method which includes

these σ-π correlations, orders the states as $1^1A_g^- < 2^1A_g^- < 1^1B_u^+ < 1^1B_u^- < 3^1A_g^-$. If we consider DFT/MRCI to include all correlation effects and DMRG-CASSCF to include all static correlation effects, then the difference between these two methods gives us an estimate for the total amount of dynamic correlation in each state: the $2^1A_g^-$ and $1^1B_u^+$ states have dynamic correlation of ~ 1 eV and > 2 eV, respectively. From this estimate, we can see that neither NOCI nor SF-XCIS (methods designed primarily to treat static correlation) are truly able to determine the state ordering as neither value is separated by the > 1 eV difference that would be added by a more complete treatment of dynamic correlation. In comparison to SF-XCIS, NOCI does provide a better estimate of the gap between these two states. Considering the difference in the complexity of the wavefunctions of these methods, it is striking that NOCI is able to achieve the results that it does. Comparing the results of both NOCI and SF-XCIS on β-carotene to that of the polyenes, we see that these methods treat this systems as a polyene of approximately length $n = 10$, which is consistent with the fact that the conjugation of β-carotene is broken by the slight twist in the polyene backbone of the molecule. Again the differences between NOCI and the reference could likely be reduced by the inclusion of more states; specifically one would like to include more double excitations, which are of known importance to molecules with this length of conjugation. We want to stress that in this current form of "hand"-picking excited determinants, NOCI cannot be expected to stand up against DFT/MRCI.

4.4 Conclusions

We have shown that NOCI may be used to calculate excitation energies for double excitations in conjugated systems. Although the excitation energies presented in this work were not quantitative, we believe this method shows promise for future use in this direction. NOCI scales favorably compared to many other multireference methods and could be applied to systems even larger than those presented here. We applied a new spin-purification scheme resulting in better $\langle S^2 \rangle$ values and excitation energies for both the ground and excited states. NOCI also shows promise where orbital relaxation may be important such as singlet-triplet gaps in transition metal systems. We also feel this method could be applied to excited states with charge transfer character as the relaxation of the orbitals would allow for charge redistribution after "excitation".

Further developments and generalizations of NOCI are possible in many directions. Currently, the most unsatisfactory portion of NOCI, as it was used in this study, is the selection of basis states by human input and can lead to biasing of the results. This is only exacerbated by the reliance of this procedure on the Maximum Overlap Method (MOM) which, because it involves a non-linear optimization can be difficult to converge to the correct determinants. A black-box method for selection of basis states and a reduced dependence on MOM is our next target of research and progress is already underway in this direction. In this work, we used GHF determinants for spin-purification, but one could also search for non-collinear GHF determinants to provide more basis states. As a wavefunction based CI theory, NOCI

would also benefit from many of the known routes to target an improved treatment of dynamic correlation, such as that used in CASPT2. Finally, we plan on implementing nuclear gradients in order to follow the potential energy surfaces of the excited states calculated above as well as orbital gradients, which would allow for an orbital optimized NOCI; very related to the resonating Hartree–Fock approach of Fukutome[244].

Chapter 5

Automatic Generation of Basis States for NOCI

5.1 Introduction

Molecular excited states play an important role in many areas of physics and chemistry such as photosynthesis, solar energy conversion, and spectroscopy, and therefore theoretically modeling these electronic excited states is very important. This is challenging because many of the methods developed to treat excited states either fail to capture excitations of a specific character (multielectron excitations, Rydberg states, and charge transfer states) or are too computationally expensive to treat large systems. Time Dependent Density Functional Theory[187, 188] (TDDFT) is, by far, the most widely used excited state model, but fails to properly treat Rydberg excitations and, at least in its most widely used form, is unable to treat multielectron excitations.[189, 190] The equation-of-motion coupled-cluster (EOM-CC) formalism[194] provides a formal theory to treat all multielectron excited states but due to truncation may provide an unbalanced treatment of those states.[197] On top of this, even with truncation, EOM-CC and cheaper models based on these theories (CIS(D),CC2) have polynomial scaling $\mathcal{O}(N^5)$ or greater, which is typically too steep for large applications. The spin-flip family of methods[58–63, 199] use a high spin reference and employ linear combinations of spin-flipping excitations ($\alpha \rightarrow \beta$) to access states with the desired M_s value, such as the ground state or doubly excited states. The complete active space self-consistent-field (CASSCF)[64] and its second-order perturbation-corrected variant (CASPT2) are multiconfigurational wavefunctions which can properly treat multielectron excitations. These methods exhibit exponential-scaling with active space size, which typically grows with molecular size, and therefore are limited to small to medium molecules.

In the previous chapter, we presented work showing how Non-orthogonal Configuration Interaction (NOCI) may be applied to treat the doubly excited states of the linear polyenes and β-carotene. In that work, we used a hand selected set of important configurations, henceforth called basis states, chosen using knowledge of the system from previous research[225,

233, 234, 238]. Here, we shall detail an algorithm which automates this process, utilizing information obtained from calculating the eigenvectors of the Hartree–Fock Hessian.[106]

The remainder of this article is organized as follows: 1) we present a brief overview of NOCI, 2) we describe our new algorithm for automating the selection of the basis states 3) we show that the new method reproduces the hand-picking method for the polyenes studied previously, 4) we test the automated method on a larger test set of Schreiber et al.[245] consisting of 28 molecules, and 5) we draw some conclusions about where NOCI should be applicable and discuss future prospects for the method.

5.2 Theory

The notation utilized in this work is as follows: NOCI wavefunctions: Φ; Slater determinants: Ψ with indices w, x to distinguish between different SCF solutions; Spatial Molecular Orbitals (MO): ψ; Spatial Atomic Orbitals (AO): ω; AO Indices: lower case Greek μ, ν...; Virtual MO indices: a, b; Occupied MO indices: i, j; Generic MO indices: l, k. Bold case is employed for matrices. We employ the Einstein summation convention and the tensor notation with both covariant (subscript) and contravariant (superscript) indices of Head-Gordon et al.[23]

Basics

Within NOCI, one builds and diagonalizes the Hamiltonian in a basis of Slater determinants, which we will call basis states, which are, in general non-orthogonal. The non-orthogonality of the basis states introduces an overlap metric, $\mathbf{S}$, into the traditional CI eigenvalue problem:

$$\mathbf{HD} = \mathbf{SDE} \tag{5.1}$$

where $\mathbf{H}$ is the Hamiltonian matrix, $\mathbf{D}$ are the expansion coefficients, and $\mathbf{E}$ is a diagonal matrix of the energies.

NOCI therefore requires the computation of the overlap and Hamiltonian between two generally non-orthogonal basis states; our method for this may be found in Chapter 4. The most important portion of our NOCI procedure is that we transform each pair of determinants into the corresponding orbital basis[215, 216], also known as Löwdin-Paired orbitals[217]. The corresponding orbitals are defined as those in which the occupied-occupied orbital overlap is diagonal with elements bound between zero and one.

$$^{wx}\mathbf{S} = {}^{w}\tilde{\mathbf{C}}^{t}\mathbf{S}_{AO}{}^{x}\tilde{\mathbf{C}} \tag{5.2}$$

$$^{wx}\mathbf{S}_{ij} = \delta_{ij}s_i \tag{5.3}$$

As in our previous work[246] we shall utilize our NOCI spin purification scheme which relies on using Generalized Hartree–Fock (GHF) determinants. We apply an AO based unitary rotation parameterized by an angle θ to the coefficient matrix which changes the direction of the S_z axis without changing the energy. The choice of $\theta = \frac{\pi}{2}$ transforms the α

component of each orbital into the β component of each orbital. These degenerate basis states provide a new set of overlap and Hamiltonian matrix elements with the other basis states in the expansion and provide more variational flexibility in the CI. In this work, we shall use a quadrature of n_q points equidistant between 0 and $\frac{\pi}{2}$ to allow spin-contaminated states to purify. In order to compute $\langle S^2 \rangle$ for a given state, we evaluate the $\langle S^2 \rangle$ matrix elements for each pair of GHF determinants and then use the eigenvectors of the CI diagonalization to calculate the value of a given state.

Automatic Basis State Selection

In order to obtain the basis states for a NOCI calculation, we begin by converging a point-group symmetric RHF solution. From this solution, we compute the K lowest eigenvectors of the orbital Hessian[106], which is closely related to both TDHF and RPA[247]. The Hessian may be computed by expanding the wavefunction to second order, with wavefunction coefficients, χ_i^a:

$$|\Psi\rangle = |\Psi_0\rangle + \sum_{ia} \chi_i^a |\Psi_i^a\rangle + \sum_{ia,jb} \chi_i^a \chi_j^b \left|\Psi_{ij}^{ab}\right\rangle + ... \tag{5.4}$$

and taking derivatives of the energy with respect to either orbital rotations or equivalently single occupied-virtual excitations:

$$\frac{\partial^2 E}{\partial \chi_i^a \partial \chi_j^b} = \sum_{ia,jb} \chi^{*a}_{\ i} \chi_j^b \left\langle \Psi_i^a \left| \mathbf{Q} \right| \Psi_j^b \right\rangle \tag{5.5}$$

$$+ \sum_{ia,jb} \left[\frac{1}{2} \chi_i^a \chi_j^b \left\langle \Psi_0 \left| \mathbf{Q} \right| \Psi_{ij}^{ab} \right\rangle \right. \tag{5.6}$$

$$\left. + \frac{1}{2} \chi^{*a}_{\ i} \chi^{*b}_{\ j} \left\langle \Psi_{ij}^{ab} \left| \mathbf{Q} \right| \Psi_0 \right\rangle \right] \tag{5.7}$$

$$\mathbf{Q} = H - \langle \Psi_0 | H | \Psi_0 \rangle \tag{5.8}$$

This can then be rewritten in matrix form as:

$$\mathbf{H} = \frac{1}{2} \begin{pmatrix} \chi \\ \chi^* \end{pmatrix}^\dagger \begin{pmatrix} \mathbf{A} & \mathbf{B} \\ \mathbf{B}^* & \mathbf{A}^* \end{pmatrix} \begin{pmatrix} \chi \\ \chi^* \end{pmatrix} \tag{5.9}$$

with:

$$A_{ia,jb} = \left\langle \Psi_i^a \left| \mathbf{Q} \right| \Psi_j^b \right\rangle = (\varepsilon_a - \varepsilon_i)\delta_{ij}^{ab} + \langle aj | ib \rangle \tag{5.10}$$

$$B_{ia,jb} = \left\langle \Psi_{ij}^{ab} \left| \mathbf{Q} \right| \Psi_0 \right\rangle = \langle ab | ij \rangle \tag{5.11}$$

If real molecular orbitals are used and spin integration is taken into account, this matrix problem may be blocked according to both the symmetry of the reference determinant

(R/U/GHF) and whether that symmetry is allowed to relax. The process of computing Hessian eigenvectors may be written as an iterative $\mathcal{O}(N^3)$ process,[248] which is the same as the original HF calculation, so we have not introduced a computational bottleneck.

Now that we have a set of K Hessian eigenvectors, we form the natural transition orbitals (NTOs)[249] for each vector. NTOs are formed by singular value decomposition (SVD):

$$\chi_{ai} = \mathbf{U}\sigma\mathbf{V}^t \tag{5.12}$$

$$\bar{\mathbf{C}}_{\text{occ}} = \mathbf{C}_{\text{occ}} * V \tag{5.13}$$

$$\bar{\mathbf{C}}_{\text{vir}} = \mathbf{C}_{\text{vir}} * U \tag{5.14}$$

The NTOs represent, in some sense, the "best" possible particle/hole picture of an excited states and the singular values (σ) represent their relative importance. We will therefore use the σ values to define an "active space" in terms of the NTOs. The conceptual underpinning is that the NTOs of the Hessian eigenvectors correspond to orbitals which form a set of excitations which are important, especially for describing low-lying excitations. This is similar to using the low energy excited states of a cheaper CI (CIS or CISD) to begin a more complicated MRCI procedure. Procedurally, if there is only one large σ, we substitute the occupied orbital of $\bar{\mathbf{C}}$ with the virtual orbital of $\bar{\mathbf{C}}$ in the α space corresponding to that singular value, creating an excited determinant we then save. We then perform a double excitation of the same orbitals in both spin spaces. If there are two large singular values, we form all occupations in a (4,4) active space of the four spin-orbitals corresponding to the two large singular values. This corresponds to FCI in this active space. However, it is important to note that in the next step we will be transforming these orbitals and thus the properties that FCI in a space implies will no longer be true.

These determinants, although "different" than the original set, still consist of orbitals which are orthogonal to the original set. Next we relax these orbitals, by treating them as unrestricted determinants and allowing them to optimize using the Maximum Overlap Method (MOM)[218] combined with the Direct Inversion of the Iterative Subspace (DIIS) extrapolation method[219, 220]. It is well known that these relaxed states provide approximations to excited states despite not being orthogonal to the ground state[110, 201, 218, 221–223]. As shown in our previous work, this relaxation can be very important, providing a 2 eV shift in the excitation energy for a doubly excited state of the linear polyenes. In this relaxation procedure, both valence and core orbitals are relaxed in the presence of the MOM enforced occupancy of what would be virtual orbitals. This mean-field level relaxation clearly cannot fully account for all correlations of the electrons. It is important to make the distinction between this SCF type relaxation, which is a basis state specific optimization, and the relaxation of a CASSCF[64] type wavefunction where all the orbitals are optimized in the presence of all the configurations included in the active space.

The nonlinear optimization required to relax the basis states may cause complications to arise. When optimizing, if the state converges back to a previously found solution or is unable to reach a convergence threshold in a reasonable number of cycles, that state is deleted from our list of saved solutions. There is no guarantee that each Hessian eigenvector will

provide unique sets of determinants, because multiple eigenvectors could produce similar sets of important orbitals. However, by eliminating solutions which have already been located, these linearly dependent basis states are automatically removed. Finally, after all the basis states are optimized, these solutions are used as the basis states for a NOCI calculation.

A development version of QCHEM 3.2[98] utilizing the Armadillo linear algebra library[224] was used for all calculations. All polyene data was calculated using the 6-31G*[165] atomic orbital basis with geometries having been optimized using the B3LYP functional[40] in the same basis. The data for the Schreiber test set was computed using the geometries and basis set (TZVP[250]) from that work.[245]

Identification of the Excitations

In the test set, excitations are labeled with the symmetry of their transitions. In NOCI, neither basis states nor the final wavefunction if formed from an incomplete determinantal basis must obey the symmetries of the exact wavefunction but both do retain approximate symmetries. In order to identify which excitations were being computed, we used two methods. First, we computed the transition dipole moments and oscillator strengths between the ground and excited states, which is easy to do (even between non-orthogonal determinants) because the dipole moment operator is a one-electron operator. Utilizing the generalized set of Slater–Condon rules, if there are no zeros in the overlap (s_i) of the corresponding orbital basis ($\tilde{\mathbf{C}}$), the dipole matrix element between two non-orthogonal GHF determinants is:

$$^{wx}\mu_\lambda = \tilde{S}\sum_i \frac{\left({}^w\tilde{\mathbf{C}}^t\mu_\lambda{}^x\tilde{\mathbf{C}}\right)_{ii}}{s_i} \quad \lambda = x, y, z \tag{5.15}$$

where $\tilde{S}$ is the reduced overlap $\tilde{S} = \prod_i s_i$ with $s_i \neq 0$. If there is one zero at position i then:

$$^{wx}\mu_\lambda = \tilde{S}({}^w\tilde{\mathbf{C}}_i)^t\mu_\lambda({}^x\tilde{\mathbf{C}})_i \tag{5.16}$$

If there are two zeros, then the dipole is also zero (one-electron operator). The matrix formed from these elements ($\mathbf{M}_\lambda$) is then combined with the NOCI eigenvectors ($\mathbf{U}$) and the transformation resulting from the overlap metric ($\mathbf{X}$) to form the transition dipole between the ground and an excited state, n:

$$\mu_\lambda^{n0} = \mathbf{U}_n^t\mathbf{X}^t\mathbf{M}_\lambda\mathbf{X}\mathbf{U}_0 \tag{5.17}$$

Finally, we then compute the oscillator strength for this transition:

$$f_{n0} = \frac{2}{3}\left|\vec{\mu}^{n0}\right|^2(E_n - E_0) \tag{5.18}$$

If the basis states used in a NOCI calculation had proper point group symmetry, then the symmetry of a given NOCI excited state could be deduced from the symmetry of the

basis states with significant weight. While in general, the basis states used in NOCI do not have point group symmetry, within the implementation discussed above, they do maintain an approximate symmetry. Thus, if we had a way to calculate this approximate symmetry, we could infer the symmetry of the NOCI excited states. In order to do this, we can relate the excited determinants to a determinant for which we know the symmetry. In our case, this will be the reference RHF determinant.

For a given excited determinant, x, we form the corresponding orbital basis with the reference RHF determinant and identify the orbitals ($^x\tilde{\mathbf{C}}_k$) with small overlap ($s_k < .01$), as those which are important for the transition. In order to relate these orbitals to the original RHF orbitals, we use the vectors:

$$S^{\text{occ}} = (^{\text{RHF}}\tilde{\mathbf{C}}_k)^t \mathbf{S}_{\text{AO}}\, ^{\text{RHF}}\mathbf{C}_{\text{occ}} \tag{5.19}$$

$$S^{\text{vir}} = (^{x}\tilde{\mathbf{C}}_k)^t \mathbf{S}_{\text{AO}}\, ^{\text{RHF}}\mathbf{C}_{\text{vir}} \tag{5.20}$$

where the index of the maximum value in S^{occ} corresponds to the hole (i) and the index of the maximum value in S^{vir} corresponds to the electron (a). Now that we have the RHF orbitals, approximately excited in a given determinant, we use the known orbital symmetries of the RHF determinant and the product table of the point group to compute the transition symmetry for that determinant. We use all the values discussed above $\vec{\mu}^{n0}$, f_{n0}, s_k, S_i^{occ}, S_a^{vir}, and the eigenvector weight to evaluate how close these symmetries represent the actual symmetry of the wavefunction.

5.3 Results

Comparison with Hand-Picked Determinants

As in the prior work, we use the linear polyenes as a testing ground for our automatic NOCI (aNOCI). In comparison to the previous work, in which the number of basis states was limited to 10 for all systems studied, here the number of basis states is determined automatically and is system dependent. For all systems studied in this work we will be using 10 eigenvectors of the Hessian to generate the basis states.

In Table 5.1, we compare the results of CIS, CASCI-MRMP, and both the hand-picked (NOCI) and the automatically generated (aNOCI) forms of NOCI with two values of quadrature $n_q = 2\&10$. In Figure 5.1, we highlight the trends of the results in Table 5.1 (excluding the $n_q = 2$ results) as the chain length increases. We have included CASCI-MRMP results[225], not to be directly compared with those calculated in this work, because they were obtained using different geometries and basis sets but rather to provide a benchmark for accurate results. The CI Singles (CIS) in Table 5.1 are calculated using the same geometry and basis set, in order to provide a comparison with methods which have similar scaling and expected accuracy.

As discussed previously, CIS when compared to CASCI-MRMP is unable to qualitatively reproduce the excitation energy of the 2^1A_g^- state, because of its double excitation character.

Table 5.1: Absolute ground state energies (a.u.), vertical excitation energies (eV), and $\langle S^2 \rangle$ shown in () for the all-*trans* polyenes $C_{2n}H_{2n+2}$ with $2 \leq n \leq 10$ from different theories. Here aNOCI is the automatically generated basis state NOCI.

n	State	CIS	NOCI ($n_q = 2$)	aNOCI ($n_q = 2$)	NOCI ($n_q = 10$)	aNOCI ($n_q = 10$)	CASCI-MRMP
2	$1^1A_g^-$		-154.93643 (0.00)	-154.96361 (0.00)	-154.93647 (0.00)	-154.96372 (0.00)	
	$1^1B_u^+$	6.79	7.63 (0.01)	8.23 (0.01)	7.61 (0.00)	8.21 (0.00)	6.21
	$2^1A_g^-$	9.24	6.72 (0.35)	6.89 (0.03)	6.63 (0.10)	6.87 (0.02)	6.31
3	$1^1A_g^-$		-231.81963 (0.00)	-231.83637 (0.01)	-231.81965 (0.00)	-231.83710 (0.00)	
	$1^1B_u^+$	5.69	6.57 (0.04)	6.72 (0.09)	6.51 (0.01)	6.62 (0.03)	5.25[2]
	$2^1A_g^-$	8.12	6.32 (0.29)	6.21 (0.20)	6.23 (0.08)	6.11 (0.07)	5.10
4	$1^1A_g^-$		-308.70398 (0.00)	-308.71519 (0.01)	-308.70398 (0.00)	-308.71606 (0.00)	
	$1^1B_u^+$	4.97	5.59 (0.07)	5.76 (0.10)	5.52 (0.02)	5.67 (0.03)	4.57
	$2^1A_g^-$	7.23	5.22 (0.48)	5.11 (0.24)	5.09 (0.14)	5.02 (0.07)	4.26
5	$1^1A_g^-$		-385.58980 (0.00)	-385.59900 (0.01)	-385.58982 (0.00)	-385.59980 (0.01)	
	$1^1B_u^+$	4.47	4.94 (0.09)	5.12 (0.11)	4.86 (0.03)	5.05 (0.06)	4.17
	$2^1A_g^-$	6.54	4.73 (0.53)	4.63 (0.29)	4.59 (0.16)	4.50 (0.15)	3.68
6	$1^1A_g^-$		-462.47573 (0.00)	-462.48352 (0.01)	-462.47575 (0.00)	-462.48432 (0.01)	
	$1^1B_u^+$	4.11	4.45 (0.12)	4.58 (0.18)	4.35 (0.03)	4.45 (0.07)	3.87
	$2^1A_g^-$	6.00	4.25 (0.67)	4.19 (0.44)	4.10 (0.21)	4.05 (0.14)	3.19
7	$1^1A_g^-$		-539.36198 (0.00)	-539.36895 (0.01)	-539.36201 (0.00)	-539.36980 (0.01)	
	$1^1B_u^+$	3.83	4.09 (0.14)	4.09 (0.19)	3.98 (0.04)	3.97 (0.09)	3.60
	$2^1A_g^-$	5.55	3.93 (0.78)	3.83 (0.64)	3.77 (0.25)	3.67 (0.21)	2.80
8	$1^1A_g^-$		-616.24832 (0.00)	-616.25389 (0.01)	-616.24837 (0.00)	-616.25473 (0.01)	
	$1^1B_u^+$	3.61	3.80 (0.17)	3.94 (0.22)	3.67 (0.05)	3.81 (0.08)	3.38
	$2^1A_g^-$	5.19	3.63 (0.92)	3.53 (0.77)	3.46 (0.33)	3.38 (0.27)	2.50
9	$1^1A_g^-$		-693.13482 (0.00)	-693.13985 (0.02)	-693.13488 (0.00)	-693.14068 (0.01)	
	$1^1B_u^+$	3.43	3.57 (0.21)	3.68 (0.27)	3.43 (0.06)	3.54 (0.10)	3.18
	$2^1A_g^-$	4.88	3.39 (1.07)	3.28 (1.00)	3.19 (0.37)	3.11 (0.37)	2.25
10	$1^1A_g^-$		-770.02148 (0.00)	-770.02456 (0.02)	-770.02157 (0.00)	-770.02508 (0.01)	
	$1^1B_u^+$	3.29	3.39 (0.24)	3.41 (0.35)	3.24 (0.07)	3.23 (0.14)	3.00
	$2^1A_g^-$	4.62	3.17 (1.25)	2.99 (1.48)	2.94 (0.48)	2.76 (0.59)	2.04

[1] Reference [234]. Basis set:Dunning "QZ3p" (Carbon:5s4p3d,Hydrogen:3s2p), Active Space: (4,8), Geometry: Experimental

[2] Reference [225]. Basis set: cc-pvDZ, Active Space: (10,10) Geometry: Møller-Plesset 2nd Order Perturbation Theory

Figure 5.1: Polyene singlet vertical excitation energies (eV), comparing the automatic NOCI results with hand-picked NOCI, CIS, and MRMP (highly accurate results). Solid lines: $1^1B_u^+$. Dashed lines: $2^1A_g^-$. Clearly the automatic and hand-picked results are quite similar.

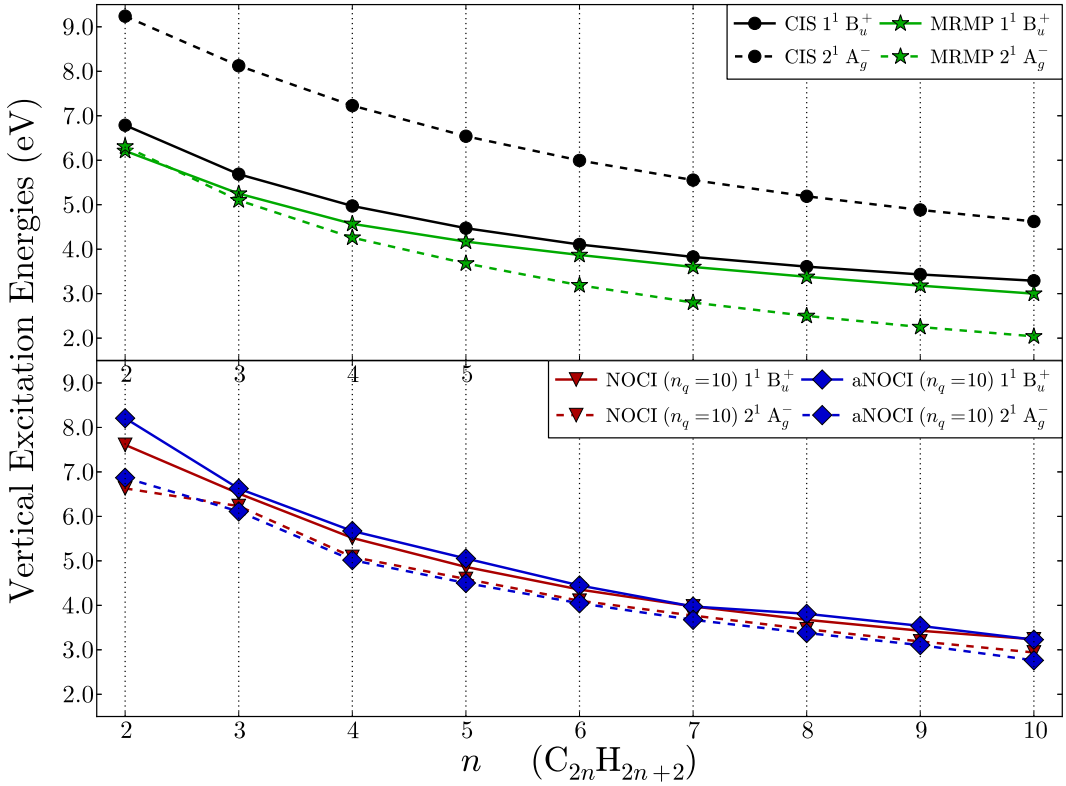

CIS places the $2^1A_g^-$ state well above the $1^1B_u^+$ state for all systems studied even though in the benchmark data the two states cross at hexatriene ($n = 3$). The wavefunction is also deficient; the two largest CIS amplitudes for the $2^1A_g^-$ state are HOMO-1 $\rightarrow$ LUMO and HOMO $\rightarrow$ LUMO+1 which are of the correct symmetry but clearly do not have the character of a double excitation. This is in comparison to the true wavefunction which has large weight on the double excitation $\text{HOMO}^2 \rightarrow \text{LUMO}^2$. TDDFT would also have this same problem because it can only account for single excitations. On the other hand CIS treats the $1^1B_u^+$ state quite well, paralleling the CASCI-MRMP results.

If we compare either NOCI method to CIS, we clearly see a marked improvement in the the excitation energy of the $2^1A_g^-$ states, up to a whole 2 eV change. We do also see a difference in the $1^1B_u^+$ state in the opposite direction this is primarily due to the lack of dynamic correlation in our model; as even in the automatic generation we are not including

that many states.

Comparing the results of the automatic NOCI and the hand-picked NOCI, the mean absolute errors are 0.16 eV and 0.11 eV for the $1^1B_u^+$ and $2^1A_g^-$ states respectively for $n_q = 10$ and 0.17 eV and 0.12 eV for $n_q = 2$. For these systems, the automatic generation was able to select states important for these excitations without any user input other than the number of Hessian eigenvectors.

5.4 Excited State Test Set

In order to test our automatic NOCI on a large number of systems, we applied the method to the 28 small to medium-sized organic molecules benchmark of Schreiber et al.[245]. For the polyenes we saw little change in excitation energy for the spin purification scheme and therefore we have only computed the benchmark data at $n_q = 2$. This set includes the most important classes of organic chromophores, unsaturated aliphatic hydrocarbons, aromatic hydrocarbons and heterocycles, carbonyl molecules (aldehydes, ketones, and amides) and nucleobases. The excited states are primarily of singlet valence character, although there are some Rydberg states and a few doubly excited valance states. Reference [245], includes singlet and triplet energies calculated by CASPT2, CC2, CCSD, and CC3 although here we only compare with the singlet energies. By comparing to experiment and using known disadvantages of the methods, Schreiber et al. make a decision about which energies are reliable and they call these the "Best" estimates. In this work we shall only compare with these best estimates although in the future it may be beneficial to do a comparison with each method in turn. As a note, the benchmark set does include three of the polyenes discussed in the previous section, butadiene, hexatriene, and octatetraene but these have been completely recalculated so as to take into account geometry and basis set differences. This benchmark was also recently used by Liu and Subotnik[251] and we will compare with the results of CIS and Variationally Orbital-Adapted Configuration Interaction Singles method (VOA-CIS). In Table 5.2 we compare all the methods listed above where "—" indicates the method was unable to find a state of that character.

Table 5.2: Comparison of NOCI vertical excitation energies (eV) with results from other methods.

Name	State	CASPT2	CASPT2	CC2	CCSD	CC3	Best[1]	VOA-CIS[2]	CIS	NOCI
Ethene	1^1B_{1u} $(\pi \rightarrow \pi^*)$	7.98	8.62	8.40	8.51	8.37	7.80	7.64	8.01	8.42
Butadiene	1^1B_u $(\pi \rightarrow \pi^*)$	6.23	6.47	6.49	6.72	6.58	6.18	5.90	6.44	7.42
	2^1A_g $(\pi \rightarrow \pi^*)$	6.27	6.83	7.63	7.42	6.77	6.55	7.76	9.22	6.66
Hexatriene	1^1B_u $(\pi \rightarrow \pi^*)$	5.01	5.31	5.41	5.72	5.58	5.10	4.96	5.47	6.34
	2^1A_g $(\pi \rightarrow \pi^*)$	5.20	5.42	6.67	6.61	5.72	5.09	6.92	8.24	6.02
Octatetraene	2^1A_g $(\pi \rightarrow \pi^*)$	4.38	4.64	5.87	5.99	4.97	4.47	6.32	7.50	4.94
	1^1B_u $(\pi \rightarrow \pi^*)$	4.42	4.70	4.72	5.07	4.94	4.66	4.19	4.83	5.40

Table 5.2: (continued)

Name	State	CASPT2	CASPT2	CC2	CCSD	CC3	Best[1]	VOA-CIS[2]	CIS	NOCI
Cyclopropene	1^1B_1 ($\sigma \rightarrow \pi^*$)	6.36	6.76	6.96	6.96	6.90	6.76	6.21	7.34	8.29
	1^1B_2 ($\pi \rightarrow \pi^*$)	7.45	7.06	7.17	7.24	7.10	7.06	6.59	6.92	6.62
Cyclopentadiene	1^1B_2 ($\pi \rightarrow \pi^*$)	5.27	5.51	5.69	5.87	5.73	5.55	5.09	5.54	8.49
	2^1A_1 ($\pi \rightarrow \pi^*$)	6.31	6.31	7.05	7.05	6.61	6.31	7.49	8.42	6.65
	3^1A_1 ($\pi \rightarrow \pi^*$)	7.89	8.52	8.86	8.95	6.69	—	8.86	8.92	—
Norbornadiene	1^1A_2 ($\pi \rightarrow \pi^*$)	5.28	5.34	5.57	5.80	5.64	5.34	5.18	5.67	6.21
	1^1B_2 ($\pi \rightarrow \pi^*$)	6.20	6.11	6.37	6.69	6.49	6.11	6.50	7.25	7.76
	2^1B_2 ($\pi \rightarrow \pi^*$)	6.48	7.32	7.65	7.87	7.64	—	7.70	8.04	8.88
	2^1A_2 ($\pi \rightarrow \pi^*$)	7.36	7.44	7.66	7.87	7.71	—	7.57	8.27	8.51
Benzene	1^1B_{2u} ($\pi \rightarrow \pi^*$)	4.84	5.05	5.27	5.19	5.07	5.08	—	—	5.65
	1^1B_{1u} ($\pi \rightarrow \pi^*$)	6.30	6.45	6.68	6.74	6.68	6.54	4.99	6.10	7.64
	1^1E_{1u} ($\pi \rightarrow \pi^*$)	7.03	7.07	7.44	7.65	7.45	7.13	—	—	8.48
	2^1E_{2g} ($\pi \rightarrow \pi^*$)	7.90	8.21	9.03	9.21	8.43	8.41	—	—	—
Naphthalene	1^1B_{3u} ($\pi \rightarrow \pi^*$)	4.03	4.24	4.45	4.41	4.27	4.24	4.70	5.24	5.20
	1^1B_{2u} ($\pi \rightarrow \pi^*$)	4.56	4.77	4.96	5.21	5.03	4.77	4.50	5.09	6.11
	2^1A_g ($\pi \rightarrow \pi^*$)	5.39	5.90	6.22	6.23	5.98	5.90	6.96	7.34	6.64
	1^1B_{1g} ($\pi \rightarrow \pi^*$)	5.53	6.00	6.21	6.53	6.07	6.00	6.42	6.77	7.32
	2^1B_{3u} ($\pi \rightarrow \pi^*$)	5.54	6.07	6.25	6.55	6.33	6.07	6.44	7.08	7.51
	2^1B_{1g} ($\pi \rightarrow \pi^*$)	5.87	6.48	6.82	6.97	6.79	6.48	—	—	8.31
	2^1B_{2u} ($\pi \rightarrow \pi^*$)	5.93	6.33	6.57	6.77	6.57	6.33	6.72	7.27	8.24
	3^1A_g ($\pi \rightarrow \pi^*$)	6.04	6.71	7.34	7.77	6.90	6.71	—	—	8.05
	3^1B_{2u} ($\pi \rightarrow \pi^*$)	7.16	8.18	8.46	8.77	8.44	—	—	—	10.64
	3^1B_{3u} ($\pi \rightarrow \pi^*$)	7.18	7.76	8.85	9.03	8.12	—	—	—	11.89
Furan	1^1B_2 ($\pi \rightarrow \pi^*$)	6.04	6.43	6.75	6.80	6.60	6.32	6.26	6.53	8.58
	2^1A_1 ($\pi \rightarrow \pi^*$)	6.16	6.52	6.87	6.89	6.62	6.57	6.57	8.16	6.57
	3^1A_1 ($\pi \rightarrow \pi^*$)	7.66	8.22	8.78	8.83	8.53	8.13	8.97	9.15	9.72
Pyrrole	2^1A_1 ($\pi \rightarrow \pi^*$)	5.92	6.31	6.61	6.61	6.40	6.37	6.43	7.65	6.28
	1^1B_2 ($\pi \rightarrow \pi^*$)	6.00	6.33	6.83	6.87	6.71	6.57	6.70	6.78	6.74
	3^1A_1 ($\pi \rightarrow \pi^*$)	7.46	8.17	8.44	8.44	8.17	7.91	8.63	8.89	9.20
Imidazole	$1^1A''$ ($n \rightarrow \pi^*$)	6.52	6.81	6.86	7.01	6.82	6.81	6.23	7.21	6.34
	$2^1A'$ ($\pi \rightarrow \pi^*$)	6.72	6.19	6.73	6.80	6.58	6.19	6.52	7.07	6.38
	$3^1A'$ ($\pi \rightarrow \pi^*$)	7.15	6.93	7.28	7.27	7.10	6.93	7.15	7.96	7.87
	$2^1A''$ ($\pi \rightarrow \pi^*$)	7.56	7.91	8.00	8.15	7.93	—	6.79	7.90	7.94
	$4^1A'$ ($\pi \rightarrow \pi^*$)	8.51	8.15	8.62	8.70	8.45	—	8.78	9.33	9.59
Pyridine	1^1B_2 ($\pi \rightarrow \pi^*$)	4.84	5.02	5.32	5.27	5.15	4.85	5.48	6.19	4.97
	1^1B_1 ($n \rightarrow \pi^*$)	4.91	5.14	5.12	5.25	5.05	4.59	5.44	6.13	5.49
	2^1A_2 ($n \rightarrow \pi^*$)	5.17	5.47	5.39	5.73	5.50	5.11	8.08	8.61	6.06
	2^1A_1 ($\pi \rightarrow \pi^*$)	6.42	6.39	6.88	6.94	6.85	6.26	6.68	6.51	7.41
	3^1A_1 ($\pi \rightarrow \pi^*$)	7.23	7.46	7.72	7.94	7.70	7.18	7.99	8.42	9.10
	2^1B_2 ($\pi \rightarrow \pi^*$)	7.48	7.29	7.61	7.81	7.59	7.27	7.86	8.44	8.83
	4^1A_1 ($\pi \rightarrow \pi^*$)	7.96	8.70	9.00	9.45	8.68	—	—	—	11.92
	3^1B_2 ($\pi \rightarrow \pi^*$)	7.95	8.62	9.37	9.64	8.77	—	—	—	9.42
Pyrazine	1^1B_{3u} ($n \rightarrow \pi^*$)	3.63	4.12	4.26	4.42	4.24	3.95	4.01	5.13	5.03
	1^1A_u ($n \rightarrow \pi^*$)	4.52	4.70	4.95	5.29	5.05	4.81	4.92	7.03	7.35
	1^1B_{2u} ($\pi \rightarrow \pi^*$)	4.75	4.85	5.13	5.14	5.02	4.64	4.76	5.98	8.32
	1^1B_{2g} ($n \rightarrow \pi^*$)	5.17	5.68	5.92	6.02	5.74	5.56	5.35	6.70	9.53

Table 5.2: (continued)

Name	State	CASPT2	CASPT2	CC2	CCSD	CC3	Best[1]	VOA-CIS[2]	CIS	NOCI
	1^1B_{1g} $(n \rightarrow \pi^*)$	6.13	6.41	6.70	7.13	6.75	6.60	6.58	9.81	8.72
	1^1B_{1u} $(\pi \rightarrow \pi^*)$	6.70	6.89	7.10	7.18	7.07	6.58	6.37	6.65	6.26
	2^1B_{1u} $(\pi \rightarrow \pi^*)$	7.57	7.79	8.13	8.34	8.06	7.72	7.80	8.75	9.93
	2^1B_{2u} $(\pi \rightarrow \pi^*)$	7.70	7.65	8.07	8.29	8.05	7.60	7.85	9.07	10.44
	1^1B_{3g} $(\pi \rightarrow \pi^*)$	8.19	8.47	9.42	9.75	8.77	—	—	—	—
	2^1A_g $(\pi \rightarrow \pi^*)$	8.26	8.61	9.26	9.55	8.69	—	—	—	—
Pyrimidine	1^1B_1 $(n \rightarrow \pi^*)$	3.81	4.44	4.49	4.70	4.50	4.55	4.88	5.87	5.66
	1^1A_2 $(n \rightarrow \pi^*)$	4.12	4.81	4.84	5.12	4.93	4.91	5.52	6.56	6.31
	1^1B_2 $(\pi \rightarrow \pi^*)$	4.93	5.24	5.51	5.49	5.36	5.44	5.87	6.50	5.58
	2^1A_1 $(\pi \rightarrow \pi^*)$	6.72	6.64	7.12	7.17	7.06	6.95	7.15	6.90	7.83
	2^1B_2 $(\pi \rightarrow \pi^*)$	7.32	7.64	8.08	8.24	8.01	—	8.48	8.88	8.34
	3^1A_1 $(\pi \rightarrow \pi^*)$	7.57	7.21	7.79	7.97	7.74	—	8.06	8.61	9.29
Pyridazine	1^1B_1 $(n \rightarrow \pi^*)$	3.48	3.78	3.90	4.11	3.92	3.78	3.59	4.91	—
	1^1A_2 $(n \rightarrow \pi^*)$	3.66	4.32	4.40	4.76	4.49	4.32	4.78	6.10	5.81
	2^1A_1 $(\pi \rightarrow \pi^*)$	4.86	5.18	5.37	5.35	5.22	5.18	5.24	6.32	6.03
	2^1A_2 $(n \rightarrow \pi^*)$	5.09	5.77	5.81	6.00	5.74	5.77	5.61	7.29	7.13
	2^1B_1 $(n \rightarrow \pi^*)$	5.80	6.52	6.40	6.70	6.41	—	7.00	8.43	—
	1^1B_2 $(\pi \rightarrow \pi^*)$	6.61	6.31	7.00	7.09	6.93	—	6.34	6.56	5.24
	2^1B_2 $(\pi \rightarrow \pi^*)$	7.39	7.29	7.57	7.79	7.55	—	7.43	8.32	7.88
	3^1A_1 $(\pi \rightarrow \pi^*)$	7.50	7.62	7.90	8.11	7.82	—	7.83	8.67	9.18
Triazine	$1^1A_1'$' $(n \rightarrow \pi^*)$	3.90	4.60	4.70	4.96	4.78	4.60	—	6.34	5.24
	$1^1A_2'$' $(n \rightarrow \pi^*)$	4.08	4.68	4.80	4.98	4.76	4.66	—	6.45	5.57
	$1^1E''$ $(n \rightarrow \pi^*)$	4.36	4.71	4.77	5.01	4.81	4.71	—	6.45	5.91
	$1^1A_2'$ $(\pi \rightarrow \pi^*)$	5.33	5.79	5.82	5.84	5.71	5.79	—	7.02	6.04
	$2^1A_2'$ $(\pi \rightarrow \pi^*)$	6.77	7.25	7.52	7.51	7.41	—	—	—	—
	$2^1E''$ $(n \rightarrow \pi^*)$	7.15	7.72	8.04	8.19	7.80	—	—	—	—
	$1^1E'$ $(\pi \rightarrow \pi^*)$	8.16	7.49	8.06	6.28	8.04	—	—	—	—
	$2^1E'$ $(\pi \rightarrow \pi^*)$	8.03	8.99	9.93	10.24	9.44	—	—	—	—
Tetrazine	1^1B_{3u} $(n \rightarrow \pi^*)$	1.96	2.24	2.47	2.71	2.53	2.24	1.83	3.52	4.34
	1^1A_u $(\pi \rightarrow \pi^*)$	3.06	3.48	3.67	4.07	3.79	3.48	3.61	5.67	6.49
	1^1B_{1g} $(n \rightarrow \pi^*)$	4.51	4.73	5.10	5.32	4.97	4.73	4.53	6.08	9.07
	1^1B_{2u} $(\pi \rightarrow \pi^*)$	4.89	4.91	5.20	5.27	5.12	4.91	4.76	6.24	6.09
	1^1B_{2g} $(n \rightarrow \pi^*)$	5.05	5.18	5.53	5.70	5.34	5.18	4.72	6.56	7.67
	1^1B_{3g} $(n, n \rightarrow \pi^*, \pi^*)$	5.16	5.79	—	—	—	5.79	—	—	—
	2^1A_u $(n \rightarrow \pi^*)$	5.28	5.47	5.50	5.70	5.46	5.47	5.12	6.65	7.39
	2^1B_{2g} $(n \rightarrow \pi^*)$	5.48	6.07	6.32	6.76	6.23	—	6.12	9.36	9.97
	2^1B_{1g} $(n \rightarrow \pi^*)$	5.99	6.38	6.91	7.25	6.87	—	6.77	9.79	9.73
	3^1B_{1g} $(n \rightarrow \pi^*)$	6.20	6.74	7.64	8.36	7.08	—	—	—	11.90
	2^1B_{3u} $(n \rightarrow \pi^*)$	6.37	6.77	6.70	6.99	6.67	—	6.97	8.68	—
	1^1B_{1u} $(\pi \rightarrow \pi^*)$	7.13	6.96	7.60	7.66	7.45	—	6.52	6.88	—
	2^1B_{1u} $(\pi \rightarrow \pi^*)$	7.54	7.43	7.75	8.06	7.79	—	7.28	8.58	—
	2^1B_{2u} $(\pi \rightarrow \pi^*)$	7.94	8.15	8.65	8.88	8.51	—	8.35	9.53	—
	2^1B_{3g} $(\pi \rightarrow \pi^*)$	8.12	8.32	8.97	9.44	8.47	—	—	—	—
Formaldehyde	1^1A_2 $(n \rightarrow \pi^*)$	3.91	3.98	4.09	3.97	3.95	3.88	2.93	4.46	3.43
	1^1B_1 $(\sigma \rightarrow \pi^*)$	9.09	9.14	9.35	9.26	9.18	9.10	9.04	9.62	8.32
	2^1A_1 $(\pi \rightarrow \pi^*)$	9.77	9.31	10.34	10.54	10.45	9.30	9.05	9.67	9.58
Acetone	1^1A_2 $(n \rightarrow \pi^*)$	4.18	4.42	4.52	4.43	4.40	4.40	3.78	5.10	3.66
	1^1B_1 $(\sigma \rightarrow \pi^*)$	9.10	9.27	9.29	9.26	9.17	9.10	9.31	9.77	7.36

Table 5.2: (continued)

Name	State	CASPT2	CASPT2	CC2	CCSD	CC3	Best[1]	VOA-CIS[2]	CIS	NOCI
	2^1A_1 $(\pi \rightarrow \pi^*)$	9.16	9.31	9.74	9.87	9.65	9.40	8.89	9.69	9.17
Benzoquinone	1^1A_u $(n \rightarrow \pi^*)$	2.50	2.80	2.92	3.19	2.85	2.80	—	4.16	4.72
	1^1B_{1g} $(n \rightarrow \pi^*)$	2.50	2.78	2.81	3.07	2.75	2.78	—	5.08	4.19
	1^1B_{3g} $(\pi \rightarrow \pi^*)$	4.19	4.25	4.69	4.93	4.59	4.25	—	4.00	4.69
	1^1B_{1u} $(\pi \rightarrow \pi^*)$	5.15	5.29	5.59	5.89	5.62	5.29	—	8.31	8.49
	1^1B_{3u} $(n \rightarrow \pi^*)$	5.15	5.60	5.69	6.55	5.82	5.60	—	6.31	6.90
	2^1B_{3g} $(\pi \rightarrow \pi^*)$	6.34	6.98	7.36	7.62	7.27	6.98	—	9.05	9.20
	2^1B_{1u} $(\pi \rightarrow \pi^*)$	7.08	7.91	8.31	8.47	7.82	—	—	—	8.49
Formamide	$1^1A''$ $(n \rightarrow \pi^*)$	5.61	5.63	5.76	5.66	5.65	5.63	5.25	6.42	4.68
	$2^1A'$ $(\pi \rightarrow \pi^*)$	7.41	7.44	8.15	4.52	8.27	7.44	6.84	8.82	7.17
	$3^1A'$ $(\pi \rightarrow \pi^*)$	10.50	10.54	11.24	11.34	10.93	—	8.37	10.57	8.12
Acetamide	$1^1A''$ $(n \rightarrow \pi^*)$	5.54	5.80	5.77	5.71	5.69	5.80	5.26	6.58	4.71
	$2^1A'$ $(\pi \rightarrow \pi^*)$	7.21	7.27	7.66	7.85	7.67	7.27	7.07	9.02	6.83
	$3^1A'$ $(\pi \rightarrow \pi^*)$	10.08	10.09	10.71	10.77	10.50	—	7.65	9.86	7.95
Propanamide	$1^1A''$ $(n \rightarrow \pi^*)$	5.48	5.72	5.78	5.74	5.72	5.72	5.20	6.62	4.72
	$2^1A''$ $(\pi \rightarrow \pi^*)$	7.28	7.20	7.56	7.80	7.62	7.20	7.22	9.00	6.71
	$3^1A'$ $(\pi \rightarrow \pi^*)$	9.95	9.94	10.33	10.34	10.06	—	7.73	9.82	6.89
Cytosine	$2^1A'$ $(\pi \rightarrow \pi^*)$	4.39	4.68	4.80	4.98	—	4.66	5.26	6.07	4.88
	$1^1A''$ $(n \rightarrow \pi^*)$	5.00	5.12	5.13	5.45	—	4.87	5.39	6.85	4.66
	$2^1A''$ $(n \rightarrow \pi^*)$	6.53	5.54	5.01	5.99	—	5.26	5.59	7.21	6.40
	$3^1A'$ $(\pi \rightarrow \pi^*)$	5.36	5.54	5.71	5.95	—	5.62	6.21	7.45	7.49
	$4^1A'$ $(\pi \rightarrow \pi^*)$	6.16	6.40	6.65	6.81	—	—	7.30	7.99	8.12
	$5^1A'$ $(\pi \rightarrow \pi^*)$	6.74	6.98	6.94	7.23	—	—	7.82	9.04	—
	$6^1A'$ $(\pi \rightarrow \pi^*)$	7.61	8.23	8.45	8.69	—	—	—	—	—
Thymine	$1^1A''$ $(n \rightarrow \pi^*)$	4.39	4.94	4.94	5.14	—	4.82	4.80	6.23	4.08
	$2^1A'$ $(\pi \rightarrow \pi^*)$	4.88	5.06	5.39	5.60	—	5.20	5.88	6.31	6.25
	$3^1A'$ $(\pi \rightarrow \pi^*)$	5.88	6.15	6.46	6.78	—	6.27	7.17	8.24	7.07
	$2^1A''$ $(n \rightarrow \pi^*)$	5.91	6.38	6.33	6.57	—	6.16	6.12	7.67	5.76
	$4^1A'$ $(\pi \rightarrow \pi^*)$	6.10	6.52	6.80	7.05	—	6.53	7.45	8.65	7.64
	$4^1A''$ $(n \rightarrow \pi^*)$	6.15	6.86	6.73	7.67	—	—	8.09	8.88	8.18
	$5^1A''$ $(n \rightarrow \pi^*)$	6.70	7.43	7.18	7.87	—	—	8.15	8.58	8.45
	$5^1A'$ $(\pi \rightarrow \pi^*)$	7.13	7.43	7.71	7.90	—	—	8.63	9.59	8.23
Uracil	$1^1A''$ $(n \rightarrow \pi^*)$	4.54	4.90	4.91	5.11	—	4.80	4.81	6.22	3.97
	$2^1A'$ $(\pi \rightarrow \pi^*)$	5.00	5.23	5.52	5.70	—	5.35	6.03	6.49	6.08
	$3^1A'$ $(\pi \rightarrow \pi^*)$	5.82	6.15	6.43	6.76	—	6.26	7.16	8.36	6.82
	$2^1A''$ $(n \rightarrow \pi^*)$	6.00	6.27	6.73	7.68	—	6.10	6.09	7.61	5.63
	$3^1A''$ $(n \rightarrow \pi^*)$	6.37	6.97	6.26	6.50	—	6.56	7.13	7.82	8.36
	$4^1A'$ $(\pi \rightarrow \pi^*)$	6.46	6.75	6.96	7.19	—	6.70	7.58	8.76	7.93
	$5^1A''$ $(n \rightarrow \pi^*)$	6.95	7.28	7.12	7.74	—	—	8.83	9.33	8.75
	$5^1A'$ $(\pi \rightarrow \pi^*)$	7.00	7.42	7.66	7.81	—	—	8.48	9.47	8.79
Adenine	$2^1A'$ $(\pi \rightarrow \pi^*)$	5.13	5.20	5.28	5.37	—	5.25	5.76	6.23	5.74
	$3^1A'$ $(\pi \rightarrow \pi^*)$	5.20	5.30	5.42	5.61	—	5.25	5.89	6.37	6.32
	$1^1A''$ $(n \rightarrow \pi^*)$	6.15	5.21	5.27	5.58	—	5.12	5.80	7.05	5.56
	$2^1A''$ $(n \rightarrow \pi^*)$	6.86	5.97	5.91	6.19	—	5.75	6.78	7.50	5.73
	$4^1A'$ $(\pi \rightarrow \pi^*)$	6.24	6.35	6.58	6.83	—	—	7.28	7.69	6.48
	$5^1A'$ $(\pi \rightarrow \pi^*)$	6.72	6.64	6.93	7.17	—	—	7.55	8.16	—
	$6^1A'$ $(\pi \rightarrow \pi^*)$	6.99	6.88	7.49	7.72	—	—	8.01	8.37	—
	$7^1A'$ $(\pi \rightarrow \pi^*)$	7.57	7.56	8.04	8.47	—	—	—	—	—

Table 5.2: (continued)

Name	State	CASPT2	CASPT2	CC2	CCSD	CC3	Best[1]	VOA-CIS[2]	CIS	NOCI

[1] Benchmark molecules and reference data from Reference [245].
[2] CIS and VOA-CIS data taken from Reference [251].

In order to compare our data quantitatively with the benchmark data we adopt the same errors as Liu and Subotnik. For a given molecule m there are n states and for each state there is an error:

$$\mathrm{Err}_{m,j} = E^{\mathrm{trial}}_{m,j} - E^{\mathrm{ref}}_{m,j} \qquad (j = 1, 2, ..., n) \tag{5.21}$$

and for each molecule m there is therefore an average absolute error:

$$\mathrm{Err}^{\mathrm{abs}}_{m} = \frac{\sum_{j=1}^{n_m} |\mathrm{Err}_{m,j}|}{n_m} \tag{5.22}$$

We also compute the relative error for each molecule:

$$\mathrm{Err}^{\mathrm{rel}}_{m} = \sqrt{\frac{\sum_{j,i=1}^{n_m} \left(\mathrm{Err}_{m,i} - \mathrm{Err}_{m,j}\right)^2}{n_m^2}} \tag{5.23}$$

We use a denominator of n_m^2 instead of the standard variance $n_m(n_m - 1)$ because n_m can be 1. Clearly, the relative error for a certain molecule will be zero if the excitations are different by a constant shift. Both the absolute and relative errors described above are per molecule errors and thus we can average these errors over all the molecules($\mathrm{Err}^{\mathrm{abs/rel}}_{\mathrm{mol}}$). For absolute error, it is also possible to ignore which molecule the excitation came from and just average over all excitations ($\mathrm{Err}^{\mathrm{abs}}_{\mathrm{total}}$). In Table 5.3, we have computed these three aggregate errors for all the columns in Table 5.2.

From this table it is apparent that NOCI with the automated procedure has roughly the same errors as CIS with slightly lower aggregate absolute errors and a slightly higher relative error. CIS consistently overestimates excitation energies, a positive aspect of the method, where as NOCI under and overestimates them, which explains why it has larger relative error.

In Figure 5.2 we show both absolute and relative errors for NOCI and for CIS in comparison to the "Best" estimates of Schreiber et al.. As one can see the errors between CIS and NOCI look comparable except for a two systems (pyrazine and tetrazine) which have absolute errors above 2 eV. These large errors seem to be primarily in the systems with $n \rightarrow \pi^*$ type transitions for which the accuracy of NOCI requires further assessment. It is possible that for these systems the excited states are being overcorrelated with respect to the ground state as is seen in CISD.

CIS includes many more states than NOCI and thus one would expect the errors in CIS and NOCI to be comparable for single excitations. For double excitations, which CIS can

Table 5.3: Aggregate errors (eV), as defined in the text, with respect to the "Best" column for all the methods included in Table 5.2.

Method	$\mathrm{Err}^{\mathrm{abs}}_{\mathrm{total}}$	$\mathrm{Err}^{\mathrm{abs}}_{\mathrm{mol}}$	$\mathrm{Err}^{\mathrm{rel}}_{\mathrm{mol}}$
CASPT2	0.32	0.29	0.25
CASPT2	0.10	0.11	0.08
CC2	0.30	0.34	0.27
CCSD	0.49	0.51	0.35
CC3	0.24	0.26	0.19
VOA-CIS	0.49	0.54	0.52
CIS	1.27	1.15	0.74
NOCI	1.18	1.03	0.81

Figure 5.2: Absolute (upper) and relative (lower) error in vertical excitation energies (eV), as defined in the text, with respect to the "Best" estimates from the benchmark set for each of the 28 molecules.

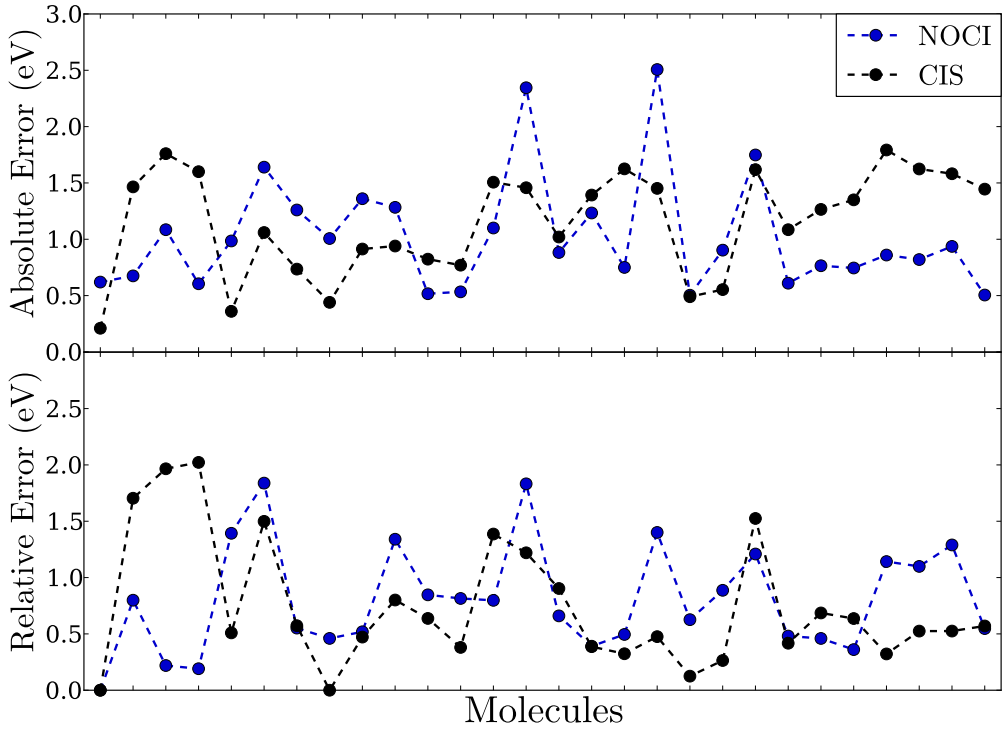

not accurately compute, one would expect NOCI to outperform CIS. The double excitations in the benchmark data may be identified by a low $\%T_1$ of either EOM-CCSD or CC3 theory. $\%T_1$ is a diagnostic which is the norm of coefficients of the singles excitations in the CC wavefunction. If we look at just the excitations from the benchmark data for which $\%T_1 < 75$ we will be looking at primarily double excitations. For these 5 excitations (the $2^1\mathrm{A}_g^-$ of butadiene, hexatriene and octatetraene, the $2^1\mathrm{E}_{2g}$ state of benzene, and the $3^1\mathrm{A}_g$ state of naphthalene), CIS was unable to find excitations of this character for both benzene and naphthalene. The average error in CIS for these states is 2.95 eV (3 states) and for NOCI is 0.71 eV (5 states). This is another example where NOCI shows strength computing double excitations.

5.5 Conclusions

We have detailed an approach for automatically generating the basis states for a NOCI calculation. Our method relies upon the utilizing the eigenvectors of the NOCI Hessian matrix to produce active spaces to generate new basis states. We have shown that this automatic NOCI performs well on the linear polyenes and is able to include doubly excited states. We have also tested this procedure on the benchmark data of Schreiber et al.[245] showing results at approximately the same error as CIS. Examining Table 5.3, it is clear that if one can computationally afford to run CC3 or CASPT2 one should do so, but when these methods are infeasible and double excitations play an important role NOCI may be a good option.

In the future, we will investigate possible adjustments of the automatic procedure to ameliorate some of the errors, with the aim of providing a more balanced treatment of the excitations. In this search for balance, it would be helpful to study the patterns of the energies of the states before and after MOM relaxations and their importance in the final wavefunctions. We will also be calculating the result of the NOCI spin purification scheme on the benchmark systems, but we expect little difference in error.

Further developments and generalizations of NOCI are possible in many directions. NOCI shows promise where orbital relaxation may be important such as singlet-triplet gaps in transition metal systems and charge transfer states. Applying the current theory, to these systems, leads to difficulties due to spin contamination and potentially would benefit from a reinterpretation of NOCI with a focus on spin purity and spin completeness. NOCI is a wavefunction based CI theory and thus would benefit from an improved treatment of dynamic correlation, such as that in CASPT2. Analytic nuclear gradients would allow one to follow the potential energy surface of the excited states.

Appendix A

Experimental and Calculated Data for Catalyst

Cyclic Voltammetry

Aqueous electrochemical experiments were conducted under a N_2 atmosphere in a 1.0 M buffered potassium acetate or phosphate solutions at ambient temperature and carried out using BASi's Epsilon potentiostat. All voltammetry experiments used a glassy carbon disk working electrode (3.0 mm diameter), a platinum wire counter electrode, and a Ag/AgCl reference electrode (BASi). All potentials were converted to SHE by adding 0.198 V to the measured potentials.

Crystal Structure Determination

The crystal was coated with Paratone-N oil, attached to a Kapton loop, transferred to a Siemens SMART APEX diffractometer, and cooled in a nitrogen stream. A full hemisphere of data was collected, and the unit-cell parameters were refined against all data. The crystal did not show significant decay during data collection. Data were integrated and corrected for Lorentz and polarization effects using SAINT 7.07b, and were corrected for absorption effects using SADABS 2.10. The space-group assignment was based upon systematic absences, E-statistics, agreement factors for equivalent reflections, and successful refinement of the structure. The structure was solved by direct methods and expanded through successive difference Fourier maps. It was refined against all data using the SHELXTL 5.0 software package. Hydrogen atoms were inserted at idealized positions and refined using a riding model with an isotropic thermal parameter 1.2 times that of the attached carbon atom (or 1.5 times for terminal methyl groups). Thermal parameters for all non-hydrogen atoms were refined anisotropically, except for the disordered atoms in the triflate counter ions and the acetonitrile molecules.

Table A.1: Crystallographic data[a] for $[(PY5Me_2)Mo(MeCN)](CF_3SO_3)_2 \cdot MeCN$

Identification code	hk216a
Empirical formula	$C_{73}H_{50}F_{12}Mo_2N_{16}O_{12}S_4$
Formula weight	1891.41
Temperature	100(2) K
Wavelength	1.54178Å
Crystal system, space group	Monoclinic, $P2_1/n$
Unit cell dimensions	$a = 12.4356(6)$ Å $\quad \alpha = 90°$
	$b = 15.7501(8)$ Å $\quad \beta = 90.681(2)°$
	$c = 20.2185(10)$ Å $\quad \gamma = 90°$
Volume	3959.8(3) Å^3
Z, Calculated density	2, 1.586 mg/m^3
Absorption coefficient	4.448 mm^{-1}
F(000)	1904
Crystal size	$0.35 \times 0.20 \times 0.18$ mm
Theta range for data collection	3.56 to 68.16°
Limiting indices	$-14 \leq h \leq 12, -16 \leq k \leq 18, -24 \leq l \leq 21$
Reflections collected / unique	26907 / 7239 [R_{int}= 0.0139]
Completeness to theta = 68.16	91.7%
Absorption correction	Empirical
Max. and min. transmission	0.7530 and 0.4802
Refinement method	Full-matrix least-squares on F^2
Data / restraints / parameters	6642 / 0 / 522
Goodness-of-fit on F^2	2.139
Final R indices [$I > 2$sigma(I)][b]	$R_1 = 0.0794$, $wR_2 = 0.3049$
R indices (all data)	$R_1 = 0.0816$, $wR_2 = 0.3253$
Largest diff. peak and hole	1.916 and -1.404e$^-$/Å^{-3}

[a] Obtained with HELIOS multilayer mirror monochromated Cu Kα ($\lambda = 1.5418$Å) radiation

[b] $R_1 = \sum ||F_o| - F_c|| / \sum |F_o|$, $wR_2 = \{\sum[w(F_o^2 - F_o^2)^2] / \sum[w(F_o^2)^2]\}^{1/2}$

Table A.2: Absolute energies with three functionals at the TZV-P/6-311G** basis of all species and $\Delta G^{\text{vib}}_{(T=298.15K)} = \Delta H_{\text{translation}} + \Delta H_{\text{rotational}} + \Delta H_{\text{vibrational}} - (298.15K) * (\Delta S_{\text{translation}} + \Delta S_{\text{rotational}} + \Delta S_{\text{vibrational}})$ (B3LYP/TZV-P/6-311G**) in Hartrees.

Species	**A**	**B**	**C**	
Multiplicity	1	2	2	4
B3LYP	-5,446.783781	-0.259024	-0.583680	-0.620252
BP86	-5,447.167265	-0.274416	-0.574846	-0.584205
ωB97	-5,446.712850	-0.235381	-0.585440	-0.621088
$\Delta G^{\text{vib}}_{(T=298.15K)}$	0.435545	0.432399	0.445109	0.445458

Species	**D**		**E**	
Multiplicity	1	3	1	3
B3LYP	-0.855330	-0.865037	-1.165465	-1.176327
BP86	-0.862506	-0.870186	-1.154347	-1.166211
ωB97	-0.836189	-0.848002	-1.164639	-1.174553
$\Delta G^{\text{vib}}_{(T=298.15K)}$	0.441349	0.443420	0.454983	0.452959

Species	**F**	**G**		H_2
Multiplicity	3	2	4	1
B3LYP	-1.166247	-1.003094	-0.979054	—
BP86	-1.140344	-1.026417	-0.998338	-1.177465
ωB97	-1.157474	-0.967223	-0.946157	—
$\Delta G^{\text{vib}}_{(T=298.15K)}$	0.455456	0.437805	0.436528	0.020908

Species	**H**		**I**	
Multiplicity	2	4	2	4
B3LYP	-1.431907	-1.396265	-1.423501	-1.396995
BP86	-1.442940	-1.401435	-1.431334	-1.403241
ωB97	-1.399619	-1.379520	-1.411031	-1.383765
$\Delta G^{\text{vib}}_{(T=298.15K)}$	0.452446	0.448278	0.453949	0.450067

Species	**J**	H_2O	**H** $\overset{\ddagger}{\rightarrow}$ **I**	**I** $\overset{\ddagger}{\rightarrow}$ **C**
Multiplicity	2	1	2	2
B3LYP	-1.740281	—	-1.791604	-1.778098
BP86	-1.736175	-76.447789	-1.408120	-1.394615
ωB97	-1.736108	—	-1.862535	-1.849030
$\Delta G^{\text{vib}}_{(T=298.15K)}$	0.458366	0.001867	0.449972	0.449405

Species	**I** + H_2O	**I** + H_2O $\overset{\ddagger}{\rightarrow}$ **C** + H_2O	**F** $\overset{\ddagger}{\rightarrow}$ **A**	**E** $\overset{\ddagger}{\rightarrow}$ **F**
Multiplicity	2	2	1	3
B3LYP	-78.278236	-78.247847	-1.509342	-1.492102
BP86	-77.894752	-77.864363	-1.125859	-1.108618
ωB97	-78.349167	-78.318778	-1.563033	-1.580273
$\Delta G^{\text{vib}}_{(T=298.15K)}$	0.474128	0.470645	0.453172	0.452786

Figure A.1: A crystal structure of $[(PY5Me_2)Mo(CH_3CN)]^{2+}$ in which an acetonitrile has displaced the triflate of $[(PY5Me_2)Mo(CF_3SO_3)]^{1+}$ demonstrating the lability of the triflate.

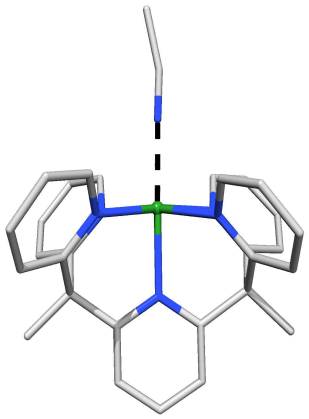

Table A.3: LOBA populations for **E** and **H**. **H** has an extra electron.

E	**H**
0.94, 0.89, 0.83, 0.67	0.91, 0.69, 0.73, 0.53, 0.55

LOBA

It is important to note that in the LOBA of **H** two orbitals in the β-space as shown in the article are below the threshold (0.60) used by Thom et al.[149] to define when to subtract one from the atomic number while calculating oxidation state. Despite the choice made in that paper, allowing 0.50 to be considered localized could also be justified from the thresholding done within the previous work. If 0.50 is chosen though a difficulty arises when analyzing **I** because in this case both bonding orbitals are greater than 0.5 and would be considered localized resulting in an oxidation state of +1 for the metal hydride. This is not to say that the analysis is broken but is more an indication of the fact that this method is quite new and needs to be used carefully with systems for which it was not previously applied.

Figure A.2: LOBA diagrams for species **A** and **B**. Each set of shapes (i.e. blue circles) represents a single molecular orbital. The y-axis is the LOBA population value for the atom given on the x-axis. For **A** three molecular orbitals are shared between Mo and O, in both the alpha (up spin) and beta (down spin) space; these are the 6 electrons making up the triple bond. For **B** one of the orbitals in the alpha space is missing thus 2.5 bond order. In both figures only orbitals involved in bonding are shown.

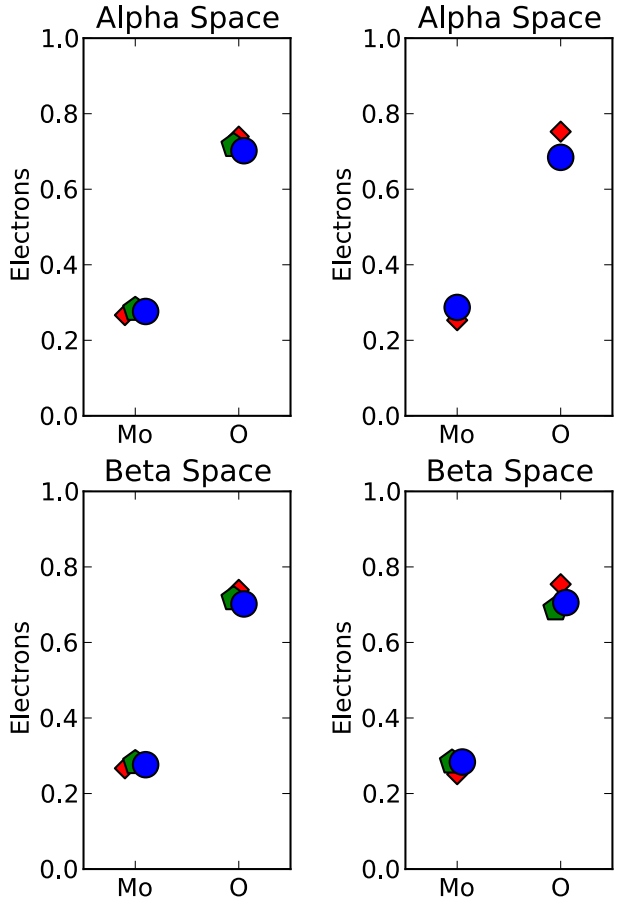

(a) **A** (b) **B**

Figure A.3: Geometries of all species.

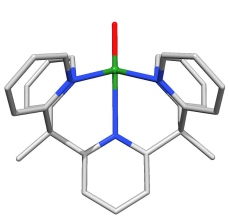

(a) **A**

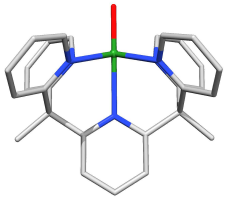

(b) **B**

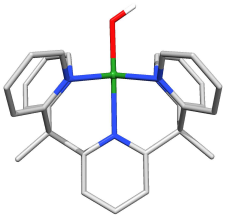

(c) **C**

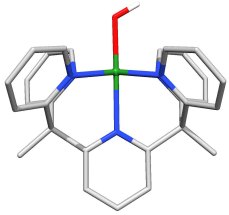

(d) **D**

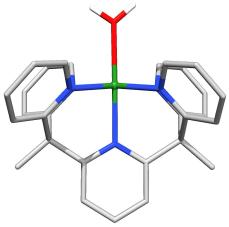

(e) **E**

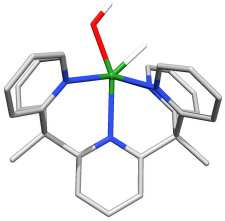

(f) **F**

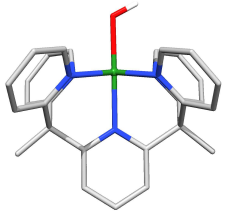

(g) **G**

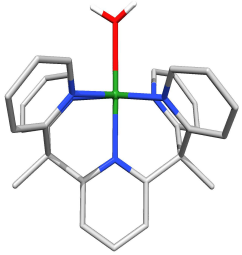

(h) **H**

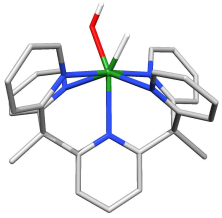

(i) **I**

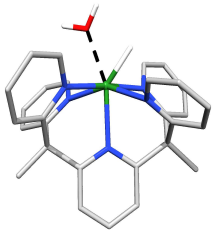

(j) **J**

Appendix B

Calculation of $\langle S^2 \rangle$ for two Non-Orthogonal GHF Determinants

The equation for computing $\langle S^2 \rangle$ between two non-orthogonal determinants may be written as:

$$\left\langle {}^{w}\Psi \left| S^2 \right| {}^{x}\Psi \right\rangle = \left\langle {}^{w}\Psi \left| S_x^2 \right| {}^{x}\Psi \right\rangle + \left\langle {}^{w}\Psi \left| S_y^2 \right| {}^{x}\Psi \right\rangle \tag{B.1}$$

$$+ \left\langle {}^{w}\Psi \left| S_z^2 \right| {}^{x}\Psi \right\rangle \tag{B.2}$$

$$\left\langle {}^{w}\Psi \left| S_\sigma^2 \right| {}^{x}\Psi \right\rangle = \left\langle {}^{w}\Psi \left| S_\sigma \right| {}^{w}\Psi \right\rangle \left\langle {}^{w}\Psi \mid {}^{x}\Psi \right\rangle \left\langle {}^{x}\Psi \left| S_\sigma \right| {}^{x}\Psi \right\rangle \tag{B.3}$$

$$+ \sum_{ia} \left\langle {}^{w}\Psi \left| S_\sigma \right| {}^{w}\Psi_i^a \right\rangle \left\langle {}^{w}\Psi_i^a \mid {}^{x}\Psi \right\rangle \left\langle {}^{x}\Psi \left| S_\sigma \right| {}^{x}\Psi \right\rangle \tag{B.4}$$

$$+ \sum_{jb} \left\langle {}^{w}\Psi \left| S_\sigma \right| {}^{w}\Psi \right\rangle \left\langle {}^{w}\Psi \mid {}^{x}\Psi_j^b \right\rangle \left\langle {}^{x}\Psi_j^b \left| S_\sigma \right| {}^{x}\Psi \right\rangle \tag{B.5}$$

$$+ \sum_{ia,jb} \left\langle {}^{w}\Psi \left| S_\sigma \right| {}^{w}\Psi_i^a \right\rangle \left\langle {}^{w}\Psi_i^a \mid {}^{x}\Psi_j^b \right\rangle \left\langle {}^{x}\Psi_j^b \left| S_\sigma \right| {}^{x}\Psi \right\rangle \tag{B.6}$$

where $\sigma = x, y, z$. We shall now show how to compute each matrix element for GHF Slater determinants in the above equation. The equations for the spin components for a given ground state determinant with itself are given by:

$$\langle \Psi \left| S_z \right| \Psi \rangle = \frac{1}{2} \left(\mathrm{tr} \left(\mathbf{S}_{AO} \mathbf{P}_{\alpha\alpha} \right) - \mathrm{tr} \left(\mathbf{S}_{AO} \mathbf{P}_{\beta\beta} \right) \right) \tag{B.7}$$

$$\langle \Psi \left| S_x \right| \Psi \rangle = \frac{1}{2} \left(\mathrm{tr} \left(\mathbf{S}_{AO} \mathbf{P}_{\alpha\beta} \right) + \mathrm{tr} \left(\mathbf{S}_{AO} \mathbf{P}_{\beta\alpha} \right) \right) \tag{B.8}$$

$$\langle \Psi \left| S_y \right| \Psi \rangle = \frac{1}{2} \left(\mathrm{tr} \left(\mathbf{S}_{AO} \mathbf{P}_{\alpha\beta} \right) - \mathrm{tr} \left(\mathbf{S}_{AO} \mathbf{P}_{\beta\alpha} \right) \right) \tag{B.9}$$

where $\mathbf{P}_{\alpha\beta}$ etc. are the blocks of the GHF density matrix and $\mathbf{S}_{AO}$ is the atomic orbital overlap. These are obtained by applying the the Pauli spin matrices to our non-collinear (GHF) wavefunction.[202, 252] To compute $\langle {}^{w}\Psi \mid {}^{x}\Psi \rangle$ we use the fact that in the corresponding

orbital basis the inter-determinantal overlap matrix ${}^{wx}\mathbf{S}$ is diagonal, which gives us:

$$\langle {}^{w}\Psi \mid {}^{x}\Psi \rangle = \det\left({}^{wx}\mathbf{S}\right) = \prod_{i} s_i \tag{B.10}$$

where s_i are the elements of that diagonal. To compute $\langle {}^{w}\Psi \left| S_\sigma \right| {}^{w}\Psi_i^a \rangle$ we recall that each individual Slater determinant maintains orthogonality between their respective occupied and virtual subspaces, therefore:

$$\begin{aligned}
\langle \Psi \left| S_z \right| \Psi_i^a \rangle &= \sum_{\mu\nu} {}^{\alpha}C_{i\cdot}^{\cdot\mu} \langle \omega_\mu \mid \omega_\nu \rangle {}^{\alpha}C_{\cdot a}^{\nu\cdot} - {}^{\beta}C_{i\cdot}^{\cdot\mu} \langle \omega_\mu \mid \omega_\nu \rangle {}^{\beta}C_{\cdot a}^{\nu\cdot} \\
\langle \Psi \left| S_x \right| \Psi_i^a \rangle &= \sum_{\mu\nu} {}^{\beta}C_{i\cdot}^{\cdot\mu} \langle \omega_\mu \mid \omega_\nu \rangle {}^{\alpha}C_{\cdot a}^{\nu\cdot} + {}^{\alpha}C_{i\cdot}^{\cdot\mu} \langle \omega_\mu \mid \omega_\nu \rangle {}^{\beta}C_{\cdot a}^{\nu\cdot} \\
\langle \Psi \left| S_y \right| \Psi_i^a \rangle &= \sum_{\mu\nu} {}^{\beta}C_{i\cdot}^{\cdot\mu} \langle \omega_\mu \mid \omega_\nu \rangle {}^{\alpha}C_{\cdot a}^{\nu\cdot} - {}^{\alpha}C_{i\cdot}^{\cdot\mu} \langle \omega_\mu \mid \omega_\nu \rangle {}^{\beta}C_{\cdot a}^{\nu\cdot}
\end{aligned} \tag{B.11}$$

To compute $\langle {}^{w}\Psi_i^a \mid {}^{x}\Psi \rangle$ and $\left\langle {}^{w}\Psi \mid {}^{x}\Psi_j^b \right\rangle$ we recognize that in the corresponding orbital basis a single substitution in the coefficient matrix replaces either a row or column of ${}^{wx}\mathbf{S}$, changing the determinant of that matrix by one value:

$$\langle {}^{w}\Psi_i^a \mid {}^{x}\Psi \rangle = \frac{\det\left({}^{wx}\mathbf{S}\right) \langle {}^{w}\phi_a \mid {}^{x}\phi_i \rangle}{{}^{wx}S_{ii}} \tag{B.12}$$

$$\left\langle {}^{w}\Psi \mid {}^{x}\Psi_j^b \right\rangle = \frac{\det\left({}^{wx}\mathbf{S}\right) \langle {}^{w}\phi_j \mid {}^{x}\phi_b \rangle}{{}^{wx}S_{jj}} \tag{B.13}$$

In order to compute the final element, $\left\langle {}^{w}\Psi_i^a \mid {}^{x}\Psi_j^b \right\rangle$, we will utilize the matrix determinant lemma which states:

$$\det\left(\mathbf{A} + \mathbf{U}\mathbf{V}^\dagger\right) = \det\left(\mathbf{I} + \mathbf{V}^\dagger\mathbf{A}^{-1}\mathbf{U}\right) \det\left(\mathbf{A}\right) \tag{B.14}$$

where $\mathbf{A}$ is an n-by-n invertible matrix and $\mathbf{U}$ and $\mathbf{V}$ are n-by-m matrices and are not related to the $\mathbf{U}$ and $\mathbf{V}$ of the SVD. The lemma becomes useful when we notice that, akin to the element $\langle {}^{w}\Psi_i^a \mid {}^{x}\Psi \rangle$ computed above, the element $\left\langle {}^{w}\Psi_i^a \mid {}^{x}\Psi_j^b \right\rangle$ involves replacing a row and a column of ${}^{wx}\mathbf{S}$. In our case the matrix $\mathbf{A}$ will be the corresponding orbitals overlap matrix ${}^{wx}\mathbf{S}$, the determinant of which is $\langle {}^{w}\Psi \mid {}^{x}\Psi \rangle$ which we have already computed above. Recalling this matrix is diagonal the inverse may also be computed easily. The $\mathbf{U}$ and $\mathbf{V}$ must be constructed so that they replace the elements of the ${}^{wx}\mathbf{S}$ appropriately; in our case because we are replacing a row and a column of this matrix $\mathbf{U}$ and $\mathbf{V}$ will be n-by-2 matrices making the so far unknown determinant on the right hand side the determinant of 2-by-2 matrix. The construction of $\mathbf{U}$ and $\mathbf{V}$ involves recognizing that the substitutions in $|{}^{w}\Psi\rangle$ make for rows consisting of elements $\langle {}^{w}\phi_a \mid {}^{x}\phi_i \rangle$, substitutions in $|{}^{x}\Psi\rangle$ make for columns consisting of elements $\langle {}^{w}\phi_j \mid {}^{x}\phi_b \rangle$ and both substitutions make a point of intersection $\langle {}^{w}\phi_a \mid {}^{x}\phi_b \rangle$. Utilizing

Kronecker deltas to take into account when to add and subtract the values, we can write down $\mathbf{U}$ and $\mathbf{V}$:

$$U_{1,k} = \delta_{ki} \tag{B.15}$$

$$U_{2,k} = (1 - \delta_{ki})(\langle {}^w\phi_k \mid {}^x\phi_b \rangle - \delta_{kj} s_j) \tag{B.16}$$

$$V_{l,1} = (1 - \delta_{lj})(\langle {}^w\phi_a \mid {}^x\phi_l \rangle - \delta_{li} s_i) + \delta_{lj}(\langle {}^w\phi_a \mid {}^x\phi_b \rangle - \delta_{li} s_i) \tag{B.17}$$

$$V_{l,2} = \delta_{lj} \tag{B.18}$$

where i represents the occupied orbital substituted by a, the virtual orbital, of $|{}^w\Psi\rangle$ and j and b likewise for $|{}^x\Psi\rangle$, and the indices k and l represent dummy occupied orbital indices (the n rows of these skinny matrices). After some algebra we arrive at:

$$\det\left(\mathbf{I} + \mathbf{V}^{\dagger wx}\mathbf{S}^{-1}\mathbf{U}\right) = \tag{B.19}$$

$$= \det\begin{pmatrix} \clubsuit & \heartsuit \\ \diamondsuit & \spadesuit \end{pmatrix} \tag{B.20}$$

$$\clubsuit = \frac{\langle {}^x\phi_i \mid {}^w\phi_a \rangle}{s_i} + \delta_{ji}\left(\frac{\langle {}^x\phi_b \mid {}^w\phi_a \rangle}{s_i} - \frac{\langle {}^x\phi_i \mid {}^w\phi_a \rangle}{s_i}\right) \tag{B.21}$$

$$\heartsuit = \sum_l \frac{\langle {}^w\phi_a \mid {}^x\phi_l \rangle \langle {}^w\phi_l \mid {}^x\phi_b \rangle}{s_l} - \frac{\langle {}^w\phi_a \mid {}^x\phi_i \rangle \langle {}^w\phi_i \mid {}^x\phi_b \rangle}{s_i} \tag{B.22}$$

$$+ \frac{\langle {}^w\phi_a \mid {}^x\phi_b \rangle \langle {}^w\phi_j \mid {}^x\phi_b \rangle}{s_j} - \frac{\langle {}^w\phi_a \mid {}^x\phi_j \rangle \langle {}^w\phi_j \mid {}^x\phi_b \rangle}{s_j} - \langle {}^w\phi_a \mid {}^x\phi_b \rangle \tag{B.23}$$

$$+ \delta_{ij}\left(\frac{\langle {}^w\phi_a \mid {}^x\phi_i \rangle \langle {}^w\phi_i \mid {}^x\phi_b \rangle}{s_i} - \frac{\langle {}^w\phi_a \mid {}^x\phi_b \rangle \langle {}^w\phi_j \mid {}^x\phi_b \rangle}{s_j} + \langle {}^w\phi_a \mid {}^x\phi_b \rangle\right) \tag{B.24}$$

$$\diamondsuit = \delta_{ij} s_i^{-1} \tag{B.25}$$

$$\spadesuit = \frac{\langle {}^w\phi_j \mid {}^x\phi_b \rangle}{s_j} - \delta_{ji}\left(\frac{\langle {}^w\phi_i \mid {}^x\phi_b \rangle}{s_i} + 1\right) \tag{B.26}$$

$$\det\left(\mathbf{I} + \mathbf{V}^{\dagger wx}\mathbf{S}^{-1}\mathbf{U}\right) = \frac{\langle {}^w\phi_a \mid {}^x\phi_i \rangle \langle {}^w\phi_j \mid {}^x\phi_b \rangle}{s_i s_j} \tag{B.27}$$

$$+ \delta_{ji}\left(\frac{\langle {}^x\phi_b \mid {}^w\phi_a \rangle}{s_i} - s_i^{-1} \sum_l \frac{\langle {}^w\phi_a \mid {}^x\phi_l \rangle \langle {}^w\phi_l \mid {}^x\phi_b \rangle}{s_l}\right) \tag{B.28}$$

This expression can then be split up into the on and off diagonal terms, combined with Equation B.11, and contracted appropriately to form an evaluation of $\langle S^2 \rangle$ which scales as N^3 per determinantal pair where N is the size of atomic orbital basis.

References

(1) Einstein, A. Zur Theorie der Lichterzeugung und Lichtabsorption. *Annalen der Physik* **1906**, *325*, 199–206.

(2) Einstein, A. Die Plancksche Theorie der Strahlung und die Theorie der spezifischen Wärme. *Annalen der Physik* **1906**, *327*, 180–190.

(3) Schrödinger, E. Die wasserstoffähnlichen Spektren vom Standpunkte der Polarisierbarkeit des Atomrumpfes. *Annalen der Physik* **1925**, *382*, 43–70.

(4) Schrödinger, E. Quantisierung als Eigenwertproblem. *Annalen der Physik* **1926**, *384*, 361–376.

(5) Schrödinger, E. Quantisierung als Eigenwertproblem. *Annalen der Physik* **1926**, *384*, 489–527.

(6) Schrödinger, E. Über das Verhältnis der Heisenberg-Born-Jordanschen Quantenmechanik zu der meinen. *Annalen der Physik* **1926**, *384*, 734–756.

(7) Schrödinger, E. Quantisierung als Eigenwertproblem. *Annalen der Physik* **1926**, *386*, 109–139.

(8) Schrödinger, E. An Undulatory Theory of the Mechanics of Atoms and Molecules. *Physical Review* **1926**, *28*, 1049–1070.

(9) Born, M.; Heisenberg, W.; Jordan, P. Zur Quantenmechanik. II. *Zeitschrift für Physik* **1926**, *35*, 557–615.

(10) Heisenberg, W. Über eine Anwendung des Korrespondenzprinzips auf die Frage nach der Polarisation des Fluoreszenzlichtes. *Zeitschrift für Physik* **1925**, *31*, 617–626.

(11) Kramers, H. A.; Heisenberg, W. Über die Streuung von Strahlung durch Atome. *Zeitschrift für Physik* **1925**, *31*, 681–708.

(12) Broglie, L. de Research on the quantum theory. Ph.D. Thesis, Paris, 1924.

(13) Szabo, A.; Ostlund, N. S.; Szabo *Modern Quantum Chemistry: Introduction to Advanced Electronic Structure Theory*; Dover Publications; New edition edition, 1996.

(14) Born, M.; Oppenheimer, R. Zur Quantentheorie der Molekeln. *Annalen der Physik* **1927**, *389*, 457–484.

(15) Pauli, W. Über den Zusammenhang des Abschlusses der Elektronengruppen im Atom mit der Komplexstruktur der Spektren. *Zeitschrift für Physik* **1925**, *31*, 765–783.

(16) Slater, J. Note on Hartree's method. *Physical Review* **1930**, *35*, 210.

(17) Slater, J. A simplification of the Hartree–Fock method. *Physical Review* **1951**, *81*, 385.

(18) Fock, V; Petrashen, M. J. Numerical solution of generalised equations of the self-consistent field. *Physikalische Zeitschrift der Sowjetunion* **1934**, *6*, 368–414.

(19) Fock, V. A.; Petrashen, M. I. Calculation of the self-consistent field with exchange for lithium. *Proceedings of the USSR Academy of Science* **1935**, *8*, 295–296.

(20) Hartree, D. R. The Wave Mechanics of an Atom with a Non-Coulomb Central Field. Part I. Theory and Methods. *Mathematical Proceedings of the Cambridge Philosophical Society* **1928**, *24*, 89.

(21) Hartree, D. R. The Wave Mechanics of an Atom with a Non-Coulomb Central Field. Part II. Some Results and Discussion. *Mathematical Proceedings of the Cambridge Philosophical Society* **1928**, *24*, 111.

(22) Hartree, D. R. The Wave Mechanics of an Atom with a non-Coulomb Central Field. Part III. Term Values and Intensities in Series in Optical Spectra. *Mathematical Proceedings of the Cambridge Philosophical Society* **1928**, *24*, 426.

(23) Head-Gordon, M.; Maslen, P. E.; White, C. A. A tensor formulation of many-electron theory in a nonorthogonal single-particle basis. *The Journal of Chemical Physics* **1998**, *108*, 616.

(24) Pople, J. A.; Nesbet, R. K. Self-Consistent Orbitals for Radicals. *The Journal of Chemical Physics* **1954**, *22*, 571.

(25) Hohenberg, P.; Kohn, W. Inhomogeneous electron gas. *Physical Review* **1964**, *136*, B864–B871.

(26) Kohn, W.; Sham, L. Self-consistent equations including exchange and correlation effects. *Physical Review* **1965**, *140*, A1133–A1138.

(27) Pople, J. A.; Gill, P. M.; Johnson, B. G. Kohn–Sham density-functional theory within a finite basis set. *Chemical Physics Letters* **1992**, *199*, 557–560.

(28) Becke, A. D. Perspective: Fifty years of density-functional theory in chemical physics. *The Journal of Chemical Physics* **2014**, *140*, 18A301.

(29) Perdew, J. P.; Zunger, A. Self-interaction correction to density-functional approximations for many-electron systems. *Physical Review B* **1981**, *23*, 5048–5079.

(30) Perdew, J. P. J.; Wang, Y. Accurate and simple analytic representation of the electron-gas correlation energy. *Physical Review B* **1992**, *45*, 244–249.

(31) Perdew, J. P.; Yue, W. Accurate and simple density functional for the electronic exchange energy: Generalized gradient approximation. *Physical Review B* **1986**, *33*, 8800–8802.

(32) Becke, A. D. Density functional calculations of molecular bond energies. *The Journal of Chemical Physics* **1986**, *84*, 4524.

(33) Becke, A. D. Density-functional exchange-energy approximation with correct asymptotic behavior. *Physical Review A* **1988**, *38*, 3098–3100.

(34) Lee, C.; Yang, W.; Parr, R. G. R. Development of the Colle-Salvetti correlation-energy formula into a functional of the electron density. *Physical Review B* **1988**, *37*, 785–789.

(35) Perdew, J.; Chevary, J.; Vosko, S.; Jackson, K. A.; Pederson, M. R.; Singh, D. J.; Fiolhais, C. Atoms, molecules, solids, and surfaces: applications of the generalized gradient approximation for exchange and correlation. *Physical Review B* **1992**, *46*.

(36) Perdew, J. P.; Burke, K.; Ernzerhof, M. Generalized Gradient Approximation Made Simple. *Physical Review Letters* **1996**, *77*, 3865–3868.

(37) Van Voorhis, T.; Scuseria, G. E. A novel form for the exchange-correlation energy functional. *The Journal of Chemical Physics* **1998**, *109*, 400.

(38) Zhao, Y.; Schultz, N. E.; Truhlar, D. G. Exchange-correlation functional with broad accuracy for metallic and nonmetallic compounds, kinetics, and noncovalent interactions. *The Journal of Chemical Physics* **2005**, *123*, 161103.

(39) Becke, A. D. A new inhomogeneity parameter in density-functional theory. *The Journal of Chemical Physics* **1998**, *109*, 2092.

(40) Becke, A. D. Density-functional Thermochemistry. III. The role of exact exchange. *Journal of Chemical Physics* **1993**, *98*, 6–10.

(41) Becke, A. D. Density-functional thermochemistry. V. Systematic optimization of exchange-correlation functionals. *The Journal of Chemical Physics* **1997**, *107*, 8554.

(42) Iikura, H.; Tsuneda, T.; Yanai, T.; Hirao, K. A long-range correction scheme for generalized-gradient-approximation exchange functionals. *The Journal of Chemical Physics* **2001**, *115*, 3540.

(43) Chai, J.-D.; Head-Gordon, M. Systematic optimization of long-range corrected hybrid density functionals. *The Journal of Chemical Physics* **2008**, *128*, 084106.

(44) Grimme, S. Semiempirical GGA-type density functional constructed with a long-range dispersion correction. *Journal of Computational Chemistry* **2006**, *27*, 1787–99.

(45) Becke, A. D. A new mixing of Hartree–Fock and local density-functional theories. *The Journal of Chemical Physics* **1993**, *98*, 1372.

(46) Hirao, K.; Hatano, Y. Cluster expansion of the wavefunction. Comparison with full CI results. *Chemical Physics Letters* **1983**, *100*, 519–522.

(47) Povill, A.; Rubio, J. Using full-CI algorithms in Bethe-Goldstone-type expansions of the correlation energy. *International Journal of Quantum Chemistry* **1997**, *61*, 35–43.

(48) Helgaker, T.; Olsen, J.; Jorgensen, P. *Molecular Electronic-Structure Theory*, 1st; John Wiley & Sons, Inc.: New York, 2000.

(49) Crawford, T. D.; Schaefer, H. F. I. An Introduction to Coupled Cluster Theory for Computational Chemists. *Reviews in Computational Chemistry* **2000**, *14*, 33–136.

(50) Schrödinger, E. Quantisierung als Eigenwertproblem. *Annalen der Physik* **1926**, *385*, 437–490.

(51) Coester, F.; Kümmel, H. Short-range correlations in nuclear wave functions. *Nuclear Physics* **1960**, *17*, 477–485.

(52) Čížek, J. On the Correlation Problem in Atomic and Molecular Systems. Calculation of Wavefunction Components in Ursell-Type Expansion Using Quantum-Field Theoretical Methods. *The Journal of Chemical Physics* **1966**, *45*, 4256.

(53) Čížek, J. On the Use of the Cluster Expansion and the Technique of Diagrams in Calculations of Correlation Effects in Atoms and Molecules. *Advances in Chemical Physics* **1969**, *14*.

(54) Čížek, J.; Paldus, J. Correlation problems in atomic and molecular systems III. Rederivation of the coupled-pair many-electron theory using the traditional quantum chemical methods. *International Journal of Quantum Chemistry* **1971**, *5*, 359–379.

(55) Pople, J. A.; Krishnan, R.; Schlegel, H. B.; Binkley, J. S. Electron correlation theories and their application to the study of simple reaction potential surfaces. *International Journal of Quantum Chemistry* **1978**, *14*, 545–560.

(56) Bartlett, R. J.; Purvis, G. D. Many-body perturbation theory, coupled-pair many-electron theory, and the importance of quadruple excitations for the correlation problem. *International Journal of Quantum Chemistry* **1978**, *14*, 561–581.

(57) Stanton, J. F.; Gauss, J.; Watts, J. D.; Bartlett, R. J. A direct product decomposition approach for symmetry exploitation in many-body methods. I. Energy calculations. *The Journal of Chemical Physics* **1991**, *94*, 4334.

(58) Krylov, A. I. Spin-flip configuration interaction: an electronic structure model that is both variational and size-consistent. *Chemical Physics Letters* **2001**, *350*, 522–530.

(59) Shao, Y.; Head-Gordon, M.; Krylov, A. I. The spin-flip approach within time-dependent density functional theory: Theory and applications to diradicals. *The Journal of Chemical Physics* **2003**, *118*, 4807.

(60) Levchenko, S. V.; Krylov, A. I. Equation-of-motion spin-flip coupled-cluster model with single and double substitutions: Theory and application to cyclobutadiene. *The Journal of Chemical Physics* **2004**, *120*, 175–85.

(61) Casanova, D.; Head-Gordon, M. Restricted active space spin-flip configuration interaction approach: theory, implementation and examples. *Physical Chemistry Chemical Physics* **2009**, *11*, 9779–90.

(62) Zimmerman, P. M.; Bell, F.; Goldey, M.; Bell, A. T.; Head-Gordon, M. Restricted active space spin-flip configuration interaction: theory and examples for multiple spin flips with odd numbers of electrons. *The Journal of Chemical Physics* **2012**, *137*, 164110.

(63) Casanova, D. Avoided crossings, conical intersections, and low-lying excited states with a single reference method: the restricted active space spin-flip configuration interaction approach. *The Journal of Chemical Physics* **2012**, *137*, 084105.

(64) Roos, B. O. In *Advances in Chemical Physics: Ab Initio Methods in Quantum Chemistry Part 2, Volume 69*; Lawley, K. P., Ed.; Advances in Chemical Physics, Vol. 69; John Wiley & Sons, Inc.: Hoboken, NJ, USA, 1987, pp 399–442.

(65) Andersson, K.; Malmqvist, P.-Å.; Roos, B. O. Second-order perturbation theory with a complete active space self-consistent field reference function. *Journal of Chemical Physics* **1992**, *96*, 1218–1226.

(66) Chan, G. K.-L.; Sharma, S. The density matrix renormalization group in quantum chemistry. *Annual Review of Physical Chemistry* **2011**, *62*, 465–81.

(67) Jansen, M.; Wedig, U. A piece of the picture–misunderstanding of chemical concepts. *Angewandte Chemie* **2008**, *47*, 10026–9.

(68) Aullón, G.; Alvarez, S. Oxidation states, atomic charges and orbital populations in transition metal complexes. *Theoretical Chemistry Accounts* **2009**, *123*, 67–73.

(69) Shields, G. P.; Raithby, P. R.; Allen, F. H.; Motherwell, W. D. S. The assignment and validation of metal oxidation states in the Cambridge Structural Database. *Acta Crystallographica Section B Structural Science* **2000**, *56*, 455–465.

(70) Orpen, A. G. Applications of the Cambridge Structural Database to molecular inorganic chemistry. *Acta Crystallographica Section B Structural Science* **2002**, *58*, 398–406.

(71) Palenik, G. J. Bond Valence Sums in Coordination Chemistry Using Oxidation State Independent R_0 Values. A Simple Calculation of the Oxidation State of Titanium in Complexes Containing Ti–N, Ti–O, and Ti–Cl Bonds. *Inorganic Chemistry* **1997**, *36*, 3394–3397.

(72) Wood, R. M.; Palenik, G. J. Bond Valence Sums in Coordination Chemistry. A Simple Method for Calculating the Oxidation State of Cobalt in Complexes Containing Only Co–O Bonds. *Inorganic Chemistry* **1998**, *37*, 4149–4151.

(73) Mulliken, R. S. Electronic Population Analysis on LCAO-MO Molecular Wave Functions. II. Overlap Populations, Bond Orders, and Covalent Bond Energies. *The Journal of Chemical Physics* **1955**, *23*, 1841.

(74) Mulliken, R. S. Electronic Population Analysis on LCAO-MO Molecular Wave Functions. IV. Bonding and Antibonding in LCAO and Valence-Bond Theories. *The Journal of Chemical Physics* **1955**, *23*, 2343.

(75) Mulliken, R. S. Electronic Population Analysis on LCAO-MO Molecular Wave Functions. I. *The Journal of Chemical Physics* **1955**, *23*, 1833.

(76) Mulliken, R. S. Electronic Population Analysis on LCAO-MO Molecular Wave Functions. III. Effects of Hybridization on Overlap and Gross AO Populations. *The Journal of Chemical Physics* **1955**, *23*, 2338.

(77) Mayer, I. Charge, bond order and valence in the Ab initio SCF theory. *Chemical Physics Letters* **1983**, *97*, 270–274.

(78) Mayer, I Comments on the Quantum Theory of Valence and Bonding: Choosing Between Alternative Definitions. *Chemical Physics Letters* **1984**, *110*, 440–444.

(79) Mayer, I. On bond orders and valences in the Ab initio quantum chemical theory. *International Journal of Quantum Chemistry* **1986**, *29*, 73–84.

(80) Löwdin, P. On the Non-Orthogonality Problem Connected with the Use of Atomic Wave Functions in the Theory of Molecules and Crystals. *The Journal of Chemical Physics* **1950**, *18*, 365.

(81) Löwdin, P. Quantum theory of many-particle systems. I. Physical interpretations by means of density matrices, natural spin-orbitals, and convergence problems in the method of configurational interaction. *Physical Review* **1955**, *97*, 1474.

(82) Reed, A. E.; Weinhold, F. Natural bond orbital analysis of near-Hartree–Fock water dimer. *Journal of Chemical Physics* **1983**, *78*, 4066.

(83) Reed, A. E.; Weinstock, R. B.; Weinhold, F. Natural Population Analysis. *The Journal of Chemical Physics* **1985**, *83*, 735.

(84) Reed, A. E.; Curtiss, L. A.; Weinhold, F. Intermolecular interactions from a natural bond orbital, donor-acceptor viewpoint. *Chemical Reviews* **1988**, *88*, 899–926.

(85) Clark, A. E.; Davidson, E. R. Local spin. *The Journal of Chemical Physics* **2001**, *115*, 7382.

(86) Herrmann, C.; Reiher, M.; Hess, B. a. Comparative analysis of local spin definitions. *The Journal of Chemical Physics* **2005**, *122*, 34102.

(87) Davidson, E. R.; Clark, A. E. Analysis of wave functions for open-shell molecules. *Physical Chemistry Chemical Physics* **2007**, *9*, 1881–94.

(88) Mayer, I. Local spins: An alternative treatment for single determinant wave functions. *Chemical Physics Letters* **2007**, *440*, 357–359.

(89) Alcoba, D. R.; Lain, L.; Torre, A.; Bochicchio, R. C. Local spin: A treatment beyond single determinant wave functions. *Chemical Physics Letters* **2009**, *470*, 136–139.

(90) Becke, A.; Edgecombe, K. A simple measure of electron localization in atomic and molecular systems. *The Journal of Chemical Physics* **1990**, *92*, 5397.

(91) Bader, R. *Atoms in Molecules*; Clarendon Press New York, 1990.

(92) Bader, R. F. W. A quantum theory of molecular structure and its applications. *Chemical Reviews* **1991**, *91*, 893–928.

(93) Rhee, Y. M.; Head-Gordon, M. A delicate electronic balance between metal and ligand in [Cu-P-Cu-P] diamondoids: oxidation state dependent plasticity and the formation of a singlet diradicaloid. *Journal of the American Chemical Society* **2008**, *130*, 3878–87.

(94) Boys, S. F. Construction of the Some Molecular Orbitals to Be Approximately Invariant for Changes from One Molecule to Another. *Reviews of Modern Physics* **1960**, *32*, 296–299.

(95) Pipek, J.; Mezey, P. G. A fast intrinsic localization procedure applicable for ab initio and semiempirical linear combination of atomic orbital wave functions. *Journal of Chemical Physics* **1989**, *90*, 4916.

(96) Pipek, J.; Mezey, P. Dependence of MO shapes on a continuous measure of delocalization. *International Journal of Quantum Chemistry* **1988**, *34*, 1–13.

(97) Edmiston, C.; Ruedenberg, K. Localized atomic and molecular orbitals. *Reviews of Modern Physics* **1963**, *35*, 457.

(98) Shao, Y. et al. Advances in methods and algorithms in a modern quantum chemistry program package. *Physical Chemistry Chemical Physics* **2006**, *8*, 3172–91.

(99) Bhaduri, S.; Tasiopoulos, A. J.; Bolcar, M. A.; Abboud, K. A.; Streib, W. E.; Christou, G. Symmetric and asymmetric dinuclear manganese(IV) complexes possessing a $[Mn_2^{IV}(\mu - O)_2(\mu - O_2CMe)]^{3+}$ core and terminal Cl^- ligands. *Inorganic Chemistry* **2003**, *42*, 1483–92.

(100) Cancès, E. Self-consistent field algorithms for Kohn–Sham models with fractional occupation numbers. *The Journal of Chemical Physics* **2001**, *114*, 10616.

(101) Cancès, E.; Le Bris, C. Can we outperform the DIIS approach for electronic structure calculations? *International Journal of Quantum Chemistry* **2000**, *79*, 82–90.

(102) Van Voorhis, T.; Head-Gordon, M. A geometric approach to direct minimization. *Molecular Physics* **2002**, *100*, 1713–1721.

(103) Kohn, W.; Becke, A. D.; Parr, R. G. Density Functional Theory of Electronic Structure. *The Journal of Physical Chemistry* **1996**, *100*, 12974–12980.

(104) Perdew, J. Density-functional approximation for the correlation energy of the inhomogeneous electron gas. *Physical Review B* **1986**, *33*, 8822.

(105) Chai, J.-D.; Head-Gordon, M. Long-range corrected hybrid density functionals with damped atom-atom dispersion corrections. *Physical Chemistry Chemical Physics* **2008**, *10*, 6615–20.

(106) Seeger, R.; Pople, J. A. Self-consistent molecular orbital methods. XVIII. Constraints and stability in Hartree–Fock theory. *The Journal of Chemical Physics* **1977**, *66*, 3045–3050.

(107) Binkley, J. S.; Pople, J. A.; Hehre, W. J. Self-consistent molecular orbital methods. 21. Small split-valence basis sets for first-row elements. *Journal of the American Chemical Society* **1980**, *102*, 939–947.

(108) Hehre, W. J.; Ditchfield, R.; Pople, J. A. Self-Consistent Molecular Orbital Methods. XII. Futher Externsions of Gaussian-Type Basis Sets for Use in Molecular Orbital Studies of Organic Molecules. *The Journal of Chemical Physics* **1972**, *56*, 2257.

(109) Francl, M. M.; Pietro, W. J.; Hehre, W. J.; Binkley, J. S.; Gordon, M. S.; DeFrees, D. J.; Pople, J. A. Self-consistent molecular orbital methods. XXIII. A polarization-type basis set for second-row elements. *The Journal of Chemical Physics* **1982**, *77*, 3654.

(110) Thom, A.; Head-Gordon, M. Locating Multiple Self-Consistent Field Solutions: An Approach Inspired by Metadynamics. *Physical Review Letters* **2008**, *101*, 1–4.

(111) Subotnik, J. E.; Shao, Y.; Liang, W.; Head-Gordon, M. An efficient method for calculating maxima of homogeneous functions of orthogonal matrices: applications to localized occupied orbitals. *The Journal of Chemical Physics* **2004**, *121*, 9220–9.

(112) Weigend, F RI-MP2: optimized auxiliary basis sets and demonstration of efficiency. *Chemical Physics Letters* **1998**, *294*, 143–152.

(113) Johnson, R. D. NIST Computation Chemistry Comparison and Benchmark Database, NIST Standard Reference Database Number 101 Release 14.

(114) *CRC Handbook of Chemistry and Physics*, 89th ed.; Lide, D. R., Ed.; CRC Press/Taylor and Francis.

(115) Deeth, R. J. Density functional study of the tetraoxometallates of Cr^{VI} , Mn^{VI} and Fe^{VI}. *Journal of the Chemical Society, Faraday Transactions* **1993**, *89*, 3745.

(116) Mccusker, J. K. Fuel from Photons. *Science* **2001**, *293*, 1599–1601.

(117) Lewis, N. S.; Nocera, D. G. Powering the planet: chemical challenges in solar energy utilization. *Proceedings of the National Academy of Sciences of the United States of America* **2006**, *103*, 15729–35.

(118) Yano, J.; Kern, J.; Sauer, K.; Latimer, M. J.; Pushkar, Y.; Biesiadka, J.; Loll, B.; Saenger, W.; Messinger, J.; Zouni, A.; Yachandra, V. K. Where water is oxidized to dioxygen: structure of the photosynthetic Mn4Ca cluster. *Science* **2006**, *314*, 821–5.

(119) Lundberg, M.; Siegbahn, P. E. M. Theoretical investigations of structure and mechanism of the oxygen-evolving complex in PSII. *Physical Chemistry Chemical Physics* **2004**, *6*, 4772.

(120) Sproviero, E. M.; Gascón, J. a.; McEvoy, J. P.; Brudvig, G. W.; Batista, V. S. QM/MM Models of the O_2-Evolving Complex of Photosystem II. *Journal of Chemical Theory and Computation* **2006**, *2*, 1119–1134.

(121) Lundberg, M.; Blomberg, M. R. A.; Siegbahn, P. E. M. Oxyl radical required for o–o bond formation in synthetic Mn-catalyst. *Inorganic Chemistry* **2004**, *43*, 264–74.

(122) Diedrich, C.; Deeth, R. J. On the performance of ligand field molecular mechanics for model complexes containing the peroxido-bridged $[Cu_2O_2]^{2+}$ center. *Inorganic Chemistry* **2008**, *47*, 2494–506.

(123) Isobe, H.; Soda, T.; Kitagawa, Y.; Takano, Y.; Kawakami, T.; Yoshioka, Y.; Yamaguchi, K. EHF theory of chemical reactions V. Nature of manganese-oxygen bonds by hybrid density functional theory (DFT) and coupled-cluster (CC) methods. *International Journal of Quantum Chemistry* **2001**, *85*, 34–43.

(124) Yamaguchi, K.; Yamanaka, S.; Isobe, H.; Shoji, M.; Koizumi, K.; Kitagawa, Y.; Kawakami, T.; Okumura, M. Theory of chemical bonds in metalloenzymes VI: Manganese–oxo bonds in the photosynthesis II system. *Polyhedron* **2007**, *26*, 2216–2224.

(125) Delfs, C. D.; Stranger, R. Oxidation State Dependence of the Geometry, Electronic Structure, and Magnetic Coupling in Mixed Oxo- and Carboxylato-Bridged Manganese Dimers. *Inorganic Chemistry* **2001**, *40*, 3061–3076.

(126) Yang, X.; Baik, M.-H. cis,cis-[(bpy)2RuVO]2O4+ catalyzes water oxidation formally via in situ generation of radicaloid RuIV-O*. *Journal of the American Chemical Society* **2006**, *128*, 7476–85.

(127) Aullón, G.; Ruiz, E.; Alvarez, S. Theoretical clues to the mechanism of dioxygen formation at the oxygen-evolving complex of photosystem II. *Chemistry (Weinheim an der Bergstrasse, Germany)* **2002**, *8*, 2508–15.

(128) Wu, A. J.; Penner-Hahn, J. E.; Pecoraro, V. L. Structural, spectroscopic, and reactivity models for the manganese catalases. *Chemical Reviews* **2004**, *104*, 903–38.

(129) Turner, J. A. Sustainable hydrogen production. *Science* **2004**, *305*, 972–4.

(130) Cook, T. R.; Dogutan, D. K.; Reece, S. Y.; Surendranath, Y.; Teets, T. S.; Nocera, D. G. Solar energy supply and storage for the legacy and nonlegacy worlds. *Chemical Reviews* **2010**, *110*, 6474–502.

(131) Sun, L; Akermark, B; Ott, S Iron hydrogenase active site mimics in supramolecular systems aiming for light-driven hydrogen production. *Coordination Chemistry Reviews* **2005**, *249*, 1653–1663.

(132) Evans, D. J.; Pickett, C. J. Chemistry and the hydrogenases. *Chemical Society Reviews* **2003**, *32*, 268.

(133) Darensbourg, M. Y.; Lyon, E. J.; Zhao, X.; Georgakaki, I. P. The organometallic active site of [Fe]hydrogenase: models and entatic states. *Proceedings of the National Academy of Sciences of the United States of America* **2003**, *100*, 3683–8.

(134) Gloaguen, F.; Rauchfuss, T. B. Small molecule mimics of hydrogenases: hydrides and redox. *Chemical Society Reviews* **2009**, *38*, 100–8.

(135) Felton, G. A. N.; Vannucci, A. K.; Chen, J.; Lockett, L. T.; Okumura, N.; Petro, B. J.; Zakai, U. I.; Evans, D. H.; Glass, R. S.; Lichtenberger, D. L. Hydrogen generation from weak acids: electrochemical and computational studies of a diiron hydrogenase mimic. *Journal of the American Chemical Society* **2007**, *129*, 12521–30.

(136) Du, P.; Knowles, K.; Eisenberg, R. A homogeneous system for the photogeneration of hydrogen from water based on a platinum(II) terpyridyl acetylide chromophore and a molecular cobalt catalyst. *Journal of the American Chemical Society* **2008**, *130*, 12576–7.

(137) Fihri, A.; Artero, V.; Razavet, M.; Baffert, C.; Leibl, W.; Fontecave, M. Cobaloxime-based photocatalytic devices for hydrogen production. *Angewandte Chemie* **2008**, *47*, 564–7.

(138) Baffert, C.; Artero, V.; Fontecave, M. Cobaloximes as functional models for hydrogenases. 2. Proton electroreduction catalyzed by difluoroborylbis (dimethylglyoximato) cobalt(II) complexes in organic media. *Inorganic Chemistry* **2007**, *46*, 1817–24.

(139) Hu, X.; Brunschwig, B. S.; Peters, J. C. Electrocatalytic hydrogen evolution at low overpotentials by cobalt macrocyclic glyoxime and tetraimine complexes. *Journal of the American Chemical Society* **2007**, *129*, 8988–98.

(140) Wilson, A. D.; Newell, R. H.; McNevin, M. J.; Muckerman, J. T.; Rakowski DuBois, M; DuBois, D. L. Hydrogen oxidation and production using nickel-based molecular catalysts with positioned proton relays. *Journal of the American Chemical Society* **2006**, *128*, 358–66.

(141) Appel, A. M.; DuBois, D. L.; Rakowski DuBois, M Molybdenum-sulfur dimers as electrocatalysts for the production of hydrogen at low overpotentials. *Journal of the American Chemical Society* **2005**, *127*, 12717–26.

(142) Goldsmith, J. I.; Hudson, W. R.; Lowry, M. S.; Anderson, T. H.; Bernhard, S. Discovery and high-throughput screening of heteroleptic iridium complexes for photoinduced hydrogen production. *Journal of the American Chemical Society* **2005**, *127*, 7502–10.

(143) Karunadasa, H. I.; Chang, C. J.; Long, J. R. A molecular molybdenum-oxo catalyst for generating hydrogen from water. *Nature* **2010**, *464*, 1329–33.

(144) Sun, Y.; Bigi, J. P.; Piro, N. A.; Tang, M. L.; Long, J. R.; Chang, C. J. Molecular cobalt pentapyridine catalysts for generating hydrogen from water. *Journal of the American Chemical Society* **2011**, *133*, 9212–5.

(145) Thoi, V. S.; Karunadasa, H. I.; Surendranath, Y.; Long, J. R.; Chang, C. J. Electrochemical generation of hydrogen from acetic acid using a molecular molybdenum–oxo catalyst. *Energy & Environmental Science* **2012**, *5*, 7762.

(146) Baik, M.-H.; Friesner, R. A. Computing Redox Potentials in Solution: Density Functional Theory as a Tool for Rational Design of Redox Agents. *The Journal of Physical Chemistry A* **2002**, *106*, 7407–7412.

(147) Winget, P.; Cramer, C. J.; Truhlar, D. G. Computation of equilibrium oxidation and reduction potentials for reversible and dissociative electron-transfer reactions in solution. *Theoretical Chemistry Accounts* **2004**, *112*, 217–227.

(148) Bell, A. T.; Head-Gordon, M. Quantum Mechanical Modeling of Catalytic Processes. *Annual Review of Chemical and Biomolecular Engineering* **2011**, *2*, 453–477.

(149) Thom, A. J. W.; Sundstrom, E. J.; Head-Gordon, M. LOBA: a localized orbital bonding analysis to calculate oxidation states, with application to a model water oxidation catalyst. *Physical Chemistry Chemical Physics* **2009**, *11*, 11297–304.

(150) Li, J.; Yoshizawa, K. Computational Evidence for Hydrogen Generation by Reductive Cleavage of Water and α-H Abstraction on a Molybdenum Complex. *Angewandte Chemie* **2011**, *50*, 11972–11975.

(151) Ziegler, T. Approximate density functional theory as a practical tool in molecular energetics and dynamics. *Chemical Reviews* **1991**, *91*, 651–667.

(152) Ziegler, T. Density functional theory as a practical tool for the study of elementary reaction steps in organometallic chemistry. *Pure and applied chemistry* **1991**, *63*, 873–878.

(153) Szilagyi, R. K.; Frenking, G. Structure and Bonding of the Isoelectronic Hexacarbonyls $[Hf(CO)_6]^{2-}$, $[Ta(CO)_6\ ]^{-}$, $W(CO)_6$, $[Re(CO)_6]$ + , $[Os(CO)_6]^{2+}$, and $[Ir(CO)_6]^{3+}$: A Theoretical Study. *Organometallics* **1997**, *16*, 4807–4815.

(154) Jonas, V.; Thiel, W. Theoretical study of the vibrational spectra of the transition-metal carbonyl hydrides $HM(CO)_5$ (M=Mn, Re), $H_2M(CO)_4$ (M=Fe, Ru, Os), and $HM(CO)_4$ (M=Co, Rh, Ir). *The Journal of Chemical Physics* **1996**, *105*, 3636.

(155) González-Blanco, O.; Branchadell, V. Density functional study of the Fe–CO bond dissociation energies of $Fe(CO)_5$. *The Journal of Chemical Physics* **1999**, *110*, 778.

(156) Hyla-Kryspin, I.; Grimme, S. Comprehensive Study of the Thermochemistry of First-Row Transition Metal Compounds by Spin Component Scaled MP2 and MP3 Methods. *Organometallics* **2004**, *23*, 5581–5592.

(157) Furche, F.; Perdew, J. P. The performance of semilocal and hybrid density functionals in 3d transition-metal chemistry. *The Journal of Chemical Physics* **2006**, *124*, 044103.

(158) Bühl, M.; Kabrede, H. Geometries of Transition-Metal Complexes from Density-Functional Theory. *Journal of Chemical Theory and Computation* **2006**, *2*, 1282–1290.

(159) Li, J. Periodic Trends and Ligand Effects in Transition Metal Dihydrogen Complexes: A Quasi-relativistic Density Functional Study. *Organometallics* **1996**, *15*, 3844–3849.

(160) Torrent, M.; Solà, M.; Frenking, G. Theoretical Studies of Some Transition-Metal-Mediated Reactions of Industrial and Synthetic Importance. *Chemical Reviews* **2000**, *100*, 439–494.

(161) Nemcsok, D. S.; Kovács, A.; Rayón, V. M.; Frenking, G. Nature of the Transition-Metal–η^2 -H_2 Bond in $TM(CO)_3X_2(\eta^2\text{-}H_2)$ (TM = Cr, Mo, W; X = CO, PH_3 , PCl_3 , PMe_3) Complexes. *Organometallics* **2002**, *21*, 5803–5809.

(162) Dolg, M.; Stoll, H.; Preuss, H.; Pitzer, R. M. Relativistic and correlation effects for element 105 (hahnium, Ha): a comparative study of M and MO (M = Nb, Ta, Ha) using energy-adjusted ab initio pseudopotentials. *The Journal of Physical Chemistry* **1993**, *97*, 5852–5859.

(163) Dunning, T. H. Gaussian basis sets for use in correlated molecular calculations. I. The atoms boron through neon and hydrogen. *The Journal of Chemical Physics* **1989**, *90*, 1007.

(164) Ahlrichs, R.; May, K. Contracted all-electron Gaussian basis sets for atoms Rb to Xe. *Physical Chemistry Chemical Physics* **2000**, *2*, 943–945.

(165) Hariharan, P. C.; Pople, J. The influence of polarization functions on molecular orbital hydrogenation energies. *Theoretica Chimica Acta* **1973**, *28*, 213–222.

(166) Khaliullin, R. Z.; Head-Gordon, M.; Bell, A. T. An efficient self-consistent field method for large systems of weakly interacting components. *The Journal of Chemical Physics* **2006**, *124*, 204105.

(167) Miertuš, S.; Scrocco, E.; Tomasi, J. Electrostatic interaction of a solute with a continuum. A direct utilizaion of AB initio molecular potentials for the prevision of solvent effects. *Chemical Physics* **1981**, *55*, 117–129.

(168) Miertuš, S.; Tomasi, J. Approximate evaluations of the electrostatic free energy and internal energy changes in solution processes. *Chemical Physics* **1982**, *65*, 239–245.

(169) Cramer, C.; Truhlar, D. Implicit solvation models: equilibria, structure, spectra, and dynamics. *Chemical Reviews* **1999**, *99*, 2161–2200.

(170) Truhlar, D. G.; Cramer, C. J.; Lewis, A.; Bumpus, J. A. Molecular Modeling of Environmentally Important Processes: Reduction Potentials. *Journal of Chemical Education* **2004**, *81*, 596.

(171) Trasatti, S. The absolute electrode potential: an explanatory note. *International Union of Pure and Applied Chemistry Commission on Electrochemistry* **1986**, *58*, 955–966.

(172) Trasatti, S. The "Absolute" Electrode Potential - The End of the Story. *Electrochimica Acta* **1990**, *35*, 269–271.

(173) Donald, W. A.; Leib, R. D.; O'Brien, J. T.; Williams, E. R. Directly relating gas-phase cluster measurements to solution-phase hydrolysis, the absolute standard hydrogen electrode potential, and the absolute proton solvation energy. *Chemistry - A European Journal* **2009**, *15*, 5926–34.

(174) Isse, A. A.; Gennaro, A. Absolute potential of the standard hydrogen electrode and the problem of interconversion of potentials in different solvents. *The Journal of Physical Chemistry B* **2010**, *114*, 7894–9.

(175) Tissandier, M. D.; Cowen, K. A.; Feng, W. Y.; Gundlach, E.; Cohen, M. H.; Earhart, A. D.; Coe, J. V.; Tuttle, T. R. The Proton's Absolute Aqueous Enthalpy and Gibbs Free Energy of Solvation from Cluster-Ion Solvation Data. *The Journal of Physical Chemistry A* **1998**, *102*, 7787–7794.

(176) Coe, J. Fundamental properties of bulk water from cluster ion data. *International Reviews in Physical Chemistry* **2001**, *20*, 33–58.

(177) Bryantsev, V. S.; Diallo, M. S.; Goddard, W. A. Calculation of solvation free energies of charged solutes using mixed cluster/continuum models. *The Journal of Physical Chemistry B* **2008**, *112*, 9709–19.

(178) Solis, B. H.; Hammes-Schiffer, S. Theoretical Analysis of Mechanistic Pathways for Hydrogen Evolution Catalyzed by Cobaloximes. *Inorganic Chemistry* **2011**.

(179) Evans, M. G.; Polanyi, M. Some applications of the transition state method to the calculation of reaction velocities, especially in solution. *Transactions of the Faraday Society* **1935**, *31*, 875.

(180) Eyring, H. The Activated Complex in Chemical Reactions. *The Journal of Chemical Physics* **1935**, *2*, 853.

(181) Goodrow, A.; Bell, A. T.; Head-Gordon, M. Are Spin-Forbidden Crossings a Bottleneck in Methanol Oxidation? *The Journal of Physical Chemistry C* **2009**, *113*, 19361–19364.

(182) Solis, B. H.; Hammes-Schiffer, S. Substituent effects on cobalt diglyoxime catalysts for hydrogen evolution. *Journal of the American Chemical Society* **2011**, *133*, 19036–9.

(183) Palczewski, K. G protein-coupled receptor rhodopsin. *Annual Review of Biochemistry* **2006**, *75*, 743–67.

(184) Delgado, J. L.; Bouit, P.-A.; Filippone, S.; Herranz, M. A.; Martín, N. Organic Photovoltaics: A Chemical Approach. *Chemical Communications* **2010**, *46*, 4853–65.

(185) Zimmerman, P. M.; Bell, F.; Casanova, D.; Head-Gordon, M. Mechanism for singlet fission in pentacene and tetracene: from single exciton to two triplets. *Journal of the American Chemical Society* **2011**, *133*, 19944–52.

(186) Zimmerman, P. M.; Musgrave, C. B.; Head-Gordon, M. A Correlated Electron View of Singlet Fission. *Accounts of chemical research* **2013**, 1339–1347.

(187) Burke, K.; Werschnik, J.; Gross, E. K. U. Time-dependent density functional theory: past, present, and future. *The Journal of Chemical Physics* **2005**, *123*, 62206.

(188) Runge, E.; Gross, E. K. U. Density-Functional Theory for Time-Dependent Systems. *Physical Review Letters* **1984**, *52*, 997–1000.

(189) Maitra, N. T.; Zhang, F.; Cave, R. J.; Burke, K. Double excitations within time-dependent density functional theory linear response. *The Journal of Chemical Physics* **2004**, *120*, 5932–7.

(190) Elliott, P.; Goldson, S.; Canahui, C.; Maitra, N. T. Perspectives on double-excitations in TDDFT. *Chemical Physics* **2011**, *391*, 110–119.

(191) Cave, R. J.; Zhang, F.; Maitra, N. T.; Burke, K. A dressed TDDFT treatment of the 2^1A_g states of butadiene and hexatriene. *Chemical Physics Letters* **2004**, *389*, 39–42.

(192) Mazur, G.; Włodarczyk, R. Application of the dressed time-dependent density functional theory for the excited states of linear polyenes. *Journal of Computational Chemistry* **2009**, *30*, 811–7.

(193) Cullen, J.; Krykunov, M.; Ziegler, T. The formulation of a self-consistent constricted variational density functional theory for the description of excited states. *Chemical Physics* **2011**, *391*, 11–18.

(194) Krylov, A. I. Equation-of-Motion Coupled-Cluster Methods for Open-Shell and Electronically Excited Species: The Hitchhiker's Guide to Fock Space. *Annual Review of Physical Chemistry* **2008**, *59*, 433–462.

(195) Head-Gordon, M.; Rico, R. R. J.; Oumi, M.; Lee, T. T. J. A doubles correction to electronic excited states from configuration interaction in the space of single substitutions. *Chemical Physics Letters* **1994**, *219*, 21–29.

(196) Christiansen, O.; Koch, H.; Jørgensen, P. The second-order approximate coupled cluster singles and doubles model CC2. *Chemical Physics Letters* **1995**, *243*, 409–418.

(197) Hirata, S.; Nooijen, M.; Bartlett, R. J. High-order determinantal equation-of-motion coupled-cluster calculations for electronic excited states. *Chemical Physics Letters* **2000**, *326*, 255–262.

(198) Sears, J. S.; Sherrill, C. D.; Krylov, A. I. A spin-complete version of the spin-flip approach to bond breaking: What is the impact of obtaining spin eigenfunctions? *The Journal of Chemical Physics* **2003**, *118*, 9084.

(199) Casanova, D.; Head-Gordon, M. The spin-flip extended single excitation configuration interaction method. *The Journal of Chemical Physics* **2008**, *129*, 064104.

(200) Malmqvist, P. Å. Calculation of transition density matrices by nonunitary orbital transformations. *International Journal of Quantum Chemistry* **1986**, *30*, 479–494.

(201) Thom, A. J. W.; Head-Gordon, M. Hartree–Fock solutions as a quasidiabatic basis for nonorthogonal configuration interaction. *The Journal of Chemical Physics* **2009**, *131*, 124113.

(202) Löwdin, P.; Mayer, I. Some Studies of the General Hartree–Fock Method. *Advances in Quantum Chemistry* **1992**, *24*, 79–114.

(203) Jiménez-Hoyos, C. A.; Henderson, T. M.; Scuseria, G. E. Generalized Hartree–Fock Description of Molecular Dissociation. *Journal of Chemical Theory and Computation* **2011**, *7*, 2667–2674.

(204) Overhauser, A. Spin Density Waves in an Electron Gas. *Physical Review* **1962**, *128*, 1437–1452.

(205) Čížek, J.; Paldus, J. Stability Conditions for the Solutions of the Hartree–Fock Equations for Atomic and Molecular Systems. Application to the Pi-Electron Model of Cyclic Polyenes. *Journal of Chemical Physics* **1967**, *407*, 3976–3985.

(206) Paldus, J.; Čížek, J Stability Conditions for the Solutions of the Hartree–Fock Equations for Atomic and Molecular Systems. II Simple Open-Shell Case. *The Journal of Chemical Physics* **1970**, *52*, 2919–2936.

(207) Fukutome, H. Unrestricted Hartree–Fock theory and its applications to molecules and chemical reactions. *International Journal of Quantum Chemistry* **1981**, *20*, 955–1065.

(208) Calais, J. Gap equations and instabilities for extended systems. *Advances in Quantum Chemistry* **1985**, *17*, 225–250.

(209) Jiménez-Hoyos, C. A.; Henderson, T. M.; Tsuchimochi, T.; Scuseria, G. E. Projected Hartree–Fock theory. *The Journal of Chemical Physics* **2012**, *136*, 164109.

(210) Scuseria, G. E.; Jiménez-Hoyos, C. A.; Henderson, T. M.; Samanta, K.; Ellis, J. K. Projected quasiparticle theory for molecular electronic structure. *The Journal of Chemical Physics* **2011**, *135*, 124108.

(211) Ellis, J.; Martin, R.; Scuseria, G. On pair functions for strong correlations. *Journal of Chemical Theory and Computation* **2013**, *9*, 2857–2869.

(212) Samanta, K.; Jiménez-Hoyos, C. A.; Scuseria, G. E. Exploring Copper Oxide Cores Using the Projected Hartree–Fock Method. *Journal of Chemical Theory and Computation* **2012**, *8*, 4944–4949.

(213) Mayer, I. The Spin-Projected Extended Hartree–Fock Method. *Advances in Quantum Chemistry* **1980**, *12*, 189–262.

(214) Rodríguez-Guzmán, R.; Schmid, K. W.; Jiménez-Hoyos, C. A.; Scuseria, G. E. Symmetry-projected variational approach for ground and excited states of the two-dimensional Hubbard model. *Physical Review B* **2012**, *85*, 245130.

(215) Amos, A. T.; Hall, G. G. Single Determinant Wave Functions. *Proceedings of the Royal Society A* **1961**, *263*, 483–493.

(216) King, H. F.; Stanton, R. E.; Kim, H.; Wyatt, R. E.; Parr, R. G. Corresponding Orbitals and the Nonorthogonality Problem in Molecular Quantum Mechanics. *The Journal of Chemical Physics* **1967**, *47*, 1936–1940.

(217) Löwdin, P.-O. Band Theory, Valence Bond, and Tight-Binding Calculations. *Journal of Applied Physics* **1962**, *33*, 251.

(218) Gilbert, A. T. B.; Besley, N. a.; Gill, P. M. W. Self-consistent field calculations of excited states using the maximum overlap method (MOM). *The Journal of Physical Chemistry A* **2008**, *112*, 13164–71.

(219) Pulay, P Convergence Acceleration of Iterative Sequences. The Case of SCF Iteration. *Chemical Physics Letters* **1980**, *73*.

(220) Pulay, P. Improved SCF convergence acceleration. *Journal of Computational Chemistry* **1982**, *3*, 556–560.

(221) Besley, N. A.; Gilbert, A. T. B.; Gill, P. M. W. Self-consistent-field calculations of core excited states. *The Journal of Chemical Physics* **2009**, *130*, 124308.

(222) Peng, B.; Van Kuiken, B. E.; Ding, F.; Li, X. A Guided Self-Consistent-Field Method for Excited-State Wave Function Optimization: Applications to Ligand-Field Transitions in Transition-Metal Complexes. *Journal of Chemical Theory and Computation* **2013**, 3933–3938.

(223) Yost, S. R.; Kowalczyk, T.; Van Voorhis, T. A multireference perturbation method using non-orthogonal Hartree–Fock determinants for ground and excited states. *The Journal of Chemical Physics* **2013**, *139*, 174104.

(224) Sanderson, C. Armadillo: An open source C++ linear algebra library for fast prototyping and computationally intensive experiments. *Technical Report* **2010**, *NICTA*, 1–16.

(225) Kurashige, Y.; Nakano, H.; Nakao, Y.; Hirao, K. The $\pi \rightarrow \pi^*$ excited states of long linear polyenes studied by the CASCI-MRMP method. *Chemical Physics Letters* **2004**, *400*, 425–429.

(226) Hsu, C.-P.; Hirata, S.; Head-Gordon, M. Excitation Energies from Time-Dependent Density Functional Theory for Linear Polyene Oligomers: Butadiene to Decapentaene. *The Journal of Physical Chemistry A* **2001**, *105*, 451–458.

(227) Starcke, J. H.; Wormit, M.; Schirmer, J.; Dreuw, A. How much double excitation character do the lowest excited states of linear polyenes have? *Chemical Physics* **2006**, *329*, 39–49.

(228) Watts, J. D.; Gwaltney, S. R.; Bartlett, R. J. Coupled-cluster calculations of the excitation energies of ethylene, butadiene, and cyclopentadiene. *The Journal of Chemical Physics* **1996**, *105*, 6979.

(229) Watson, M. A.; Chan, G. K.-L. Excited States of Butadiene to Chemical Accuracy: Reconciling Theory and Experiment. *Journal of Chemical Theory and Computation* **2012**, *8*, 4013–4018.

(230) Lehtonen, O.; Sundholm, D.; Send, R.; Johansson, M. P. Coupled-cluster and density functional theory studies of the electronic excitation spectra of trans-1,3-butadiene and trans-2-propeniminium. *The Journal of Chemical Physics* **2009**, *131*, 024301.

(231) Kitao, O.; Nakatsuji, H. Cluster expansion of the wavefunction: Valence and Rydberg excitations of trans- and cis-butadiene. *Chemical Physics Letters* **1988**, *143*, 528–534.

(232) Saha, B.; Ehara, M.; Nakatsuji, H. Singly and doubly excited states of butadiene, acrolein, and glyoxal: Geometries and electronic spectra. *The Journal of Chemical Physics* **2006**, *125*, 014316.

(233) Serrano-Andrés, L.; Lindh, R.; Roos, B. O.; Merchán, M. Theoretical study of the electronic spectrum of all-trans-1,3,5,7-octatetraene. *The Journal of Physical Chemistry* **1993**, *97*, 9360–9368.

(234) Nakayama, K.; Nakano, H.; Hirao, K. Theoretical study of the $\pi \rightarrow \pi^*$ excited states of linear polyenes: The energy gap between $1^1B_u^+$ and $2^1A_g^-$ states and their character. *International Journal of Quantum Chemistry* **1998**, *66*, 157–175.

(235) Ostojić, B.; Domcke, W. Ab initio investigation of the potential energy surfaces involved in the photophysics of s-trans-1,3-butadiene. *Chemical Physics* **2001**, *269*, 1–10.

(236) Boggio-Pasqua, M.; Bearpark, M. J.; Klene, M.; Robb, M. A. A computational strategy for geometry optimization of ionic and covalent excited states, applied to butadiene and hexatriene. *The Journal of Chemical Physics* **2004**, *120*, 7849–60.

(237) Doering, J. P.; McDiarmid, R. Electron impact study of the energy levels of trans-1,3-butadiene: II. Detailed analysis of valence and Rydberg transitions. *The Journal of Chemical Physics* **1980**, *73*, 3617.

(238) Serrano-Andrés, L.; Merchán, M.; Nebot-Gil, I.; Lindh, R.; Roos, B. O. Towards an accurate molecular orbital theory for excited states: Ethene, butadiene, and hexatriene. *The Journal of Chemical Physics* **1993**, *98*, 3151.

(239) Polívka, T.; Sundström, V. Dark excited states of carotenoids: Consensus and controversy. *Chemical Physics Letters* **2009**, *477*, 1–11.

(240) Ghosh, D.; Hachmann, J.; Yanai, T.; Chan, G. K.-L. Orbital optimization in the density matrix renormalization group, with applications to polyenes and beta-carotene. *The Journal of Chemical Physics* **2008**, *128*, 144117.

(241) Grimme, S.; Waletzke, M. A combination of Kohn–Sham density functional theory and multi-reference configuration interaction methods. *The Journal of Chemical Physics* **1999**, *111*.

(242) Kleinschmidt, M.; Marian, C. M.; Waletzke, M.; Grimme, S. Parallel multireference configuration interaction calculations on mini-beta-carotenes and beta-carotene. *The Journal of Chemical Physics* **2009**, *130*, 044708.

(243) Tschirner, N.; Schenderlein, M.; Brose, K.; Schlodder, E.; Mroginski, M. A.; Thomsen, C.; Hildebrandt, P. Resonance Raman spectra of beta-carotene in solution and in photosystems revisited: an experimental and theoretical study. *Physical Chemistry Chemical Physics* **2009**, *11*, 11471–8.

(244) Fukutome, H. Theory of Resonating Quantum Fluctuations in a Fermion System: Resonating Hartree–Fock Approximation. *Progress of Theoretical Physics* **1988**, *80*, 417–432.

(245) Schreiber, M.; Silva-Junior, M. R.; Sauer, S. P. A.; Thiel, W. Benchmarks for electronically excited states: CASPT2, CC2, CCSD, and CC3. *The Journal of Chemical Physics* **2008**, *128*, 134110.

(246) Sundstrom, E. J.; Head-Gordon, M. Non-orthogonal configuration interaction for the calculation of multielectron excited states. *The Journal of Chemical Physics* **2014**, *140*, 114103.

(247) Dreuw, A.; Head-Gordon, M. Single-reference ab initio methods for the calculation of excited states of large molecules. *Chemical Reviews* **2005**, *105*, 4009–37.

(248) Davidson, E. R. The iterative calculation of a few of the lowest eigenvalues and corresponding eigenvectors of large real-symmetric matrices. *Journal of Computational Physics* **1975**, *17*, 87–94.

(249) Martin, R. L. Natural transition orbitals. *The Journal of Chemical Physics* **2003**, *118*, 4775.

(250) Schäfer, A.; Horn, H.; Ahlrichs, R. Fully optimized contracted Gaussian basis sets for atoms Li to Kr. *The Journal of Chemical Physics* **1992**, *97*, 2571.

(251) Liu, X.; Subotnik, J. E. The Variationally Orbital-Adapted Configuration Interaction Singles (VOA-CIS) Approach to Electronically Excited States. *Journal of Chemical Theory and Computation* **2014**, *10*, 1004–1020.

(252) Sykja, B; Calais, J.-L. Pairing and general spin orbitals. *Journal of Physics C: Solid State Physics* **1982**, *15*, 3079–3092.